Drag Reduction Fundamentals

Drag reduction by dilute solutions of linear, random-coiling macromolecules in turbulent pipe flow is reviewed. The experimental evidence is emphasized in three sections concerned with the graphical display of established features of the phenomenon, data correlation and analysis, and the physical mechanism of drag reduction.

P. S. VIRK

Department of Chemical Engineering
Indian Institute of Technology
Madras 600036, India

SCOPE

Our objective is to acquaint the reader with the phenomenon of drag reduction, in which the skin friction caused by turbulent flow of an ordinary liquid is reduced by additives. This phenomenon, discovered about 1947, has received attention because it suggests practical benefits, such as increased pipeline capacities and faster ships, and is also theoretically stimulating, in the areas of wall turbulence and molecular rheology. This review, restricted to drag reduction by polymer solutions in pipe flow, has three sections: (1) the experimental evidence, (2) correlation and analysis, and (3) mechanism. Section 1 presents experimentally established results showing the flow regimes exhibited by polymer solutions, the relationships among flow and macromolecular parameters, and the changes in mean and turbulent flow structures which accompany drag reduction. The conclusions of Section 1 are documented in Section 2. The latter concerns the empirical correlation of experimental results, with analysis (and tabulations) of the data used for this purpose. Section 2 also provides for discussion of evidence not fully enough established to be included in Section 1. Finally, in Section 3 an attempt is made to physically interpret the experimental results, to infer the nature of the polymer-turbulence interaction responsible for drag reduction and its effect on the energy balances of turbulent pipe flow.

CONCLUSIONS AND SIGNIFICANCE

1. *Gross Flow.* Drag reduction by dilute polymer solutions in turbulent pipe flow appears bounded between two universal asymptotes, namely, the Prandtl-Karman law [Equation (2)] for Newtonian turbulent flow and a maximum drag reduction asymptote [Equation (4)]. Between these limits is a polymeric regime in which the observed friction factor relations are approximately linear on Prandtl-Karman coordinates and can be characterized by two parameters—the wall shear stress at the onset of drag reduction and the slope increment by which the polymer solution slope exceeds Newtonian. For a given polymer species-solvent pair: The onset wall shear stress is essentially independent of pipe diameter, polymer concentration, and solvent viscosity, and varies inversely as the two to three power of polymer radius of gyration [Equations (19) and (5)]. The slope increment is essentially independent of pipe diameter, varies as the square root of polymer concentration, and as the three-halves power of the number of chain links in the polymer backbone [Equation (6)], and seems unaffected by decreases in polymer excluded volume.

2. *Mean Velocity Profiles.* On law of the wall coordinates, these possess, in general, three zones: from the wall outward, there is the usual viscous sublayer, from the axis inward is the Newtonian plug region wherein the velocity profile is shifted upward from, but parallel to, the Newtonian law of the wall, and between these is a region, which we call the elastic sublayer, that is characteristic of drag reduction and across which U^+ climbs to above Newtonian by an amount S^+, the effective slip. With increasing drag reduction elastic sublayer extent increases until, at maximum drag reduction, it pervades the entire cross section. Beyond the viscous sublayer [Equation (7)], therefore, mean velocity profiles are bounded by asymptotes, [Equations (8) and (9)], analogous to (actually, transforms of) the friction factor asymptotes [Equations (2) and (4)]; the maximum drag reduction profile has a mixing length constant of 0.085, about a fifth of the Newtonian value, 0.40. Between these limits, the profiles show both the elastic sublayer and Newtonian plug regions, the respective extent of which can be simply related to the polymeric regime friction factor relation.

3. *Turbulence Structure.* Data, available only in the polymeric regime, suggest three radial zones analogous to those observed in the mean velocity profiles. In the viscous sublayer, the Newtonian streaky structure seems to remain at least partially intact during drag reduction, with the axial intensity gradient at the wall and the aspect ratio of transverse macroscales both essentially the same as Newtonian. In the elastic sublayer, the turbulence structure is significantly different from Newtonian: relatively, the (nondimensional) axial intensity is higher while the radial intensity, turbulent shear stress, and u-v correlation coefficient are all lower. The maximum turbulent kinetic energy appears to exceed Newtonian by roughly the same amount S^+ that the maximum mean velocity exceeds Newtonian. Finally, the Newtonian plug region has turbulence structure the same as Newtonian, based on axial and radial intensity measurements.

4. *Physical Interpretations.* The polymer-turbulence interaction responsible for drag reduction appears to commence in the vicinity $y^+ \simeq 15$ of the plane of peak turbulent energy production, suggesting that the polymer molecules interfere with the turbulent bursting processes. At the onset of drag reduction, the duration of a turbulent burst is of the order of the relaxation time of a macro-

molecule, and after onset, the extent of drag reduction correlates with the turbulent strain energy of a dilute polymer solution. These observations suggest that macromolecular extension is involved in the mechanism of drag reduction. The random-coiled radius of gyration of the macromolecule is significantly smaller than, by about 10^{-3} times, the smallest turbulent burst length scale. The axial and radial turbulent flow fields are decoupled in the region of interaction, as witnessed by a striking reduction in the u-v correlation coefficient, relative to Newtonian. The polymer-induced flow field decoupling seems to retard about equally the radial transport of axial momentum and of turbulent kinetic energy. The observed drag reduction is possibly a consequence of the readjustments, notably an increase in maximum kinetic energy, that the inner flow makes to maintain the overall cross-sectional turbulent energy balance.

Experiments, the earliest by Toms (1948) and Mysels (1949), have established that the skin friction caused by turbulent flow of an ordinary liquid past a solid surface can be reduced significantly by the addition of small amounts of certain materials to the liquid. This phenomenon, commonly termed *drag reduction* or *Toms phenomenon,* suggests possible practical benefits, such as increased pipeline capacities and faster ships, which have motivated much research during the past decade. This work is an attempt to summarize developments in the basic, and certainly the most studied, case of drag reduction by dilute solutions of linear random-coiling polymers in turbulent flow through smooth pipes. A future extension of this work is contemplated to consider selected flow and additive related topics. Flow-related topics include the effect of wall roughness, scalar transport during drag reduction, external boundary layer flows, and laminar-to-turbulent transition while additive-related topics include the influence of polymer chain conformation and excluded volume, the effects of heterogeneous molecular weight distributions, the kinetics of polymer degradation, and aspects of drag reduction by soaps, fibers, and polyelectrolytes.

Earlier reviews of the subject are each separately noteworthy. Zakin and co-workers (Patterson, Zakin, and Rodriguez, 1969) have contributed many of the available results on drag reduction in organic solvents, and their work emphasizes this area. Hoyt (1972), a pioneer investigator in this field, provides a most comprehensive compilation and discussion of the literature. Lumley (1969, 1973) considers possible mechanisms of drag reduction with his customary penetrating physical insight. Landahl (1973) emphasizes the fluid mechanics viewpoint, with a particularly cogent discussion of the role of rheology.

This review is intended to convey some of the experimental facts and theoretical understanding of drag reduction to the reader not necessarily familiar with the subject. There are four sections:

1. The experimental evidence. The main physical features of the drag reduction phenomenon and their dependencies on flow and polymer related variables are depicted in graphical form and described.

2. Correlation and analysis. The available experimental information is summarized by empirical correlations based on the elastic sublayer model of drag reduction (Virk, 1971). Tables containing the primary results of our analysis of the literature are presented. There is also some discussion of experimental evidence, mainly those results either peripheral to, or not fully enough established to be included in, Section 1.

3. Mechanism. The mechanism of drag reduction is considered with mention of models proposed in the literature and an attempt to physically interpret the experimental observations in terms of the basic polymer-turbulence interaction responsible for drag reduction and its effect on the energy balances of turbulent pipe flow.

SUMMARY

It was hoped that Section 1 would describe the essential physics of drag reduction, Section 2 provide the basic documentation, and Section 3 physically interpret the experimental results. However, the reader should be forewarned about what has finally transpired. Section 1 is a deluge of seeming similar semi-log graphs, and we fear it will take persistent perusal of data points, captions, and text to discern any essential physics within. In Section 2, the basic documentation lies in tables and data analysis, both decidedly dull reading; yet we entreat the reader to plough through because the reservations which must be expressed about drag reduction data do tend to exceed the information therein. In Section 3, the physical interpretation is based on a relatively few facts and regrettably too much conjecture and should, therefore, be read with the appropriate skepticism; and, alas, there is no happy ending, the mechanism of drag reduction remaining obscure.

1. THE EXPERIMENTAL EVIDENCE

The experimental evidence is classified into three echelons of increasing detail, namely, (1) gross flow studies, (2) mean velocity profiles, and (3) turbulence structure measurements.

1.1 Gross Flow

Gross flow studies involve pressure drop versus flow rate measurements, an example of which will introduce the phenomenon of drag reduction. Figure 1 shows results obtained in the same pipe, 8.46 mm I.D., for pure solvent (hollow circles) and for a polymer solution (solid circles) containing 300 weight parts per million of a polyethyleneoxide of molecular weight 0.57×10^6 dissolved in distilled water. The data are plotted three ways. Figure 1a, log-log, shows directly the measured flow rate versus the corresponding wall shear stress, the latter simply related to the measured pressure gradient. Figure 1b, also log-log, shows the data on nondimensional coordinates of Fanning friction factor versus Reynolds number, while Figure 1c, semi-log, employs the Prandtl-von Karman form of plotting $f^{-1/2}$ versus log $Ref^{1/2}$. Following both sets of data from low to high flow rates reveals that in laminar flow, $Re < 2000$, the polymer solution and solvent exhibit identical behavior. In turbulent flow, $Re > 3000$, the polymer solution data are identically the same as solvent for $3000 < Re < 12000$; at $Re \simeq 12000$ ($T_w \simeq 7.0$ N/m^2, $Ref^{1/2} \simeq 1100$), we witness a rather distinct onset of drag reduction and, for $Re >$ 12000, the polymer solution data diverge from solvent in the direction of lower friction. The extent of drag reduction can be measured either by the ratio of polymer solution to solvent wall shear stresses at the same flow rate or by the ratio of flow rates at the same wall shear stress. It can be seen that, after onset, the drag reduction increases with increasing flow rate and at the highest flow rate of polymer

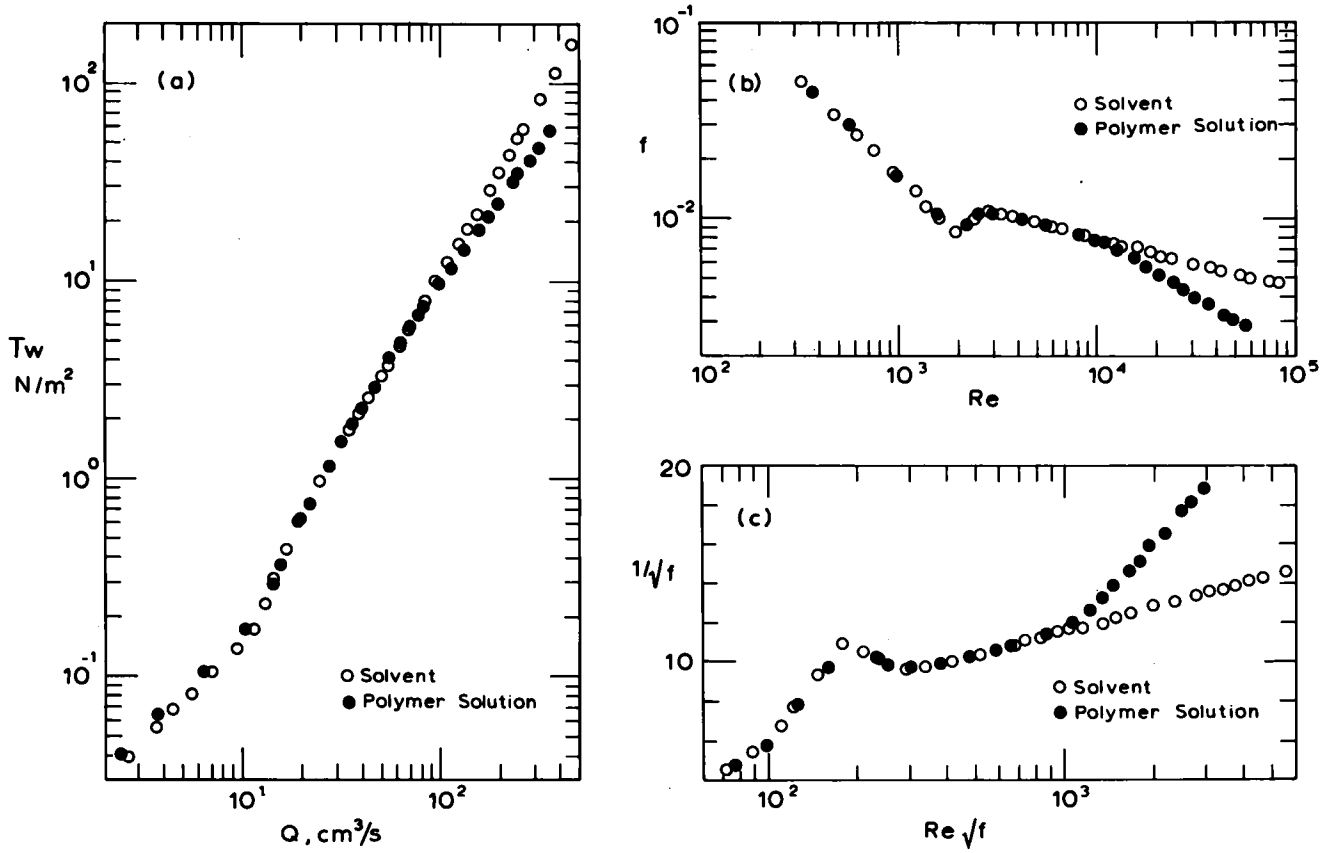

Fig. 1. Drag reduction depicted on various gross flow coordinates. Pipe I.D. 8.46 mm, temperature 25 C, solvent distilled water, polymer solution PEO, $M = 0.57 \times 10^6$, $c = 296$ wppm.

solution the shear stress ratio is 0.56 while the flow rate ratio is 1.38. Either way, it is evident that the specific energy required to sustain turbulent flow of the polymer solution can be significantly less than that required for the solvent alone. This introduction is completed with brief comment on polymer solution characterization, Prandtl-Karman (P-K) coordinates, and some drag reduction scales.

The description of polymer solutions follows standard practice (see Flory, 1953; Tanford, 1961; and Yamakawa, 1971). The polyethyleneoxides are a homologous series of macromolecules in which the repeating $(CH_2/CH_2\backslash O)$ mer units are linked head-to-tail in linear fashion. Figure 1 was obtained using a commercial polymer sample which possessed a rather broad molecular weight distribution, with weight to number average ratio $M_w/M_n \simeq 4$ about twice the most probable value; its $M_w = 0.57 \times 10^6$ corresponds to a degree of polymerization of 1.3×10^4 so that the backbone of the average macromolecule consisted of a chain of 3.9×10^4 consecutive covalent C—C and C—O bonds. The number of backbone chain links is a parameter of importance in polymer chain statistics and the efficacy of a macromolecule in drag reduction too appears dependent on it. In distilled water solution PEO macromolecules exist as random coils. For our solution, $\eta_{rel} \simeq 1.10$ corresponding to a nondimensional concentration $c[\eta] \simeq 0.10$ which latter physically approximates the volume fraction of solution occupied by the macromolecular random coils. Polymer solutions of $\eta_{rel} < 2.0$ might reasonably be considered dilute, and most of the examples which follow will meet this criterion. Based on light scattering experiments, the radius of gyration of our polymer in distilled water was 81 nm; this is a measure of the radius of the biggest random coils in a static solution and shows also that these are significantly expanded, to 1.4 times their radius in a theta solvent. The contour length of the polymer is 6000 nm; this is measured end-to-end along the backbone chain, the ratio (L_C/R_G) typically being about $N^{1/2}$. The relaxation time of the polymer molecules in solution is not experimentally accessible but can be estimated from the theory of Zimm (1956) to be about 0.3×10^{-3} s.

Prandtl-Karman coordinates appear to be the most natural for depicting drag reduction in pipes and will be employed almost exclusively hereafter. These involve the use of a friction velocity $u_T = (T_w/\rho)^{1/2}$, formed from the wall shear stress, as a scale characteristic of the turbulence; near the pipe wall, the corresponding turbulent length and time scales are respectively ν/u_T and ν/u_T^2. Physically therefore the ordinate $f^{-1/2} = U_{av}/\sqrt{2}u_T$ is a ratio of bulk to turbulent velocities while the abscissa $Ref^{1/2} = \sqrt{2}du_T/\nu$ is a ratio of pipe to turbulence length scales (the awkward numerical factors are due to entrenched definitions of f and Re).

Some typical drag reduction scales illustrated by the example are noted. The very dilute nature of the polymer solution, weight fraction polymer 0.0003, volume fraction random coils 0.10, suggests that individual macromolecules are involved rather than entangled clusters. At the onset of drag reduction, the ratio of polymer to turbulence length scales is $R_G u_T/\nu = 0.008$, while the ratio of time scales is $\tau_t u_T^2/\nu = 2.0$; that is, the macromolecular random coil has static dimensions rather smaller than those of the energy-containing turbulent eddies near the pipe wall, but its relaxation time about equals wall eddy lifetime.

1.1.1 Gross Flow Regimes. The general pattern of gross flow behavior is somewhat more complex than indicated in the preceding example and will now be considered in detail. In laminar pipe flow, the dilute polymer solutions of interest to us here do nothing unusual. The majority obey Poiseuille's law:

$$f^{-1/2} = Ref^{1/2}/16 \qquad (1)$$

Solution viscosities are generally so close to solvent that shear thinning, which almost all polymer solutions exhibit to some extent at high enough shear rates, has little discernible effect on the gross flow. In fully turbulent pipe flow, dilute polymer solutions exhibit three distinct regimes which are, in order of increasing flow rate:

1. A regime without drag reduction in which the friction factor relation is the same as for solvent, that is, the usual Prandtl-Karman (or Blasius) law for Newtonian turbulent flow

$$f^{-1/2} = 4.0 \log_{10} Re f^{1/2} - 0.4 \qquad (2)$$

2. A regime with drag reduction in which the friction factor relation depends upon the nature of the polymer solution. Anticipating later results, an approximate relation for this regime is

$$f^{-1/2} = (4.0 + \delta) \log_{10} Re f^{1/2} - 0.4 - \delta \log_{10} \sqrt{2} dW^* \qquad (3)$$

where δ, W^* are polymer solution parameters.

3. An asymptotic regime of maximum possible drag reduction in which the friction factor relation is insensitive to the polymer solution employed, being, universally,

$$f^{-1/2} = 19.0 \log_{10} Re f^{1/2} - 32.4 \qquad (4)$$

The foregoing will respectively be termed the Newtonian (N), polymeric (P), and maximum drag reduction (M) regimes, the laminar (L) regime having been noted first. Laminar to turbulent transition is not well detected by gross flow studies and therefore only a brief description will be given in Section 1.1.6 after the turbulent flow regimes have been considered.

1.1.2 Polymeric Regime. Aspects of the polymeric regime are illustrated in Figures 2a to 2d using P-K coordinates with abscissae $Re_s f^{1/2}$, all based on solvent viscosity.

The effect of pipe diameter is shown in Figure 2a which contains data for solvent (hollow points) and the same polymer solution in each of three pipes, of inside diameters respectively 2.92, 8.46, and 32.1 mm. Two features merit attention. First, the onset of drag reduction in the three cases occurs at $Re_s f^{1/2*} \simeq 400$, 1100, and 4000, the ratio of which, 0.36:1.0:3.6, closely approximates the ratio of pipe diameters, 0.35:1.0:3.8. Thus, regardless of pipe size, the given polymer solution reduces drag only after a certain wall shear stress $T_w^* \simeq 7.0$ N/m^2 has been exceeded. Second, it will be noticed that, after onset, the polymer solution data describe approximately straight lines which have much the same slope in all pipes. The difference between polymer solution and solvent slopes, called the *slope increment*, is in this case $\delta = 11 \pm 2$.

The effect of polymer concentration is shown by Figure 2b which displays data taken in the same pipe for solutions of the same polymer ranging in concentration from 50 to 1000 wppm. For clarity, solvent (distilled water) data have been omitted, being replaced by solid lines representing the Prandtl-Karman law (2) to which they closely adhered; also, ordinates have been shifted upward in an obvious way for each successive set of data, and straight lines have been drawn through the polymer solution points after onset. In each case it can be seen that the onset of drag reduction occurs at a rather well defined $Re_s f^{1/2*}$. Further, in all four solutions, spanning a 20-fold concentration range, onset occurs at much the same $Re_s f^{1/2*} = 1150 \pm 100$. Thus, the onset wall shear stress is essentially independent of polymer concentration. After onset the polymer solution data are quite well approximated by the indicated straight lines, the slopes increasing with increasing concentration such that the slope increment is $\delta = (4.3, 6.9, 11.7, 18.5)$ for $c = (44, 100, 300, 940)$ wppm, respectively. Scrutiny of these results will reveal that δ varies approximately as the square root of polymer concentration with $\delta/c^{1/2} = 0.65 \pm 0.05$.

The effect of polymer molecular weight is illustrated in Figure 2c, using data taken in the same pipe with distilled water solutions of various homologous PEO polymers ranging in molecular weight from 0.1×10^6 to 8×10^6. It is apparent that, as molecular weight is increased, the

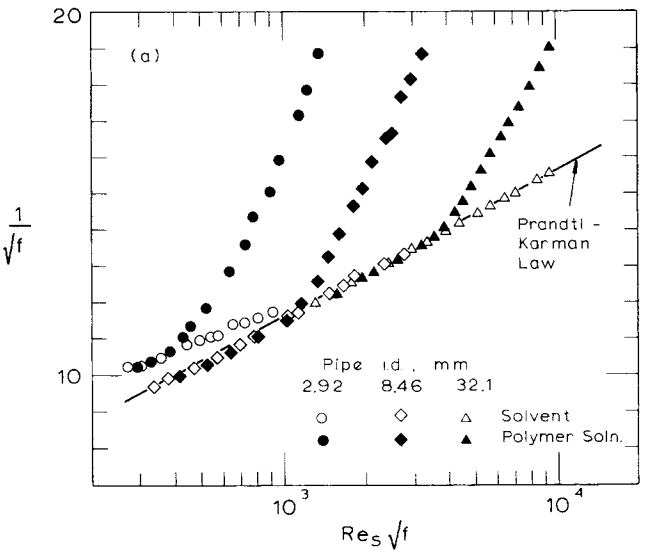

Fig. 2a. Aspects of the polymeric regime: Effect of pipe diameter. Pipe I.D. 2.92, 8.46, and 32.1 mm, temperature 25 C, solvent distilled water, polymer solution PEO, $M = (0.66 \pm 0.10) \times 10^6$, $c = 250 \pm 50$ wppm.

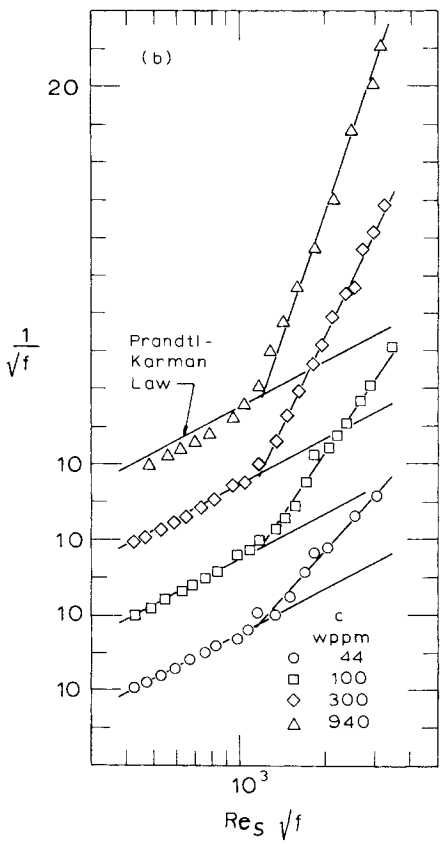

Fig. 2b. Aspects of the polymeric regime: Effect of concentration. Pipe I.D. 8.46 mm, temperature 25 C, solvent distilled water, polymer PEO, $M = 0.57 \times 10^6$, $c = 44$, 100, 300, 940 wppm.

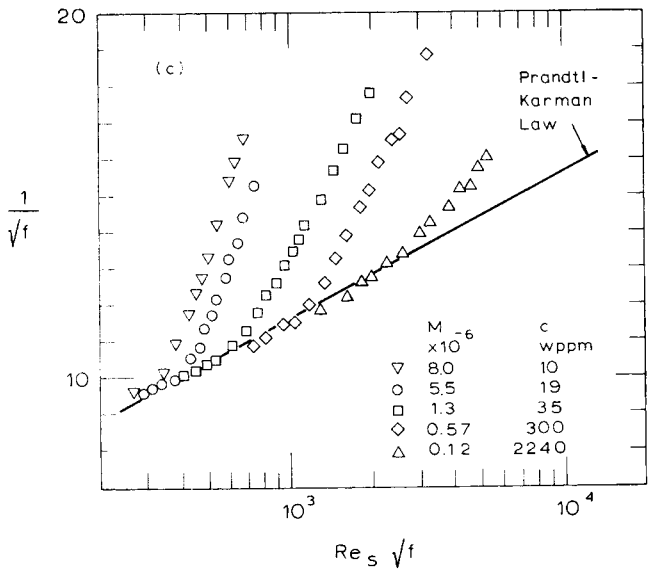

Fig. 2c. Aspects of the polymeric regime: Effect of molecular weight. Pipe I.D. 8.46 and 9.45 mm, temperature 25 C, solvent distilled water, polymer PEO, ($M \times 10^{-6}$, c wppm) as follows: (8.0, 10), (5.5, 10), (1.3, 35), (0.57, 300), (0.12, 2240).

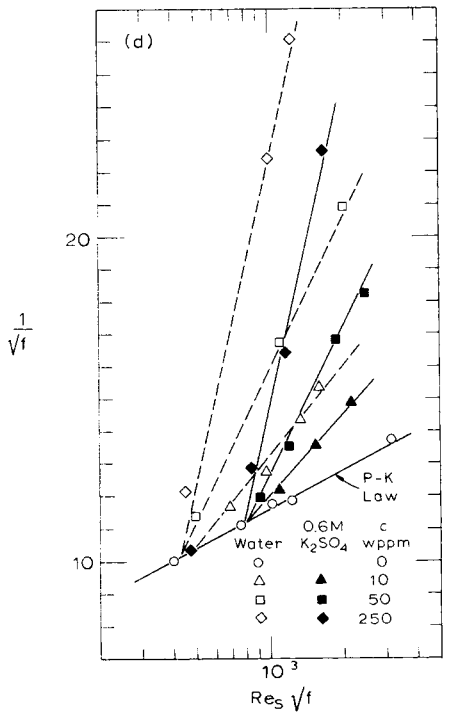

Fig. 2d. Aspects of the polymeric regime: Effect of polymer coil size (data from Pruitt, Rosen, and Crawford 1966). Pipe I.D. 4.57 mm, temperature 22 C, solvents water and 0.6m K_2SO_4, polymer PEO, $M = 0.8 \times 10^6$, $c =$ 10, 50, 250 wppm.

onset of drag reduction occurs at lower $Re_s f^{1/2*}$, and strikingly lower concentrations are required to yield a given slope increment. Molecular weight thus strongly influences the effectiveness of a polymer in reducing drag and, speaking qualitatively, T_w^* varies inversely and δ directly as M.

The effect of polymer random coil size in solution is shown in Figure 2d, using data derived from Pruitt, Rosen, and Crawford (1966), who studied drag reduction by the same PEO polymer in water, a good solvent, and in 0.6m K_2SO_4, a poorer solvent. From their reported intrinsic viscosities of the polymer in these two solvents, R_G is estimated to be 96 nm in water and 65 nm in 0.6m K_2SO_4. In Figure 2d, all of the data shown were obtained in the same pipe; the bottom-most solid line represents the Prandtl-Karman law, polymer concentrations are distinguished by symbols, water solution data (hollow) are faired through by broken lines, and 0.6m K_2SO_4 solution data (solid) by light continuous lines. It is evident that the change in solvent from water to 0.6m K_2SO_4 shifts the onset of drag reduction from $Re_s f^{1/2*} \simeq 500$ to $Re_s f^{1/2*} \simeq 800$ but does not appreciably alter the slopes exhibited by the polymer solutions after onset. Thus, a decrease in the dimensions of a macromolecular random-coil in solution increases the onset wall shear stress but does not much affect the slope increment.

The effect of solvent viscosity on drag reduction is still uncertain, fragmentary evidence (Section 2) suggesting that T_w^* is independent of viscosity.

1.1.3 Onset. In summary, the onset of drag reduction occurs at a rather well-defined onset wall shear stress T_w^*. For a given polymer solution, T_w^* is essentially the same in pipes of different diameters. For solutions of a given polymer-solvent combination, T_w^* is approximately independent of polymer concentration. And onset depends on the polymer random-coil size in solution, with T_w^* increasing as R_G decreases. The onset of drag reduction implies incipient interaction betwen the turbulent flow and the polymer molecule in solution and, among experimentally accessible quantities, T_w^* and R_G are respectively the flow and polymeric parameters most relevant to onset. The relationship observed between T_w^* and R_G in the pipe flow of PEO solutions is indicated in Figure 3, log-log coordinates. Amid scatter, T_w^* varies as an inverse 2 to 3 power of R_G. The solid line in the figure has been drawn with slope -3 and represents the data within a factor $2^{\pm 1}$ over a 500-fold

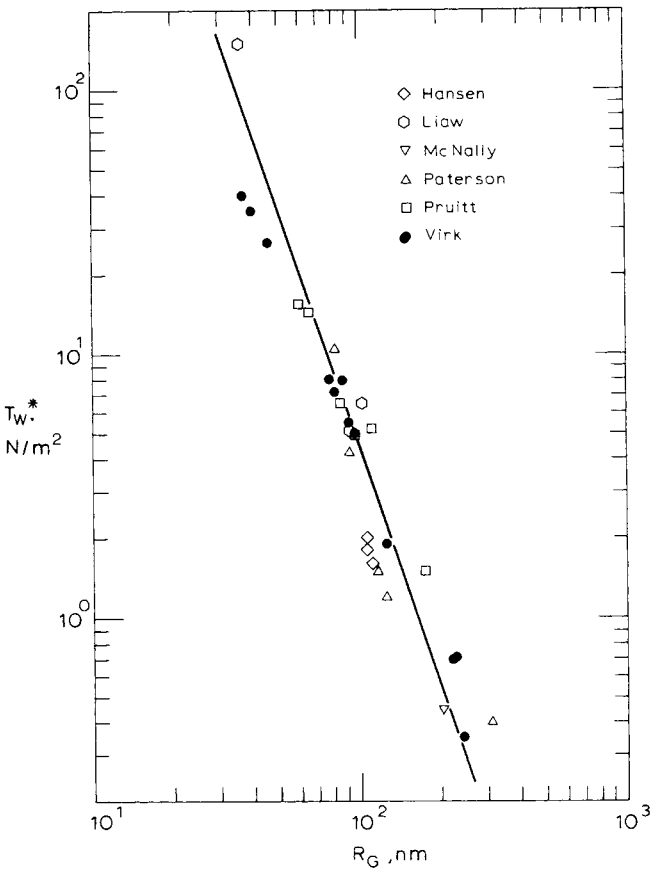

Fig. 3. Onset results for polyethyleneoxide solutions. Solid line corresponds to an onset constant $\Omega_T = 4.4 \times 10^6$. Data from Table 2.

range of T_w^*. This corresponds to an onset correlation of the form

$$R_G{}^3 T_w^* = \Omega_T \qquad (5)$$

with an average onset constant $\Omega_T = 4.4 \times 10^6$ (dimensional with R_G in nm, T_w^* in N/m^2) for PEO. Onset observations obtained with various polymers other than PEO are shown in Figure 4 using the same coordinates as Figure 3. Among the polymers PAM, PDMS, and PIB, for which T_w^* data are available over a range of R_G, the observed power law slopes are respectively -1.6, -2.4, and -2.3. Forcible fitting of the onset correlation (5) to the PAM and PIB data, as indicated by the two solid lines in Figure 4, yields onset constants $\Omega_T = 13 \times 10^6$ in each case. These are rather higher than for PEO, the average line for which is shown dashed in Figure 4, indicating that Ω_T depends upon polymer species (and possibly solvent also). Notice, however, that most of the onset data lie between the lines respectively representing PEO and PAM-PIB, implying that an order of magnitude $\Omega_T = 10 \times 10^6$ prevails for all onset results obtained until now.

1.1.4 Slope Increment. After onset, polymer solutions describe nearly straight lines on Prandtl-Karman coordinates, with their slopes exceeding the solvent slope. For a given polymer solution, the slope increment δ is essentially the same in pipes of different diameters. For solutions of a given polymer-solvent combination, δ increases approximately as the square root of polymer concentration. Also, δ depends on polymer molecular weight but, for solutions of a given polymer, δ is not appreciably affected by decreased polymer random-coil size. The square-root relationship between δ and c is depicted in Figure 5, log-log: the solid lines have all been drawn with slope 1/2 and can be seen to reasonably represent the variation of δ over concentration ranges of from one to three decades. The quantity $\delta/c^{1/2}$, which we call specific slope increment, would therefore appear to characterize the drag reducing ability of a polymer-solvent pair after onset and the wide separation of the data for different polymers on Figure 5 suggests its further dependence on polymeric parameters. From $\delta/c^{1/2}$, one can obtain $\Pi = \delta/(c/M)^{1/2}$ which is properly termed an *intrinsic* (that is, per macromolecule) slope increment and seek its relationship to the number of backbone chain links N which is the essential configurational parameter. This leads to Figure 6 which displays some of the available drag reduction literature on coordinates of Π versus N, log-log. All polymers with methylene \C/C\, oxyethylene \O/C\C/, and siloxane \Si/O\ backbone, which are structurally similar, lie on much the same line

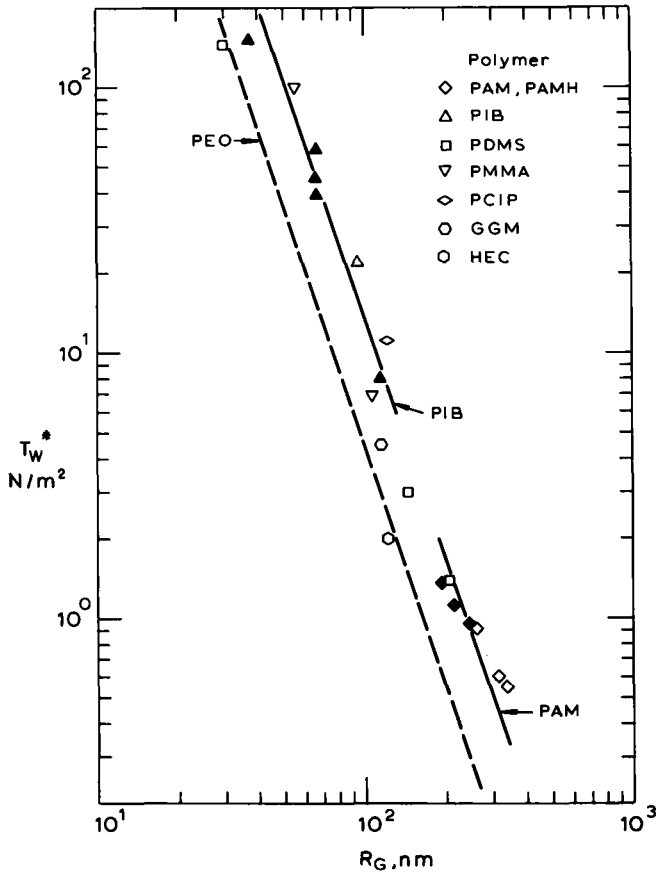

Fig. 4. Onset results for some linear, random-coiling macromolecules. Polymer abbr. as in Table 1, data from Table 2. The dashed line represents PEO, from Figure 3; the two solid lines represent PIB and PAM.

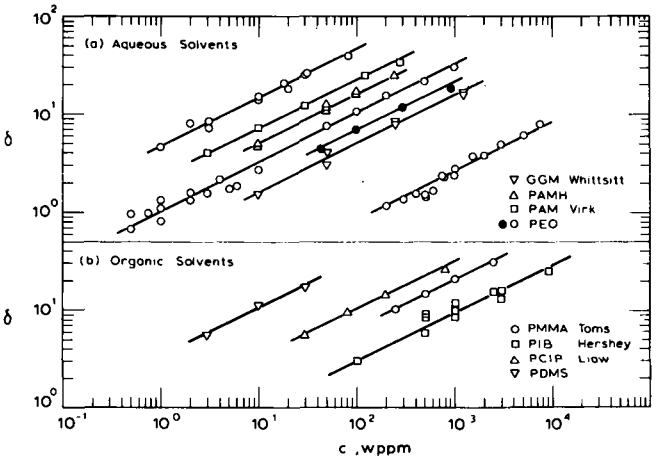

Fig. 5. The effect of polymer concentration on slope increment in (a) aqueous and (b) organic solvents. See Table 2 for experimental details. Solid circles in Figure 5a correspond to data of Figure 2b.

$$\Pi = \kappa N^{3/2} \qquad (6)$$

with slope modulus $\kappa = 70 \times 10^{-6}$ for $5 \times 10^3 < N < 5 \times 10^5$, this intrinsic slope increment correlation being depicted by the solid line in the figure. However, the cellulosic backbone polymers, guargum and hydroxyethylcellulose, with slope moduli $\kappa = (1400 \pm 200) \times 10^{-6}$, lie distinctly apart from the polymethylene group. Thus, for a given polymer species, the intrinsic slope increment increases as the three-halves power of the number of backbone chain links per macromolecule with proportionality constant apparently dependent upon the species skeletal structure.

1.1.5 Maximum Drag Reduction. The maximum drag reduction that can be achieved appears to be limited by a rather unique asymptote which is illustrated in Figure 7, P-K coordinates. The 450-wppm PEO solution in a 32.1-mm I.D. pipe (solid circles) exhibits an interesting gross flow trajectory. For $300 < Ref^{1/2} < 400$, these data lie on the Prandtl-Karman line, slope 4.0; at $Ref^{1/2} \simeq 400$, there is the onset of drag reduction, and for $400 < Ref^{1/2} < 1000$ the data describe a curve of average slope $\simeq 50$; then at $Ref^{1/2} \simeq 1000$ there is a perceptible change of slope, and for $Ref^{1/2} > 1000$ the data lie on a line of slope $\simeq 20$. Another kind of behavior is exhibited by the 110-wppm PAM solution in an 8.46 mm I.D. pipe (solid squares). These data obey Poiseuille's law for $60 < Ref^{1/2} < 150$, then peel away downward from Poiseuille's law and for $Ref^{1/2} > 300$ describe a straight line, slope $\simeq 20$, which is essentially the same as that eventually reached in the first example. This asymptote of maximum drag reduction is also attained by the remaining three examples

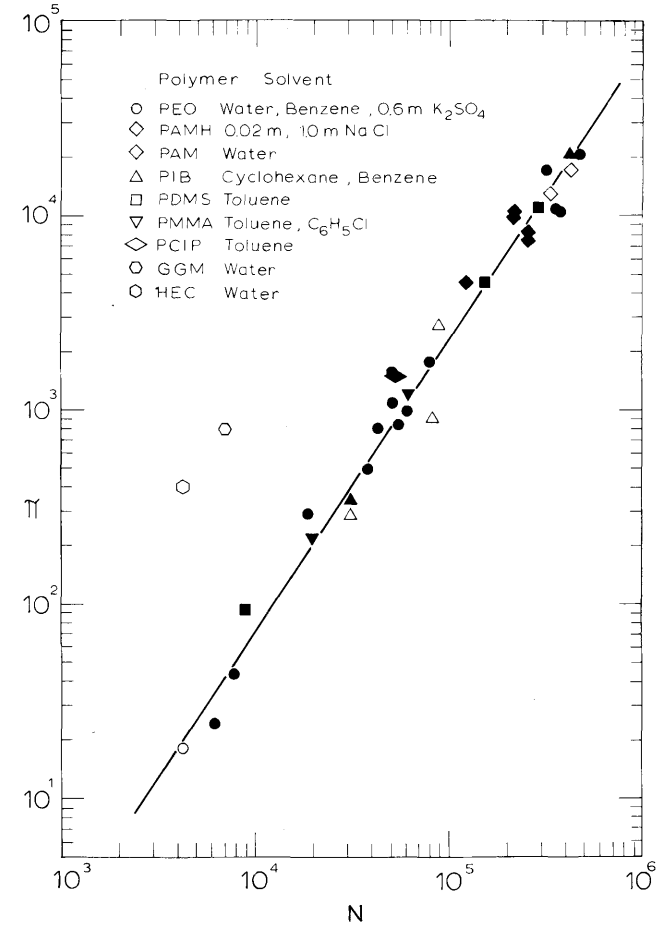

Fig. 6. Relationship between intrinsic slope increment and number of backbone chain links for some linear, random-coiling macromolecules. Solid line corresponds to a slope modulus $\kappa = 70 \times 10^{-6}$. Data from Table 2.

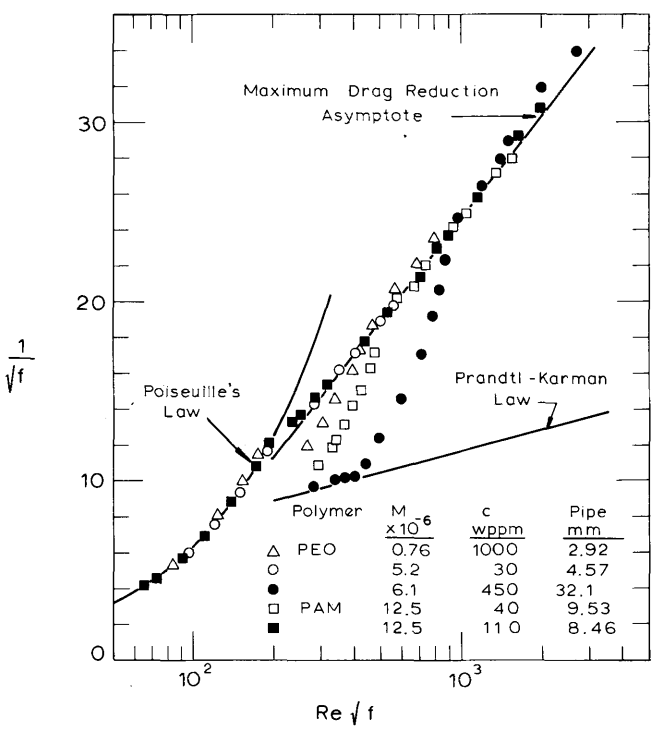

Fig. 7. Gross flow trajectories exhibiting maximum drag reduction. In all cases solvent was distilled water, temperature 25 C. (Polymer, M $\times 10^{-6}$, c wppm, d mm) as follows: (PEO, 0.76, 1000, 2.92), (PEO, 5.2, 30, 4.57), (PEO, 6.1, 450, 32.1), (PAM, 12.5, 40, 9.53), (PAM, 12.5, 110, 8.46).

shown in Figure 7, despite differences among their trajectories at the lower $Ref^{1/2}$. Perusal of the experimental details associated with the data of Figure 7 will show that, besides being independent of pipe diameter, the asymptotic maximum drag reduction is strikingly insensitive to polymer species, molecular weight, and concentration, which contrasts with the pronounced dependence of drag reduction on these polymeric parameters witnessed in the preceding polymeric regime. The maximum drag reduction asymptote has been widely observed and seems to be a fundamental feature of the drag reduction phenomenon. Some recent results are presented in Figure 8, P-K coordinates, in which the solid line labeled *mdr asymptote* corresponds with Equation (4) of the text. The magnitudes of maximum drag reduction are worth noting. At $Ref^{1/2} = (300, 1000, 3000)$, the respective fractional flow enhancements relative to Newtonian are $S_F = (0.54, 1.12, 1.49)$; at the corresponding $Re = (4.4 \times 10^3, 2.5 \times 10^4, 10^5)$, the respective fractional drag reductions relative to Newtonian are $R_F = (0.52, 0.73, 0.80)$.

1.1.6 Transition. The transition from laminar to turbulent flow with dilute polymer solutions can be appreciated by observing first some of the gross flow trajectories depicted in Figures 1 and 7. In Figure 1, the polymer solution shows the laminar, Newtonian, and polymeric regimes, an LNP trajectory, while in Figure 7 we observe two LPM trajectories, for the 38 wppm PAM solution (hollow squares) and for the 1000 wppm PEO solution (hollow diamonds), and two LM trajectories, for the 300 wppm PEO solution (triangles) and the 100 wppm PAM solution (solid squares). Evidently, the existence of one laminar and three turbulent flow regimes makes for three possible laminar-to-turbulent transitions, which we designate $L \rightarrow N$, $L \rightarrow P$, $L \rightarrow M$, respectively. These seem to have the following characteristics:

1. $L \rightarrow N$. The transition with polymer solution is pre-

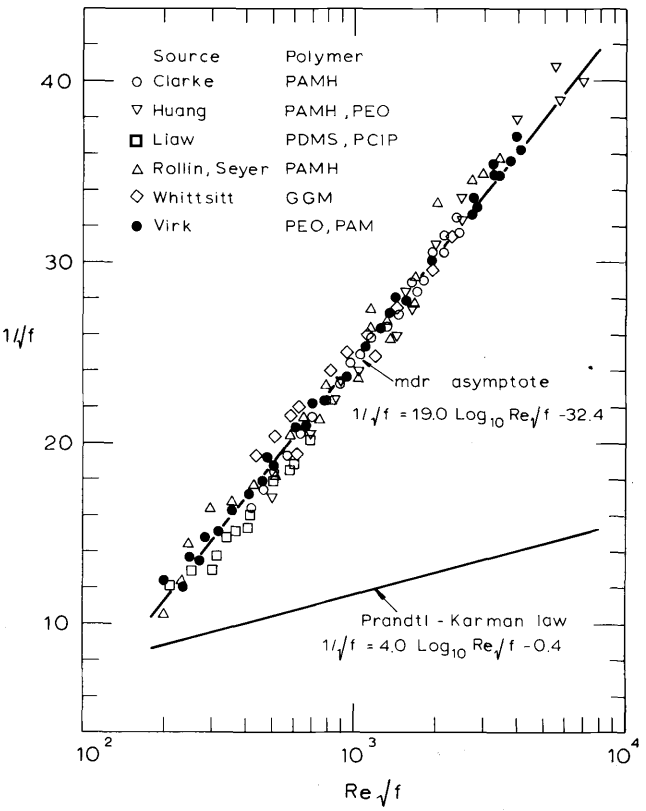

Fig. 8. The maximum drag reduction asymptote in pipe flow of polymer solutions. See Table 4 for experimental details.

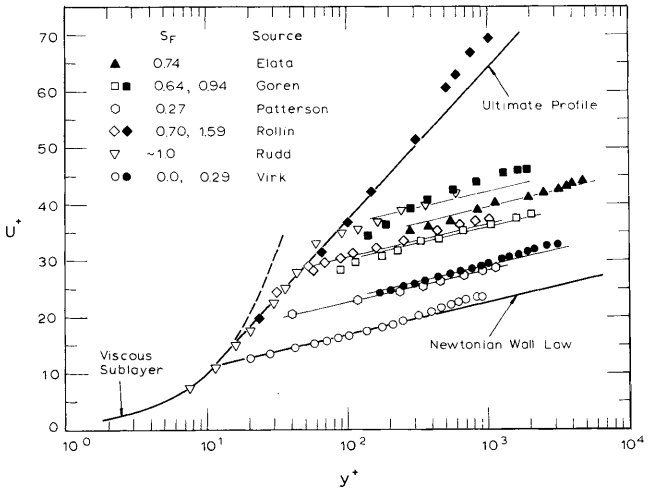

Fig. 9. Mean velocity profiles during drag reduction. See Table 5 for experimental details.

cisely the same as in the usual Newtonian case (Rotta, 1956). There is a critical Reynolds number Re_{tr}, which marks the beginning of a regime of intermittent laminar and turbulent slugs that finally terminates in fully turbulent flow.

2. $L \rightarrow P$. This transition is very similar to Newtonian, with much the same critical Reynolds number, turbulent slug lengths, and growth rates. However, the turbulent slug formation frequency seems to be greater than Newtonian and increases with the drag-reducing ability of the polymer solution.

3. $L \rightarrow M$. In this transition, exhibited by very strongly drag-reducing solutions, velocity fluctuations are apparent at $Re \simeq 1500$, decidedly lower than the Newtonian $Re_{tr} = 2000$, but intermittency cannot be readily discerned.

The kind of transition observed apparently depends upon whether or not the onset of drag reduction occurs in the turbulent slugs which appear for $Re > Re_{tr}$. Also, Re_{tr} in polymer solutions appears always to be equal to or less than Re_{tr} in solvent; in no case do the polymer solutions delay transition. It should be pointed out that the preceding summarize our data for triggered (that is, high inlet disturbance) transition in pipes (Ohara, 1968) and agree substantially with the conclusions of Paterson and Abernathy (1972), but are contrary to those of Castro and Squire (1967), Giles and Pettit (1967), and White and McEligot (1970).

1.2 Mean Velocity Profiles

1.2.1 Law of the Wall. Representative mean velocity data are shown in Figure 9, a law of the wall plot with nondimensional coordinates of U^+ versus log y^+. On the figure, fractional flow enhancement S_F is used to denote the drag reduction. Other experimental details corresponding to the data shown in Figure 9 are contained in Table 5 of Section 2, casual perusal of which will indicate the various pipe sizes, polymers, and concentrations used. The three heavy solid lines in Figure 9 respectively represent the viscous sublayer

$$U^+ = y^+ \tag{7}$$

the Newtonian law of the wall

$$U^+ = 2.5 \ln y^+ + 5.5 \tag{8}$$

and the ultimate profile

$$U^+ = 11.7 \ln y^+ - 17.0 \tag{9}$$

the last arising from the maximum drag reduction asymptote as explained later. Turning to the data, it is seen that, at zero drag reduction (Virk $S_F = 0$), the polymer solution profile adheres to the Newtonian wall law. At low drag reduction (Patterson $S_F = 0.27$, Virk $S_F = 0.29$), the polymer solution profiles are shifted upward from but parallel to the Newtonian wall law. The parallel upward shift, called (after Oldroyd, 1948) the *effective slip* S^+, increases with increasing drag reduction (Goren $S_F = 0.64$, Rollin $S_F = 0.70$, Elata $S_F = 0.74$). At still higher drag reductions (Goren $S_F = 0.94$, Rudd $S_F = 1.0$), an upward shifted region of roughly Newtonian slope is still discernible, but at the lower y^+, toward the wall, the profiles exhibit a slope significantly greater than Newtonian. Finally, at maximum drag reduction conditions (Rollin $S_F = 1.59$), the entire profile is approximately semilogarithmic with a slope $\simeq 12$, about five times that of the Newtonian wall law.

1.2.2 Velocity Defects. A portion of the mean velocity data considered in Figure 9 are shown again in a velocity-defect plot, Figure 10, on arithmetic coordinates of the velocity defect $U_1^+ - U^+$ versus radius-normalized distance from the wall ξ. This is the conventional, and sensitive, method of displaying mean velocity profiles relative to the mean velocity on the pipe axis, the arithmetic abscissa emphasizing the central region of the pipe. The solid line represents the Newtonian velocity defect law including a small, but significant, wake correction as given by Hinze (1959); solvent data reported by the investigators quoted in Figure 10 were all in close agreement with this line but are omitted for clarity. Of the results with polymer solutions, those at the lower, but nevertheless considerable, drag reduction (Virk $S_F = 0.29$, Goren $S_F = 0.64$, Rollin $S_F = 0.70$) show velocity defect profiles identically the same as Newtonian for $1.0 > \xi > 0.05$. As drag reduction is increased (Goren $S_F = 0.94$), the velocity defect remains Newtonian toward the axis $1.0 > \xi > 0.2$ but is greater than Newtonian toward the wall $\xi < 0.2$. At maximum drag reduction (Rollin $S_F = 1.59$), the velocity defect exceeds Newtonian over the entire pipe cross section. Evidently, the mean velocity profiles retain a Newtonian velocity defect structure over a region, $1 > \xi > \xi_e$, which we will call the *Newtonian plug*, the inner (wall-ward) boundary of which ξ_e moves progressively toward the pipe axis $\xi = 1$ with increasing drag reduction. Too, the Newtonian defect structure is retained despite absolute velocities significantly, and by various amounts, higher than Newtonian as already seen in the parallel upward shifts exhibited by these profiles in Figure 9.

1.2.3 Velocity Profile Zones. The characteristic feature of mean velocity profiles during drag reduction seems to be the appearance of a region, lying somewhere between the viscous sublayer and the outer Newtonian plug, in which the mean velocity increases to above Newtonian by an amount S^+. While such a region, which we will call the *elastic sublayer*, can actually be seen in the data of Rudd (1969), roughly $15 < y^+ < 60$ in Figure 9, other profiles at lower drag reduction do not extend close enough to the wall to make it visible. However, from the pipe axis inward, these profiles are observed to be parallel-shifted upward from Newtonian by S^+, and from the wall outward we have the conviction that, in polymer solutions as in Newtonian fluids, the profiles must start out along a viscous sublayer and, hence, between the viscous sublayer and the Newtonian plug must be a region, characteristic of drag reduction, across which the effective slip occurs. Mean velocity profiles during drag reduction have thus three zones from the wall outward: (1) a viscous sublayer, (2) an elastic sublayer, characteristic of drag reduction, across which the effective slip S^+ occurs, and (3) a Newtonian plug which retains the Newtonian defect structure though absolute velocities

in it uniformly exceed Newtonian by S^+. With increasing drag reduction, as Figure 10 showed, there is a progressive shrinkage of the Newtonian plug region, its inner boundary retreating toward the pipe axis until, at maximum drag reduction, the region vanishes. This implies a corresponding increase in elastic sublayer extent, advancing outward from the wall until, at maximum drag reduction, it pervades the entire cross section. In Figure 9, notice that the elastic sublayer portion of Rudd's profile almost coincides with the maximum drag reduction profile of Rollin.

1.2.4 Relation to Gross Flow. Finally, we should like to relate the observed velocity profiles to the gross flow results considered earlier. It can be shown that a semilogarithmic velocity profile of the form

$$U^+ = A \ln y^+ + B \tag{10}$$

leads, upon integration, to a friction factor relation

$$f^{-1/2} = \hat{A} \log_{10} Ref^{1/2} + \hat{B} \tag{11}$$

where

$$\begin{bmatrix} A \\ B \end{bmatrix} = \begin{bmatrix} 0.615 & 0. \\ 1.562 & 1.414 \end{bmatrix} \begin{bmatrix} \hat{A} \\ \hat{B} \end{bmatrix} \tag{12}$$

In this way, the Prandtl-Karman law (2) was originally derived from the Newtonian law of the wall (8); the reverse procedure (Virk, Mickley, and Smith, 1970) was used to infer the ultimate mean velocity profile (9) at maximum drag reduction from the asymptote (4). Notice that the ultimate profile has a mixing length constant $X_m = 0.085$ about a fifth of the Newtonian $X_n = 0.4$. Between the limits of zero and maximum drag reduction, at a given $Ref^{1/2}$ or R^+, a parallel upward shift of S^+ above the Newtonian wall law corresponds to a value of $f^{-1/2}$ shifted by $S^+/\sqrt{2}$ above the Prandtl-Karman law, provided the Newtonian plug portion of the resultant profile still occupies most of the pipe cross section. A linear P-K friction factor relation with slope, after onset, exceeding solvent by δ thus corresponds to mean velocity profiles with effective slip S^+ increasing as $\delta \ln(u_T/u_T^*)$; this leads to the polymeric regime gross flow relation (3).

1.3 Turbulence Structure Measurements

1.3.1 Turbulence Intensity. Axial and radial turbulence intensity profiles measured in a square pipe by Logan (1972) are shown in Figure 11a and b, the polymer solution data at $S_F = 0.4$. Both parts of Figure 11 have the same ordinate of turbulent intensity which is here the root mean square turbulent velocity normalized by friction velocity; the abscissae are y^+ in Figure 11a and ξ in Figure 11b, as appropriate for the wall and core regions of the pipe, respectively. Of the data in Figure 11, the solvent (that is, Newtonian) u'^+ and v'^+ profiles are in reasonable accord, as to both magnitudes and shapes, with the classical results of Laufer (1954) and Klebanoff (1955) in air. In the polymer solution, the wall-region plot shows the axial intensity increases in the region $y^+ < 30$, reaches a maximum $u'^+ \simeq 4.3$ at $y^+ \simeq 35$ and then decreases, at first rapidly and then more slowly, with increasing y^+ for $y^+ > 40$. The polymer solution data in the region $20 < y^+ < 30$ of increasing u'^+ lie close to an extension of the straight line, through the origin, which represents the solvent data in the region $10 < y^+ < 20$, suggesting that the slope of the axial intensity profile at the wall, called α^+, during drag reduction is much the same as Newtonian. Considering u'^+ magnitudes relative to solvent, for $0 < y^+ < 20$, u'^+ in polymer solution is, by inference from the slopes, the same as in solvent; for $20 < y^+ < 100$, it can be seen that u'^+ in polymer solution is significantly higher than in solvent, by 55% at $y^+ = 50$ for example, but the difference decreases with increasing distance from the wall; and, for $y^+ > 150$, u'^+ in the polymer solution is essentially the same as in solvent. The radial intensity v'^+ in the polymer solution increases essentialy monotonically from $v'^+ \simeq 0.3$ at $y^+ \simeq 20$ to $v'^+ = 1.1$ at $y^+ = 100$, and in the intervening region v'^+ in polymer solution appears to be slightly lower than in solvent, by about 10% at $y^+ = 50$; for $y^+ > 100$, v'^+ in the polymer solution is constant and approximately equal to v'^+ in solvent. Seen from the pipe axis inward, Figure 11b, both axial and radial turbulence intensities in the polymer solution are identically the same as in solvent (Newtonian) in the central core region, but toward the wall u'^+ is higher than in solvent for $\xi < 0.4$ while v'^+ is lower than in solvent for $\xi < 0.2$.

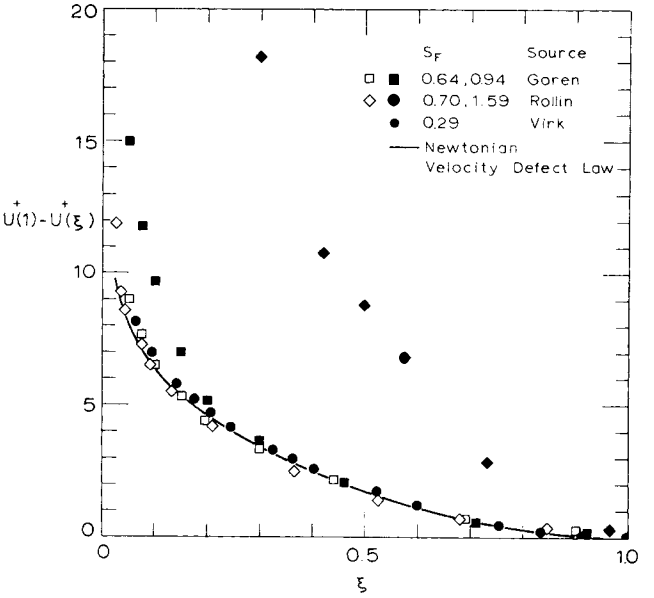

Fig. 10. Velocity defects during drag reduction. See Table 5 for experimental details; solid line is the Newtonian velocity defect law from Hinze (1959).

Other available axial turbulent intensity data, not shown in Figure 11 because of their high scatter, are in general agreement with Logan's results. In the wall region, the data of Rudd (1969) yield an axial intensity profile during drag reduction which is analogous in every respect to that shown in Figure 11a while, in the pipe core, from the axis inward, regions where u'^+ during drag reduction is the same as in solvent can be detected in the data of both Rudd (1969) and Chung and Graebel (1972). In regard to radial turbulent intensity, dye dispersion data of Taylor and Middleman (1974), $S_F \simeq 0.25$, indicate v'^+ identically the same as in solvent in the core region, which

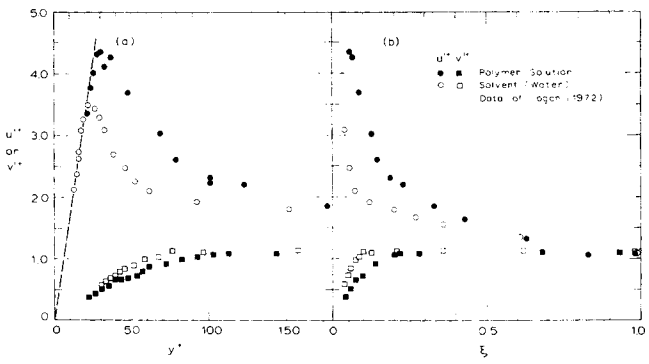

Fig. 11. Axial and radial turbulent intensity profiles during drag reduction in (a) the wall region, and (b) the core region. Data of Logan (1972); see Table 6 for experimental details.

agrees with Logan's results (Figure 11b). Concerning the variation of turbulent intensity profiles with drag reduction, the data of Logan ($S_F \simeq 0.4$) and Rudd ($S_F \simeq 1.0$) respectively yield a ratio of maximum axial intensity in polymer solution to that in solvent ($u_{max,p}'^+/u_{max,n}'^+$) of 1.3 and 1.8, while in the pipe core the regions where u'^+ is the same as in solvent are $1.0 > \xi > 0.4$ and $1.0 > \xi > 0.6$, respectively. At (or near) maximum drag reduction, there is only uncertain information from streak photography (Seyer and Metzner, 1969; Arunachalam, Hummel, and Smith, 1972), which suggests that ($u_{max,m}'^+/u_{max,n}'^+$) is 2.0 to 2.5.

1.3.2 Reynolds Stress and Correlation Coefficient. Reynolds stress data reported by Logan (1972) and u-v correlation coefficients calculated therefrom are shown in parts a and b, respectively, of Figure 12, using a common wall-region abscissa y^+. In Figure 12a the ordinate is the ratio of Reynolds to total shear stress, $\phi = \langle uv \rangle / u_T^2(1 - \xi)$, which is, of course, the ratio of turbulent to total (viscous plus turbulent) axial momentum transport in the radial direction; too, in the wall region under consideration, ξ is small so the total shear stress is close to T_w. The solvent ϕ profile is indicated by the broken line, but unfortunately Logan reported no solvent Reynolds stress data closer to the wall than $y^+ = 65$ so the region $10 < y^+ < 65$ is based on results of Laufer (1954) and Bremhorst and Walker (1973) at comparable R^+. In polymer solution, the data scatter considerably and therefore average values over various y^+ extents have been indicated by steps on the figure. For $10 < y^+ < 80$, ϕ in the polymer solution is less than in solvent, whereas for $y^+ > 80$ it is much the same as in solvent. In Figure 12b, the ordinate is the u-v correlation coefficient C_{uv} with values computed from the experimental Reynolds stress data of Figure 12a and the axial and radial intensity data of Figure 11a. The broken line represents solvent, and the polymer solution data have been averaged as in Figure 12a. It will be noticed that for $20 < y^+ < 80$ the value of $C_{uv} \simeq 0.2$ in the polymer solution is very significantly less than that in solvent, $C_{uv} \simeq 0.44$, whereas for $y^+ > 80$ values of $C_{uv} = 0.4 \pm 0.1$ in the polymer solution are much the same as in solvent. The observed decrease in C_{uv} in the wall region during drag reduction suggests that the polymer molecules reduce turbulent transport by decoupling the axial and radial velocity components rather than by suppressing the intensity of turbulence.

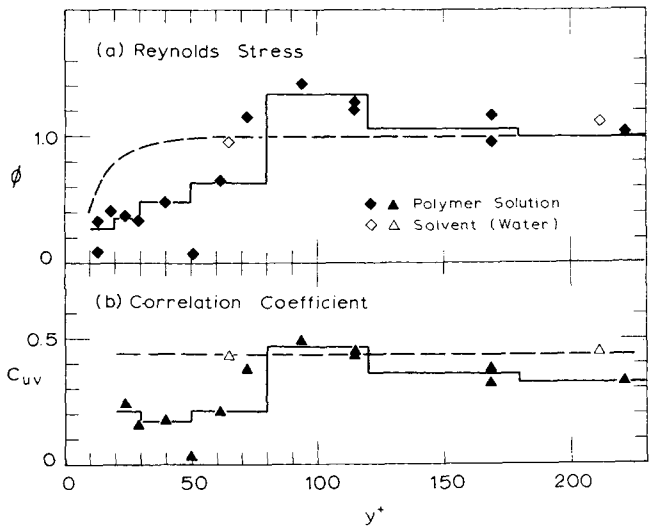

Fig. 12. Wall region profiles of (a) the ratio of Reynolds to total shear stress and (b) the u-v correlation of coefficient during drag reduction. Data of Logan (1972).

1.3.3 Turbulence Structure Zones. The axial intensity profile, for which the most information exists, has three zones:

1. A region $0 < y^+ < y_v^+$, say, in which α^+ and the magnitudes of u'^+ are essentially the same as Newtonian.
2. A region $y_v^+ < y^+ < y_e^+$, say, which is characteristic of drag reduction and in which u'^+ differs from Newtonian, being higher. This region further consists of a relatively thin portion, $y_v^+ < y^+ < y_{max}^+$, in which u'^+ increases to a maximum value and the remaining major portion $y_{max}^+ < y^+ < y_e^+$ in which u'^+ decreases from the maximum to a value close to Newtonian.
3. A region $y^+ > y_e^+$ or $1 > \xi > \xi_e$ in which u'^+ is the same as Newtonian.

The radial intensity, Reynolds stress, and correlation coefficient profiles do not yield information on the very near wall region (1) but do show clearly the region (2), toward the wall, which differs from Newtonian (v'^+, ϕ, C_{uv} are all relatively lower) and region (3), toward the axis, which is much the same as Newtonian.

There is evidently a striking analogy between the above turbulence structure zones and the (1) viscous sublayer, (2) elastic sublayer, (3) Newtonian plug zones of the mean velocity profiles considered earlier.

2. CORRELATION AND ANALYSIS

The object of this section is to correlate drag reduction data, using the elastic sublayer model (Virk, 1971) as a framework. The model is briefly described and then empirically related to experimental gross flow, mean velocity, and turbulence measurements with analysis and discussion of the data used for this purpose, including a section on polymer characterization. The empirical developments are, of course, substantially model independent.

2.1 The Elastic Sublayer Model

The essential physical notion is that the stimulation of polymer molecules by a turbulent shear flow creates a zone, called the *elastic sublayer*, which is characteristic of the drag reduction phenomenon. The elastic sublayer originates at onset, it then grows with increasing drag reduction and eventually occupies the entire pipe cross section at maximum drag reduction. By hypothesis, all drag reduction observations can be related to the properties and extent of the elastic sublayer.

The mean flow model is shown schematically in Figure 13, which defines all terminology. The general profile ABCD, consists of three zones: (1) a viscous sublayer AB, $y^+ \leq y_v^+$; (2) an elastic sublayer BC, $y_v^+ < y^+ < y_e^+$; (3) a Newtonian plug CD, $y_e^+ \leq y^+ \leq R^+$, each with the indicated mixing length constant and U^+-y^+ relationship. The inner edge B of the elastic sublayer stays fixed at $y_v^+ = 11.6$, which is the trisection of Equations (7), (8), and (9), while its outer edge C moves along the ultimate profile BM from y_v^+ at zero drag reduction to R^+ at maximum drag reduction. Comparison of Figure 9 with Figure 13 shows that the model reproduces the essential features of the experimentally observed mean velocity profiles. The effective slip is related to elastic sublayer thickness by

$$S^+ = (A_m - A_n) \ln (y_e^+/y_v^+) \qquad (13)$$

Integration of the profile ABCD by segments yields the friction factor relations:

$$U_{av}^+ = A_n \ln R^+ + B_n - 1.5\,A_n \quad ; y_e^+ \to y_v^+ \qquad (14a)$$

$$= A_n \ln R^+ + B_n - 1.5\,A_n + (A_m - A_n) \ln (y_e^+/y_v^+); y_v^+ < y_e^+ < R^+ \qquad (14b)$$

$$= A_m \ln R^+ + B_m - 1.5\,A_m \quad ; y_e^+ \to R^+ \qquad (14c)$$

respectively representing the Newtonian, polymeric, and maximum drag reduction regimes. We now postulate a dependence of elastic sublayer thickness on flow and polymeric parameters which is physically motivated by the observation that two kinds of factors appear to influence drag reduction in the polymeric regime. One factor, reflected by onset and the affine, linear P-K plots obtained thereafter, seems to concern the excitation of the macromolecule by the turbulent flow while a second factor, reflected by the P-K slopes, apparently involves the amount of polymer present. In the expressions

$$\ln(y_e^+/y_v^+) = 0 \quad ; (R^+/R^{+*}) < 1 \quad (15a)$$

$$= \psi \ln (R^+/R^{+*}); \quad (15b)$$

$$= \ln (R^+/y_v^+) \quad ; (R^+/R^{+*}) > (R^{+*}/y_v^+)^{1/(\psi-1)} \quad (15c)$$

the operational member (15b) contains these factors, ψ and $\ln (R^+/R^{+*})$, in separable form while the auxiliary relations (15a and c) respectively ensure the proper crossovers to the Newtonian and maximum drag reduction asymptotes. Substitution of (15b) into (14b) yields

$$U_{av}^+ = (A_n + \psi(A_m - A_n)) \ln R^+ + B_n - 1.5\,A_n - \psi(A_m - A_n) \ln R^{+*} \quad (16)$$

which is synonymous with the polymeric regime relation (3), the P-K slope increment being $\delta = 1.626\,\psi(A_m - A_n)$ while the onset wave number is $W^* = (2R^{+*}/d) = (T_w^*/\rho)^{1/2}/\nu$. Thus, the elastic sublayer thickness, (15b), is uniquely related to the parameters T_w^* and δ, both of which are directly accessible from gross flow experiments, and our task is to seek their respective dependencies upon macromolecular properties.

2.2 Polymer Characterization

Table 1 presents characterization information for some of the polymers which have been used in drag reduction studies. The molecular weight per backbone chain link, the unperturbed effective bond length per backbone chain link, and the chain conformation factor for each species are given in columns 3 to 5, respectively. Columns 7 to 9 summarize Mark-Houwink relationships

$$[\eta] = KM_w^a \quad (17)$$

between intrinsic viscosity and molecular weight. The quantity H in column 10 of Table 1 is a heterogeneity index, derived from light-scattering experiments on the commercial polymer samples named in column 11. Its definition

$$H = 31 \times 10^{23}\, R_G^3/M_w[\eta] \quad (18)$$

arises from Flory's (1953) viscosity relation. The numerical constant in (18) is $(0.8)6^{3/2}\Phi$, with $\Phi = 2.66 \times 10^{23}$ (Pyun and Fixman, 1966) and the factor 0.8 to account (Yamakawa, 1971) for the use of good (rather than theta) solvents in most drag reduction studies. Values of R_G and M_w obtained by light-scattering are, respectively, 'z' and 'weight' averages (see, for example, McIntyre and Gornick, 1964) while $[\eta]$ is essentially a weight-averaged quantity, that is, H is a ratio of third to second moments of the same distribution, and hence we can ascribe $H > 1$ to polymer sample heterogeneity. In principle, H can be computed from a known molecular weight distribution; for example, the most probable distribution (Flory, 1953) yields $H \simeq 2.0$ which should be an approximate lower bound for all unfractionated polymers. By the converse, the value of H, computed by (18) from a triad of experimental R_G, M_w, and $[\eta]$ measurements on a polymer sample, is an empirical index of its unknown

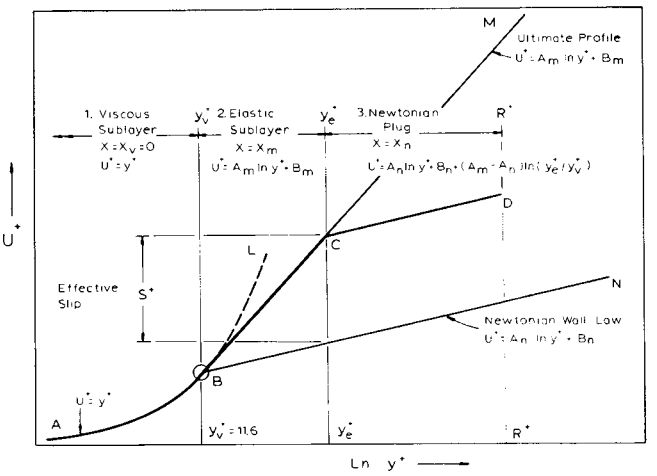

Fig. 13. Schematic of the mean velocity profile during drag reduction according to elastic sublayer model.

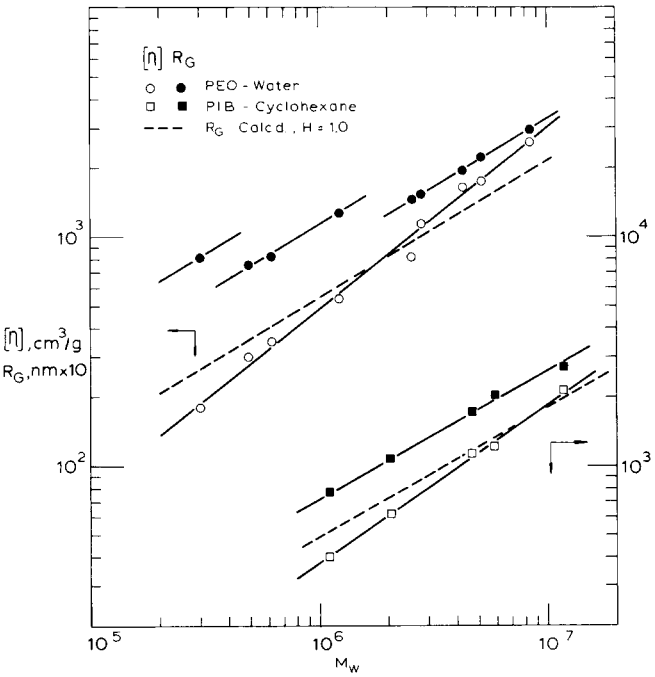

Fig. 14. Polymer characterization by viscosity and light-scattering. (a) PEO-Water (Shin, 1965); (b) PIB-Cyclohexane (Shin, 1965; Cottrell, 1968).

molecular weight distribution. The latter implicit connection nurtures the hope that a given commercial polymer family might possess characteristic H values.

The derivation of H from experimental data is illustrated in Figure 14, abscissa M_w, ordinates either $[\eta]$ or R_G, all logarithmic. Consider first the lower portion, right-hand ordinate, for the PIB-cyclohexane system (Shin, 1965; Cottrell, 1968). The hollow squares represent ($[\eta]$, M_w) pairs, and the solid line fitted to them corresponds to the Mark-Houwink relationship given in Table 1, entry 7; it is worth noting that these data agree well with established results (Flory, 1953) for the same system. The dashed line represents the calculated R_G versus M_w for $H = 1$, obtained from (17) and (18), and it can be seen that the experimental (R_G, M_w) pairs, solid squares, all lie above the dashed line. The solid line fitted to the experimental $R_G - M_w$ data is parallel to but a factor of 3 higher than the dashed line, that is, $H = 3$ for all five members of the PIB family studied. The upper portion of Figure 14, left-hand ordinate, refers to the PEO-water

TABLE 1. CHARACTERIZATION OF POLYMERS USED IN DRAG REDUCTION STUDIES

Entry	Polymer	m_0	b_0 nm	σ	Solvent	K cm³/g	a	M_w range	H	Trade names of polymers used	Sources
1	PEO	14.7	0.32	1.6	Water	0.00875	0.79	0.30-8.45	3.5	Polyox WSR 301, Coagulant, (FRA)	Shin (1965)
2									9.2	WSR 205, N3000, N750	
3									29	WSR N80, (WSR 35, N10)	
4	PEO				Benzene	0.0397	0.686		—	—	Beech (1969)
5	PAM	35.5	0.50	2.3	Water	0.0373	0.66	0.8-4.0	6.0	Cyanamer P250, P100, (E198, E117)	Lee (1966)
6	PAMH	(35.5)	0.50	2.3	1.0m NaCl	0.0418	0.66	1.0-10.0	2.8	Separan NP20, AP30	Clarke (1971)
7	PIB	28	0.39	1.8	Cyclohexane	0.0270	0.69	1.0-15	3.0	Vistanex L-80, 140, 200, 250, 300	Shin (1965), Cottrell (1968)
8	PDMS	37	0.42	1.4	Toluene	0.0215	0.65	—	—	—	—
9	PMMA	50	0.41	1.9	Toluene	0.0071	0.73	0.4-3.3	—	—	Chinai (1955)
10	PCIP	34	0.46	1.6	Toluene	0.0502	0.667	0.07-1.0	—	—	—
11	GGM	243	2.4	3.0	Water	$(M_w, R_G) = (1.72 \times 10^6, 115\,\text{nm})$			—	'Commercial Sample'	Deb (1963)
12	GTA	432	2.4	3.0	Acetonitrile	0.00262	0.87	0.07-0.85	—	—	Koleske (1964)
13						0.311	0.52	0.85-5.34	2.0	—	Koleske (1964)
14	HEC	(236)	2.8	3.6	Water	0.00948	0.87	0.08-0.63	2.2	—	Brown (1963)
15						1.3	0.50	>0.35	4.2	Cellusize WP4400, (QP1000M)	After Brown (1961)

1. Polymer abbreviations are as follows: PEO (polyethyleneoxide), PAM (polyacrylamide, homopolymer), PAMH (polyacrylamide, partially hydrolyzed), PIB (polyisobutylene), PDMS (polydimethylsiloxane), PMMA (polymethylmethacrylate), PCIP (polycisisoprene), GGM (guar gum), GTA (guaran triacetate), and HEC (hydroxyethylcellulose).
2. Values of m_0 in parentheses are approximate. PAMH samples of Clarke (1971) estimated 30% hydrolyzed; HEC sample of Brown (1961) had 1.67 moles ethylene oxide per anhydroglucose unit with degree of substitution 0.88 (maximum = 3.0).
3. Unperturbed dimensions, b_0 and σ, are from the following sources: PEO (Beech and Booth, 1969), PAM and PAMH (estimated from Stockmayer-Fixman plot of data from Lee, 1966 and Clarke, 1971), PIB, PDMS, and PMMA (Flory, 1969), PCIP (Yamakawa 1971), GGM (assumed same as GTA), GTA (Koleske and Kurath, 1966), and HEC (Brown, Henley, and Ohman, 1963).
4. Mark-Houwink constants for entries 8 and 10 from Brandrup (1966).
5. Polymer trade names according to following manufacturers: Polyox Water Soluble Resins (Union Carbide Co.), Cyanamer (American Cyanamid Co.), Separan (Dow Chemical Co.), Vistanex (Enjay Chemical Co.), Cellusize (Union Carbide Co.).
6. Polymers named in parentheses, for example, (FRA) in entry 1, have not been characterized.
7. For brevity, only lead authors are named in Sources column.
8. Cottrell (1968), entry 7, reported results for PIB in cyclohexane and decahydronaphthalene; a small adjustment, via $(\alpha_{\eta,cyc}/\alpha_{\eta,dec}) = 1.02$, has been made in using data obtained in the latter solvent.

system (Shin, 1965). The $[\eta] - M_w$ data, hollow circles, for all of the PEO polymer samples are fitted by the solid line, which corresponds with the Mark-Houwink constants given in Table 1, entry 1; these data are in fair agreement with earlier results for the PEO-water system (Bailey and Callard, 1959). The $R_G - M_w$ data, solid circles, seem to separate into three distinct families, entries 1, 2, 3, respectively, in Table 1, of strikingly different heterogeneities. The solid lines fitted to each $R_G - M_w$ family have all been drawn with the same slope and can be seen to well represent the two higher molecular weight families.

Of the cellulosic polymers, the only available data for GGM in water appear to be those of Deb and Mukherjee (1963) on a single commercial sample; in Table 1, entry 11 gives their reported M_w and an R_G calculated from their dissymmetry data. Some results from a detailed study of the guarantriacetate-acetonitrile system (Koleske and Kurath, 1964) are given in entries 12 and 13, the different Mark-Houwink constants apparently reflecting a change in the GTA random-coil from partially free-draining for $N < 1900$ to nonfree-draining for $N > 1900$. Interestingly, when R_G is plotted against N, Deb and Mukherjee's (1963) point for GGM-water accords well with Koleske and Kurath's (1964) data for GTA-acetonitrile. Table 1, entry 14, lists the results obtained by Brown, Henley, and Ohman (1963) for fractionated samples of HEC in water. Scrutiny of these and earlier (Brown, 1961) data on a Stockmayer-Fixman plot (Yamakawa, 1971) suggests that the HEC random-coil also probably undergoes a change in drainage characteristics at $N \simeq 1500$. For $N > 1500$, the estimated nonfree-draining Mark-Houwink constants given in entry 15 are recommended; also, entry 15 provides a value of H for a commercial HEC, estimated from the fractionation and light-scattering data of Brown (1961), but this is possibly too low owing to loss of some of the highest molecular weight fractions.

2.3 Gross Flow Correlations

2.3.1 Polymeric Regime. Table 2 summarizes some data for drag reduction in the polymeric regime. Columns 3 to 7 contain characterization information consisting of the polymer used, the solvent, and $[\eta]$, from which, in most cases, M and then R_G have been obtained via Table 1. Column 8 gives the pipe inside diameter. Columns 9, 10, and 11, respectively, give the number of gross flow runs with polymer solutions and the limits of the concentration range examined. Columns 12 and 13 respectively contain the drag reduction parameters T_w^* and $\delta/c^{1/2}$ derived from the data along with their approximate error limits. Experimentally, both T_w^* and $\delta/c^{1/2}$ are found to depend only weakly on polymer concentration so that a set of these parameters is representative of all dilute solutions of a given polymer-solvent pair and pipe.

Items in Table 2 requiring explanation are noted. For all entries using polymers PMMA, PCIP, and PDMS, R_G have been obtained by assuming $H = 3.0$, and in entries 12 to 17 it is assumed that both kerosene and crude oil are theta solvents for PIB. The GGM-water data showed a rather remarkable consistency, with $T_w^* = 4 \pm 2$ and $\delta/c^{1/2} = 0.60 \pm 0.15$ representing entries 79 to 88, which suggests the use of very similar polymers, and we have therefore assigned the (M_w, R_G) of Table 1, entry 11, to all cases; the assignment differs from an earlier $M = 0.2 \times 10^6$ based on manufacturer's estimates. Where the same polymer sample was used in two solvents, i and j, for example, the entry pairs (5, 6), (35, 36), (71, 72), M_i and $R_{G,i}$ were calculated from Table 1 and in the second solvent, we set $M_j = M_i$ and obtained $R_{G,j} = R_{G,i}\,([\eta]_j/[\eta]_i)^{0.4}$, assuming $\alpha_\eta^3 = \alpha_R^{2.5}$ (Yamakawa, 1971). Attention is drawn to the use of recirculating flow systems by a trailing R in column 8 because these are more prone to polymer degradation effects than once-through flow systems. In these cases, it is likely that the experimentally obtained T_w^* are higher and $\delta/c^{1/2}$ lower than appropriate for the quoted polymer characterizations which represent the original, undegraded polymer samples. For the majority of entries, T_w^* and $\delta/c^{1/2}$ were derived from the same gross flow runs so that columns 9 to 11 apply to both parameters, but there are trivial exceptions: for example, in entry 57, T_w^* was derived from data of 10 solutions, $50 < c < 2000$, as listed, but $\delta/c^{1/2}$ was obtained from 13 solutions, $10 < c < 3000$. There are two major sources of uncertainty in the experimental determinations of T_w^* and δ. The statistical uncertainty, for example

$$v(T_w^*) = 100$$

$[\text{var}\,(T_w^*)]^{1/2}/T_w^*$, can be estimated by assuming that pressure drop and flow rate measurements are respectively accurate to within $\pm 1\%$ and $\pm 0.5\%$, as in the very best data. Error analysis then shows that, for polymer solutions exhibiting slope increments $\delta = (1, 2, 5, 10, 20)$, respectively, the corresponding $\epsilon(T_w^*) = (70, 40, 20, 13, 9)\%$ and $\epsilon(\delta) = (35, 18, 8, 4, 2)\%$: that is, on statistical grounds alone, T_w^* can at best be known to within $\pm 10\%$ and uncertainties of order $\pm 100\%$ are possible for feebly drag-reducing solutions. For T_w^* (and for δ) to qualify as a flow scale, the turbulent flow should be well developed at the onset. An obvious minimum requirement is that laminar-to-turbulent transition be complete at, say, 200 diameters from the pipe inlet. Thus, for $Ref^{1/2*} < 300$ ($Re^* < 3000$), the corresponding T_w^* is always unreliable and the few such in Table 2 are put in parentheses. For $Ref^{1/2*} > 500$, T_w^* is expected to be free of transitional flow uncertainties (unless special precautions have been taken to eliminate inlet disturbances in which case, of course, laminar pipe flow can persist to indefinitely high Re). For $300 < Ref^{1/2*} < 500$, inlet flow conditions must be known to assess T_w^*; we assume that T_w^* is acceptable when $Ref^{1/2*} > 300$ for triggered inlets, and when $Ref^{1/2*} > 400$ for square cut-off pipe inlets. It should be noted that a proper criterion of turbulent flow development, that is, the existence of a region of inner-outer flow overlap which requires $y^+ \simeq 50$ at $\xi \leq 0.15$, or $Ref^{1/2*} > 1000$, is met by few entries.

Table 2 coalesces and brings up to date our previous tabulations (Virk et al., 1966, 1967; Virk and Merrill, 1969; Virk, 1971) on the present subject. It is believed to be somewhat of an improvement on the earlier works by virtue of better polymer characterization and, in the majority of entries, determination of self-consistent onset and slope increment values from the same P-K plot of the original data. Among recent literature incorporated, the following are noteworthy. Paterson and Abernathy (1970) and Hansen and Little (1971) present further, precise data for PEO-water, Clarke's (1971) investigation using PAMH is the first with control over the polyelectrolyte conformation, and Wang (1972) presents some of the first results with characterized cellulosic polymers.

2.3.2 Onset Constants. We examine the onset data in Table 2 to obtain the dependence of T_w^* on pipe diameter, polymer concentration, solvent viscosity, and polymer radius of gyration, respectively, thus leading to an onset correlation. Two methods have commonly been used to define onset. The visual method simply adjudges the onset point as that where polymer solution gross flow data depart from solvent on, say, a plot like Figure 1, whereas the slope method requires a fitting of both polymer solution and solvent data to appropriate straight lines, the intersection of which is considered the onset point. Values of

TABLE 2. SUMMARY OF POLYMERIC REGIME DATA

Entry	Source	Polymer	Solvent	$[\eta]$ cm^3/g	M $\times 10^{-6}$	R_G nm	Pipe I.D., mm	Runs	c range, wppm	T_w^*, N/m^2	$\delta/c^{1/2}$
1	Toms (1948)	PMMA	Chlorobenzene	390	3.1	106	4.04	4	230-2,300	7.0 ± 1.0	0.69 ± 0.06
2	Hershey (1967)	PMMA	Toluene	170	1.0	55	0.81	2	5,500-9,000	(115)	0.25 ± 0.01
3							1.17	2	5,500-9,000	85	0.17 ± 0.04
4							12.9 R	3	1,000-9,000	100 ± 40	0.22 ± 0.05
5		PIB	Benzene	82	0.89	37	12.9 R	2	2,500-9,000	150 ± 40	0.30 ± 0.03
6		PIB	Cyclohexane	344	0.89	66	1.17	3	100-1,000	39 ± 7	0.36 ± 0.06
7							12.9 R	3	500-3,000	58 ± 15	0.35 ± 0.05
8							25.4 R	2	1,000-3,000	45 ± 15	—
9	Rodriguez (1967)	PIB	Toluene	420	2.3	95	1.17	2	500-1,000	22	0.60 ± 0.15
10	Patterson (1968)	PIB	Cyclohexane	664	2.3	114	25.4 R	2	2,000-4,000	8.0 ± 1.5	0.51 ± 0.10
11	Shin (1965)	PIB	Cyclohexane	2,050	11.8	—	2.17 R	5	0.32-2.2	—	6.0 ± 1.0
12	Ram (1967)	PIB	Kerosene	—	(1.4)	(55)	3.2 R	3	155-205	63 ± 12	—
13					(2.5)	(74)	to	4	150-280	28 ± 8	1.7
14					(5.0)	(105)	13.7 R	5	190-800	18 ± 8	1.5 ± 0.5
15		PIB	Crude oil		(1.4)	(55)	10.2 R	1	200	70	—
16					(2.5)	(74)	10.2 R	1	200	52	1.7
17					(5.0)	(105)	10.2 R	1	220	17	1.3
18	Liaw (1968)	PCIP	Toluene	400	0.71	65	0.83	1	80	120 ± 20	0.38 ± 0.10
19				850	2.2	122	2.72	3	30-200	14 ± 5	1.01 ± 0.25
20							13.0 R	1	800	11.2	0.71
21							25.4 R	1	800	11.0	0.83
22		PDMS	Toluene	84	0.33	30	0.83	2	2,000-6,000	143 ± 10	0.16 ± 0.01
23				530	5.7	143	2.72	2	30-80	3.0 ± 0.5	1.90 ± 0.11
24							13.0 R	1	800	4.5	0.68
25							25.4 R	1	800	3.6	0.72
26				800	10.8	203	2.72	2	3-10	1.4 ± 0.3	3.34 ± 0.42
27		PEO	Benzene	78	0.063	36	0.83	1	4,000	150	0.071
28				250	0.35	93	2.72	2	80-200	5.1 ± 0.5	1.12 ± 0.05
29				450	0.81	103	2.72	3	80-500	6.5 ± 2.5	0.93 ± 0.10
30				1,270	3.7	175	2.72	1	30	(2.9)	2.92
31	Shin (1965)	PEO	Dist. water	330	0.62	—	2.17 R	4	3.5-310	—	0.93 ± 0.20
32				1,650	4.7	—	2.17 R	3	0.29-2.2	—	7.8 ± 0.3
33	Berman (1974)	PEO	Water	180	0.29	79	6.35	1	425	7.0	—
34		PEO	53% Glycerol	130	0.29	69	6.35	1	425	(10)	—
35	Pruitt (1966)	PEO	Water	200	0.33	85	4.57	3	10-250	6.5	—
36			0.6m K_2SO_4	79	0.33	59	4.57	3	10-250	15.5	—
37			Water	390	0.76	96	4.57	3	10-250	5.0 ± 2.0	1.82 ± 0.20
38			0.6m K_2SO_4	145	0.76	65	4.57	3	10-250	14.5 ± 4.0	1.79 ± 0.20
39			Water	1,300	3.5	174	4.57	3	2-50	(1.5)	—
40			0.6m K_2SO_4	429	3.5	112	4.57	3	2-50	5.2	—
41	Goren (1967)	PEO	Water	—	—	—	50.8	5	2-50	0.15 ± 0.02	5 ± 4
42	Little (1967)	PEO	Dist. water	281	0.50	110	9.53	2	100-500	1.6	1.4 ± 0.2
43	McNally (1968)	PEO	Dist. water	1,590	4.5	203	20.0	4	2-40	(0.45)	4.7 ± 0.2
44							37.6	2	10-20	0.45 ± 0.1	—
45	Paterson (1970)	PEO	Dist. water	300	0.55	116	17.4	3	1-50	1.5 ± 0.6	1.5
46				310	0.57	81	6.30	1	75	10.4	—
47				350	0.66	89	6.30	1	75	5.2	—

TABLE 2. SUMMARY OF POLYMERIC REGIME DATA (cont'd.)

Entry	Source	Polymer	Solvent	$[\eta]$ cm^3/g	$M \times 10^{-6}$	R_G nm	Pipe I.D., mm	Runs	c range, wppm	T_w^*, N/m^2	$\delta/c^{1/2}$
48				380	0.74	94	17.4	1	50	3.3	0.86
49				550	1.18	125	17.4	3	1-50	1.2 ± 0.5	1.75
50				2,700	8.8.	302	17.4	4	1-50	0.4 ± 0.2	6.0 ± 0.4
51	Hansen (1971)	PEO	Dist. water	443	0.89	106	6.60	3	3-57	1.8 ± 0.7	1.04 ± 0.30
52							25.3	2	3-9	2.0 ± 0.3	1.02
53				2,260	7.02	—	6.60	2	1-3	—	7.8 ± 0.5
54	Virk (1966-71)	PEO	Dist. water	66	0.080	37	32.1 R	3	1,000-5,000	40 ± 10	0.04 ± 0.01
55				73	0.091	40	2.92	9	500-7,500	35 ± 5	0.080 ± 0.015
56				88	0.12	46	8.46	2	2,000-6,000	26.5 ± 5	0.13 ± 0.01
57				175	0.28	77	2.92	10	50-2,000	8.0 ± 1.0	0.55 ± 0.05
58				310	0.57	81	8.46	4	40-1,000	7.2 ± 1.0	0.67 ± 0.04
59				338	0.63	86	2.92	6	20-1,000	8.0 ± 1.0	1.01 ± 0.15
60				361	0.69	91	32.1 R	4	50-1,000	5.5 ± 1.0	0.54 ± 0.05
61				390	0.76	96	2.92	6	10-500	5.0 ± 1.0	1.25 ± 0.05
62				550	1.18	125	9.45	5	3-300	1.9 ± 0.5	1.63 ± 0.06
63				1,800	5.3	—	4.57	4	1-30	—	3.9 ± 0.5
64				1,800	5.3	222	9.45	4	1-30	0.70 ± 0.15	4.7 ± 0.2
65				1,850	5.5	227	8.46	3	10-100	0.71 ± 0.15	4.6 ± 0.3
66				2,010	6.1	242	32.1 R	3	20-500	0.35 ± 0.10	3.3 ± 0.7
67				2,500	8.0	—	9.45	1	10	—	6.0
68		PAM	Dist. water	900	4.4	194	9.45	5	3-300	1.35 ± 0.25	2.20 ± 0.15
69				1,750	12.0	338	9.45	2	10-40	0.55 ± 0.15	3.8 ± 0.5
70		PAMH	1.00m NaCl	2,300	15.2	315	9.45	2	1-10	0.6 ± 0.2	4.4 ± 0.2
71	Clarke (1971)	PAMH	1.00m NaCl	1,490	7.8	215	10.3	4	10-100	1.1 ± 0.4	3.8 ± 0.4
72			0.02m NaCl	2,600	7.8	269	10.3	4	10-100	0.92 ± 0.24	3.5 ± 0.4
73			1.00m NaCl	1,640	9.2	245	10.3	4	10-100	0.95 ± 0.25	2.7 ± 0.25
74			0.02m NaCl	8,600	9.2	(475)	10.3	2	10-30	0.44 ± 0.14	$2\,5 \pm 0.1$
75	Whitsitt (1968)	PAMH	Water	—	—	—	4.57	2	10-50	—	1.66 ± 0.07
76							10.6	3	10-100	1.2 ± 0.6	1.71 ± 0.14
77							41.1	2	50-100	0.6 ± 0.2	1.34 ± 0.14
78							152	2	100-250	0.4 ± 0.1	1.56 ± 0.04
79		GGM	Water	—	(1.7)	(115)	4.57	3	10-250	4.5 ± 0.6	0.49 ± 0.08
80							10.6	3	50-1,250	4.5 ± 1.5	0.52 ± 0.07
81							41.1	2	250-1,250	4.0 ± 0.6	0.46 ± 0.06
82	Wells (1965)	GGM	Water	—	(1.7)	(115)	16.5	3	500-2,000	4.0 ± 1.0	0.65 ± 0.04
83	Elata (1965-6)	GGM	Water	—	(1.7)	(115)	12.2 R	4	100-800	6.0 ± 1.5	—
84							22.0 R	5	50-800	5.0 ± 1.5	0.50 ± 0.10
85							32.2 R	4	100-800	6.0 ± 1.5	—
86							50.2 R	5	50-800	4.0 ± 1.0	0.55 ± 0.15
87	Giles (1968)	GGM	Water	—	(1.7)	(115)	31.7	2	1,200-2,400	(5.0)	0.55 ± 0.05
88	Wang (1972)	GGM	Water	1,055	(1.7)	(115)	12.7	6	20-1,000	3.0 ± 1.0	0.65 ± 0.05
89		HEC	Water	1,305	1.0	122	25.4	6	50-1,500	2.0 ± 1.0	0.40 ± 0.05

1. In columns 2 to 7 (only), blanks imply repetition of entry immediately above.
2. Numbers in parentheses are uncertain.
3. Entries 11, 31, 32, only, are in Couette flow between concentric cylinders with outer rotating; gap width quoted in column 8.
4. 'R' following pipe I.D. indicates use of recirculating flow system.
5. Column 9, heading Runs, is the number of polymer solution gross flow runs.

T_w^* obtained by the visual method tend to be somewhat lower than those obtained by the slope method, but these differences are usually small compared with the statistical uncertainty inherent in T_w^*.

The effect of pipe diameter on onset was earlier illustrated in Figure 2a. Table 2 contains several additional examples, for example, the sets of entries (6, 7, 8), (23, 24, 25), (51, 52), and (79, 80, 81) which show that T_w^* is essentially independent of pipe diameter.

The effect of polymer concentration on T_w^*, introduced in Figure 2b, merits further discussion based on entries 50, 51, 52, 59, 66, and 73 of Table 2, which represent some of the more precise experimental results. These are displayed in Figure 15, a doubly logarithmic plot of T_w^* versus c. The results of Paterson and Abernathy (1970) and of Hansen and Little (1971) both show T_w^* decreasing with increasing polymer concentration, roughly as indicated by the lines of slope $-1/4$ drawn through each of these data sets (the power-law form is arbitrary). In the former authors' results, the observed variation of T_w^* with c exceeds experimental uncertainties but the latter authors' data, although of high measurement precision, are equivocal because the lowest T_w^*, upon which any presumed concentration dependence hinges, corresponds to $Ref^{1/2*} = 340$ which is very likely in the transitional flow region for their pipe. The results of Clarke (1971) and Virk (1966) show T_w^* independent of polymer concentration, as indicated by the horizontal lines drawn through each of these data sets. Of these, the solid circles are visual onsets, yielding $T_w^* \simeq 8.0$ N/m^2, constant, $20 < c < 1000$: the hollow circles are slope onsets but differ from the usual in that they were derived by fitting data rather remote from onset, $40 < T_w < 160$. Although values of $T_w^* \simeq 14$ N/m^2 are higher in the latter case, reflecting the curvature of the experimental Q versus T_w plot, the insensitivity to polymer concentration over the range $10 < c < 2000$ is again evident; for $0.5 < c < 10$, T_w^* apparently increases somewhat with decreasing concentration but in these cases $\delta \simeq 1$ (see Figure 5a, the central set of hollow circles), consequently $v(T_w^*) \simeq 100\%$ and no trend can be established in this region. In summary, the precise dependence of onset on polymer concentration is not yet known, but available observations show T_w^* only weakly dependent upon c, if at all.

No significant effect of solvent viscosity on onset can be detected from among entries 5 to 17 in Table 2 which contain data for PIB in four classes of solvents, namely, benzene and toluene, cyclohexane, kerosene, and a crude oil, all of which have similar densities, $\rho \simeq 0.85 \pm 0.05$ g/cm^3, but different kinematic viscosities, respectively, 0.0065, 0.0116, 0.016, and 0.062 Stokes.

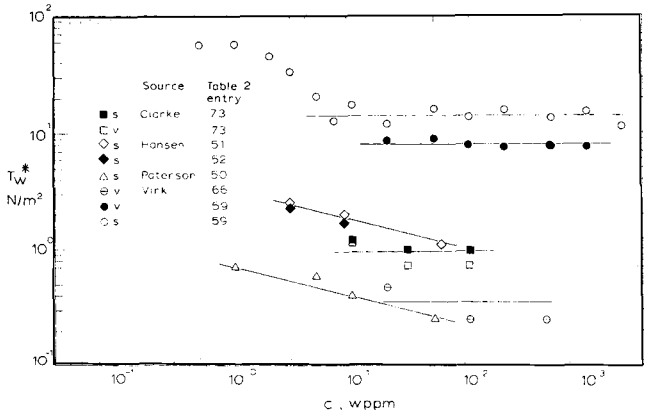

Fig. 15. The effect of polymer concentration on the onset wall shear stress. In legend, v and s besides symbols respectively denote onsets defined by visual and slope methods (see text).

An inverse power-law relation between T_w^* and R_G is suggested by the onset hypothesis, according to which the ratio of characteristic polymer and turbulence scales at onset must be unique, to reflect the incipient polymer-turbulence interaction. Either length or time scales can be matched, leading to the respective onset relations

$$R_G W^* = \Omega_L \tag{19}$$

and

$$R_G^3 T_w^* = \Omega_T \tag{5}$$

where Ω_L and Ω_T are length- and time-based onset constants, characteristic of a given polymer species-solvent pair. The length and time onset relations are both of form

$$T_w^* \propto R_G^{-g} \tag{20}$$

but with different exponents, respectively, $g = 2$ and $g = 3$, which should permit discrimination between them from experimental data. For the three best-characterized polymer-solvent families, namely, PEO-water (35 entries in Table 2), PAM-water, and PAMH-1.0m NaCl (6 entries, combined) and PIB in various solvents (12 entries), least-squares fitting of the available $T_w^* - R_G$ data to the form of (20) yields the best exponents $g = 2.5 \pm 0.2$, 1.6 ± 0.1, and 2.3 ± 0.2, respectively. These provide no clear indication as to whether (19) or (5) is to be preferred on experimental grounds. We will therefore summarize onset results in terms of both length- and time-based onset constants. Table 3 reports average values of Ω_L and of Ω_T for various polymer-solvent families, along with their respective standard deviations and the number of runs (column 4) from which the results were derived. The results for PEO-water are the best established; the PAM-water and PAMH-1.0m NaCl results reflect onsets all at rather too low $Ref^{1/2*}$, while the PIB-cyclohexane onset constants are likely too high, stemming from data in recirculating flow systems, and all other onset results are only preliminary. Although the absolute values of the onset constants must be interpreted with caution, the difference between PEO-water, $\Omega_T = 4.4 \times 10^6$, and the polymethylene group of entries 2, 3, and 4 in Table 3, all $\Omega_T \simeq 13 \times 10^6$, does seem to be statistically significant. Onset constants thus appear to depend on polymer species skeletal structure. No dependence of onset constants upon polymer excluded volume can be detected in the few available data for a given polymer in different solvents.

2.3.3 Slope Moduli. Slope increments are readily derived from experimental data in the range $2 < \delta < 30$; for $\delta < 2$ statistical uncertainties become large while for $\delta > 30$ the data exhibit excessive curvature on P-K coordinates, for example, see the solid circles in Figure 7. The variation of δ with polymer concentration was depicted in Figure 5. For solutions of a given polymer, the relation

$$\delta \propto c^{1/2} \tag{21}$$

appears to be widely applicable. Of the entries in Table 2 which cover concentration ranges of a decade or more, almost all yield δ versus c power-law exponents of 0.5 ± 0.1. As $c \to 0$, (21) appears to hold for as long as δ can meaningfully be detected but as $c \to \infty$, progressing from dilute to concentrated solutions, δ does eventually increase more slowly than $c^{1/2}$ with $c[\eta] \simeq 0.5$ representing an approximate upper limit for application of (21). For a given polymer, the $\delta - c$ relationship is essentially independent of pipe diameter as can be seen by comparing specific slope increments, $\delta/c^{1/2}$, for the sets of entries (6, 7), (51, 52), (63 to 65), (75 to 78), and (79 to 81) in Table 2. Also, for the same polymer, $\delta/c^{1/2}$ seems independent of

TABLE 3. ONSET CONSTANTS AND SLOPE MODULI FOR SOME LINEAR, RANDOM-COILING MACROMOLECULES

Entry	Polymer species	Solvent	Runs	$\Omega_L \times 10^3$	$\Omega_T \times 10^{-6}$	$\kappa \times 10^6$
1	PEO	Water	101	7.1 ± 1.3	4.4 ± 2.1	70 ± 30
2	PAM	Water	7	8.2 ± 0.4	13.1 ± 5.1	95 ± 20
3	PAMH	1.0m NaCl	10	8.2 ± 0.3	13.8 ± 2.8	80 ± 20
4	PIB	Cyclohexane	10	13.2 ± 2.0	13.3 ± 2.3	60 ± 15
5	PDMS	Toluene	8	15.0 ± 2.5	9.0 ± 3.3	70 ± 30
6	PMMA	Toluene	11	—	(13.5)	75
7	PCIP	Toluene	6	—	—	85
8	GGM	Water	29	8.6	6.9	1,300
9	HEC	Water	6	6.1	3.6	1,500

1. Ω_L is dimensionless [Equation (19)].
2. Ω_T is dimensional [Equation (5)], with R_G in nm, T_w^0 in N/m².
3. κ is dimensional [Equation (6)], with $\pi = \delta(M/c)^{1/2}$ and $N = M/m_0$.
4. Error limits represent standard deviations.

the solvent, that is, of polymer excluded volume effects, as seen from the sets of entries (5, 7), (37, 38), (71, 72), and (73, 74) in Table 2; however, this conclusion requires that the polymer still remain random-coiling in its most expanded conformation. Relation (21) is recast to define an intrinsic slope increment

$$\Pi = \delta(M/c)^{1/2} \tag{22}$$

which is physically a slope increment per macromolecule and therefore suitable for further correlation with macromolecular parameters. A plot of intrinsic slope increment versus the number of backbone chain links was earlier shown in Figure 6, the data suggesting

$$\Pi = \kappa N^{3/2} \tag{6}$$

In Figure 6, the solid points are the more reliable, being based on concentration ranges exceeding a decade and reliable polymer characterizations, with N $(= M/m_0)$ obtained by use of Table 1. Slope moduli κ for various polymer-solvent families are listed in column 7 of Table 3, along with their standard deviations. There are evidently two distinct groups; entries 1 to 7 in Table 3, with carbon-carbon types of skeletons, show $\kappa = (70 \pm 30) \times 10^{-6}$ while entries 8 and 9 with cellulosic skeletons possess $\kappa = (1400 \pm 200) \times 10^{-6}$. Polymer sample heterogeneity effects on the results summarized in Table 3 are worth pointing out. Heterogeneity has been accounted for in the onset constants, at least approximately, by the use of R_G obtained via the index H, but no account of heterogeneity has been taken in deriving the slope moduli. Preliminary study of the PEO-water data in Table 2 suggests that $\kappa \propto H^{1/3 \text{ to } 1/2}$ and that the quoted $\kappa = 70 \times 10^{-6}$ in Table 3, entry 1 corresponds to an average $H \simeq 6$; also, extrapolation to $H = 1$ yields a monodisperse $\kappa^0 \simeq 30 \times 10^{-6}$.

2.3.4 Maximum Drag Reduction. Table 4 summarizes some of the available maximum drag reduction data. Entries with asterisks were employed in the original derivation of Equation (4) for the maximum drag reduction asymptote (Virk, Mickley, and Smith, 1970). More recent data are generally in accord with (4), as can be seen in Figure 8, and their inclusion in an overall data fit causes no significant change in either the magnitudes (19.0, −32.4) or uncertainties (±0.4, ±1.2) of the coefficients. Future improvements in the form and precision of the maximum drag reduction asymptote are likely to result from three directions: first, from an extension of the present range of data; second, by more precise rheological characterization of the polymer solutions employed, many of which are concentrated enough to exhibit significant shear thinning; and third, from integration of accurate mean velocity profiles obtained during maximum drag reduction. In applying (4) to shear thinning solutions, a Reynolds number Re_w, formed with the apparent wall viscosity seems preferable to the generalized power-law Reynolds number Re'. For example, in entries 17 and 28 of Table 4, the authors studied the same shear-thinning solution in several pipes of different diameters; in their own works friction factor results were reported in terms of Re' and showed the data from different pipes following widely different trajectories, but when we transform the results to Re_w, using their quoted shear stress versus shear rate relations, the data from all pipes lie rather closer together and adhere to (4), as can be seen in Figure 8.

A power-law expression for the maximum drag reduction asymptote is

$$f = 0.58\, Re^{-0.58}; \quad 4000 < Re < 40{,}000 \tag{4a}$$

It should be noted that (4) exhibits much curvature on the usual friction factor coordinates so that (4a) does not approximate (4) nearly as effectively as the Blasius expression approximates (2).

2.4 Mean Velocity Profile Correlations

Table 5 summarizes the experimental conditions for some of the mean velocity profiles reported during drag reduction. Columns 7 and 8, respectively, quote values of $Ref^{1/2}$ and $f^{-1/2}$ derived from the experimental friction measurements accompanying each mean velocity profile and column 9 lists the corresponding fractional flow enhancement S_F from the definition: $S_F = (-1 + (f_p^{-1/2}/f_n^{-1/2})_{Ref^{1/2}})$. Columns 10 and 11 give values of S^+ and R^+, respectively, which are useful in discussion of law of the wall plots such as Figure 9. The present section will consider the precision of mean velocity data, their correlation in the polymeric and maximum drag reduction regimes, and the inference of the corresponding eddy viscosity profiles.

Mean velocity measurements in polymer solutions present some experimental difficulties because Pitot tubes, long the standard and absolute device for such measurements in Newtonian fluids, behave anomalously (Smith, Merrill, Mickley, and Virk, 1967; Brennen and Gadd, 1967) in polymer solutions. While Pitot tubes of rather large diameter can still be used to yield accurate profiles at conditions of low drag reduction, optical techniques, which do not disturb the flow, are the only good source of information at high drag reductions (see Note 1 under Table 5). Another problem is that, in the time required to measure a profile, the level of drag reduction can change (for example, by degradation of a polymer solution being recirculated), introducing uncertainty into the associated

TABLE 4. SUMMARY OF MAXIM DRAG REDUCTION DATA

Entry	Source	Polymer	Solvent	$M \times 10^{-6}$	c, wppm	Pipe I.D., mm
1*	Toms (1948)	PMMA	Chlorobenzene	3.1	500	1.28
2*	Hoyt (1965)	PEO	W	(6)	30, 100	10.2, 4.60, 1.09
3*	Castro (1966)	PEO	W	(4)	30, 60, 100	11.0, 7.82, 4.70
4*		PEO	W	(7)	5, 20	11.0, 7.82, 4.70
5*	Giles (1967)	PEO	W	(6)	30, 300	2.57, 1.40
6*	Little (1967)	PEO	DW	5.5	100	9.53
7*		PEO	0.3m $MgSO_4$	5.5	100	9.53
8*	Pruitt (1967)	PAMH	W	(3)	100, 1,000	12.7
9	Liaw (1968)	PEO	Benzene	3.1	80, 200	2.72
10		PDMS	Toluene	10.7	30	2.72
11		PDMS	Toluene	5.6	500	2.72
12		PCIP	Toluene	2.2	200, 2,000	2.72, 0.83
13*	Preston (1968)	PEO	DW	0.85	300, 1,000	8.51
14*		PEO	DW	6.1	100	8.51
15	Whitsitt (1968)	GGM	W	(0.2)	1,250	10.6
16		PAMH	W	(3)	250	10.6
17	Seyer (1969)	PAMH	W	(3)	1000	25.4
18	Paterson (1970)	PEO	DW	1.0	50	6.30
19		PEO	DW	8.0	50	6.30
20	Bilgen (1971)	PEO	W	(5)	30, 40, 60, 80, 100	25.3, 6.35, 3.18
21	Clarke (1971)	PAMH	DW	7.8	10, 30, 100	10.3
22		PAMH	0.02m NaCl	9.2	100	10.3
23	Huang (1971)	PEO	W	4.7	50, 100	19.2, 4.55
24		PAMH	W	(15)	50, 80, 100	19.2, 4.55
25	Arunachalam (1972)	PEO	70/30 Ethanol/W	(6)	6, 33	13.6
26	Chung (1972)	PEO	W	(4)	50, 100, 40	11.9
27		PAMH	W	(3)	100, 200, 500	11.9
28	Rollin (1972)	PAMH	W	(3)	1,000	69.8, 25.4
29	Kim (1973)	PAMG	W	(5)	25	6.20
30	Sylvester (1973)	PAMH	DW	2.2	50, 100, 200	6.20
31		PAMH	0.1m $MgSO_4$	2.2	50, 100, 200	6.20
32	Virk (1966-71)	PEO	DW	0.57	3,000	2.92
33*		PEO	DW	0.76	500, 1,000, 2,000	2.92
34		PEO	DW	1.1	1,000	9.45
35		PEO	DW	5.5	30, 100	8.46, 4.57
36*		PEO	DW	6.1	5, 20, 100, 450	32.1, 2.92
37		PEO	DW	8.0	100	8.46
38		PAM	DW	4.4	300, 1,000	9.45
39		PAM	DW	12.0	40, 100	8.46
40*		PAMH	0.1m NaCl	15.0	30, 100	9.45

1. * denotes data employed (Virk, Mickley, and Smith, 1970) in derivation of Equation (4).
2. Polymers: Abbr. as in Table 1, PAMG is a glyoxalated PAM.
3. Solvents: W, DW for water, distilled water; m is molarity of aqueous salt solutions.
4. Molecular weights in parentheses, estimated from trade names or manufacturers' data, are uncertain.

friction velocity which is an important normalization parameter. The precision of presently available mean velocity profiles is typically $\pm 5\%$ in each of U^+ and y^+.

2.4.1 Polymeric Regime. In the polymeric regime, the essential prediction of the elastic sublayer model is that the experimental profiles should show a Newtonian plug region $y_e^+ \leq y^+ \leq R^+$ in which the observed effective slip $S^+ = (U_p^+ - U_n^+)_{y^+}$ equals that computed from friction measurements $S^+ = \sqrt{2}(f_p^{-1/2} - f_n^{-1/2})_{Ref 1/2}$. The latter S^+ are given in Table 5, and these have been used to draw the light lines parallel to the Newtonian wall law (8) in Figure 9; for each polymeric regime profile it can be seen that the experimental data adhere to the predicted Newtonian plug line. (This is, of course, an expected result because the elastic sublayer model was originally inferred from such experimental profiles.) For the foregoing to hold, the Newtonian plug portion of the profile must occupy most of the pipe cross section, say $\xi_e < 0.1$, which is roughly equivalent to $S^+ < 20 \log_{10}(R^+/100)$. The model also postulates that, in the elastic sublayer, $y_v^+ < y^+ < y_e^+$, the mean velocity profile is a segment of the ultimate profile (9), and while the only mean velocity data available close enough to the wall (Rudd, 1969) do indeed closely coincide with the ultimate profile for $15 < y^+ < 60$, rather more evidence is required for any conclusion.

2.4.2 Ultimate Profile. At the time the ultimate profile (9) was originally inferred, by the method noted in Section 1.2.4, no experimental results were available, but data reported subsequently, shown plotted on wall law coordinates in Figure 16, appear to substantiate it. Among the data, the velocity measurements of Rollin and Seyer (1972), by a refinement of the technique used earlier by Seyer and Metzner (1969), are the most accurate; however, these authors used a shear-thinning polymer solution and the y^+ in our plot are based on wall viscosity which may not be appropriate in the pipe core. The results of Rudd (1969) are not at maximum drag reduction but show a near-wall segment which lies on the ultimate profile as noted earlier; the precision of these data cannot be assessed for lack of corresponding solvent data. The data of Chung and Graebel (1972), an early application of laser-Doppler anemometry, have errors of about $\pm 20\%$ in the velocity measurements alone. Arunachalam, Hummel, and Smith (1972) report an error of about $\pm 5\%$ in their velocity measurements but provide no information about uncertain-

Table 5. Summary of Mean Velocity Profile Data During Drag Reduction

Entry	Source	Polymer	$M \times 10^{-6}$	c, wppm	Pipe I.D., mm	Ref½	$f^{-1/2}$	S_F	S^+	R^+
1	Elata (1966)	GGM	1.7	400	50.7	20,500	22.3	0.32	7.8	7,250
2				800	50.7	14,500	28.2	0.74	17.0	5,130
3	Goren (1967)	PEO	5	2.5	50.8	6,200	24.2	0.64	13.3	2,200
4				10	50.8	5,300	28.2	0.94	19.4	1,880
5	Virk (1967)	PEO	0.7	1,000	32.1	2,700	13.5	0	0	940
6				1,000	32.1	8,950	19.9	0.29	6.4	3,170
7	Patterson (1969)	PIB	2.3	2,000	25.4	3,200	17.3	0.27	5.3	1,130
8	Seyer (1969)	PAMH	3	1,000	25.4	780	23.2	1.07	mdr	275
9				1,000	25.4	1,680	29.2	1.34	mdr	590
10	Rollin (1972)	PAMH	3	100	25.4	1,840	18.7	0.47	8.5	650
11				100	25.4	3,450	23.4	0.70	13.6	1,220
12				1,000	25.4	2,950	34.9	1.59	mdr	1,040
13				100	69.8	4,980	19.6	0.36	7.4	1,760
14	Arunachalam (1972)	PEO	5	0.55	13.6	2,290	16.4	0.25	4.7	810
15				5.5	13.6	1,440	25.7	1.10	mdr	510
16				33	13.6	1,780	27.6	1.18	mdr	630
17	Chung (1972)	PAMH	3	100	11.9	1,300	27.9	1.31	mdr	460
18				200	11.2	350	15.2	0.56	mdr	125
19	Rudd (1969)	PAMH	3	100	12.7 sq.	1,700	29.5	1.0	20	600

1. Methods used to measure mean velocities as follows:
   Entries 1 to 6—pitot tubes
   Entry 7—hot film anemometry
   Entries 8 to 13—bubble streak photography
   Entries 14 to 16—photochromic dye photography
   Entries 17 to 19—laser-Doppler anemometry
2. All polymer molecular weights are approximate only.
3. In column 10, mdr means the entry is at, or close to, maximum drag reduction.

ties in y^+ although they used a once-through flow system and a rather dilute polymer solution so that there should be little error in either u_T or ν. From the foregoing, the approximate agreement between the available data and the ultimate profile can be regarded as favorable, but less than conclusive, evidence for the existence and correctness of the latter.

The ultimate profile permits prediction of the ratio of center line to bulk average velocities at maximum drag reduction which provides an index of velocity profile shape. At $R^+ = (100, 200, 500, 1000, 2000)$, respectively, Equations (9) and (14c) yield $(U_1/U_{av})_m = (1.87, 1.62, 1.45, 1.37, 1.32)$ while, to the same approximation, (8) and (14a) give $(U_1/U_{av})_n = (1.28, 1.25, 1.22, 1.20, 1.18)$. Further, at a given R^+ at low drag reduction, it is evident that $(U_1/U_{av})_p = (U_{1,n}{}^+ + S^+)/(U_{av,n}{}^+ + S^+) < (U_1/U_{av})_n$. Thus, the elastic sublayer model predicts that, with increasing drag reduction at a given R^+, the mean velocity profile should initially tend to be blunter than Newtonian, but eventually become sharper than Newtonian as maximum drag reduction is approached. Qualitative confirmation of this predicted sequence of velocity profile shape changes is available in the results of Rollin and Seyer (1972), and, quite strikingly, in the photographs of Arunachalam, Hummel, and Smith (1972). It is also interesting that, at $R^+ = 100$, $(U_1/U_{av})_m$ is much closer to 2.0 than is $(U_1/U_{av})_n$, which suggests that the ultimate profile can evolve from a parabolic laminar profile without the large discontinuities that arise in the Newtonian case; this is of possible relevance in the detection of intermittency during transition.

2.4.3 Eddy Viscosity Profile. Eddy viscosity profiles during drag reduction, all derived from gross flow and mean velocity measurements, are shown in Figure 17, using doubly logarithmic coordinates of ϵ/ν versus y^+. The Newtonian case $S_F = 0$ is represented by the results of Laufer (1954) which can be approximated by the usual three segments, (i) a near-wall region, (ii) a law of the wall region, and (iii) a core region, given by

$$\epsilon/\nu = \gamma y^{+3} \tag{23a}$$

$$= Xy^+ \tag{23b}$$

$$= \zeta R^+ \tag{23c}$$

Equations (23a) and (23b), with Newtonian coefficients $(\gamma_n, X_n) = (0.00087, 0.4)$ are indicated by heavy solid lines, of slopes 3 and 1, respectively, in Figure 17. In the polymer solutions, for region (i), we have information only at maximum drag reduction. Under these conditions, mass transfer measurements (Virk and Suraiya, 1975) at $Sc = 10^3$, which stress the regions where $\epsilon/\nu < 10^{-3}$, suggest $(\gamma_m/\gamma_n)^{-1/3} = 1.9 \pm 0.1$, while experiments on

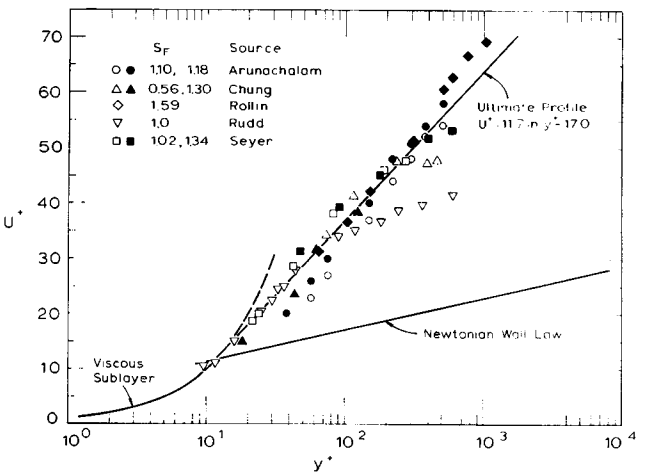

Fig. 16. Evidence for the ultimate mean velocity profile. See Table 5 for experimental details.

the onset of roughness (Virk, 1971), which stress the region where $\epsilon/\nu = 10^{-1}$, yield $(\gamma_m/\gamma_n)^{-1/3} = 2.5 \pm 0.2$. The average $(\gamma_m/\gamma_n)^{-1/3} = 2.2$ may be used to represent the near-wall region at maximum drag reduction, and (23a) with γ_m so calculated is shown by the dashed line of slope 3 in Figure 17. For region (ii), all of the ϵ/ν are from differentiation of mean velocity profiles already displayed in Figure 9 and merit no further discussion save to point out the approximate bounding relations, (23b) with X_n and X_m respectively, the latter shown as a dashed line of slope 1 in Figure 17. In region (iii), the ϵ/ν profiles tend to constant values in all cases as shown by the light horizontal lines in Figure 17 besides which are noted the corresponding $\zeta = \epsilon/Ru_T$, the latter nondimensional grouping being appropriate for the core (Hinze, 1959). At less than maximum drag reduction, the polymer solution data all yield $\zeta_p \simeq \zeta_n = 0.06$, reinforcing the Newtonian plug notion, but at maximum drag reduction, Rollin's data yield $\zeta_m \simeq 0.013$. The latter is especially curious because it implies $(\zeta_m/\zeta_n) = (X_m/X_n)$, that is, that at maximum drag reduction, the entire outer flow structure, say $y^+ > 50$, is analogous to Newtonian save for a different similarity parameter, X_m instead of X_n.

The preceding suggest an eddy viscosity profile during drag reduction bounded between the Newtonian profile and a maximum drag reduction profile, the latter such that, at a given y^+, $(\epsilon/\nu)_m \simeq 0.1\,(\epsilon/\nu)_n$ in the near-wall region, $y^+ < 10$, and $(\epsilon/\nu)_m \simeq 0.2(\epsilon/\nu)_n$ in the outer flow, $y^+ > 50$. At low drag reduction, an essentially Newtonian eddy viscosity profile prevails which is, by inference from Figure 12a, dimpled downward in the neighborhood of $\epsilon/\nu \simeq 1$; with increasing drag reduction, the dimple deepens, spreads outward to the pipe core (also, presumably, toward the wall) and bottoms out on the maximum drag reduction profile, the sequence of these events yet unknown.

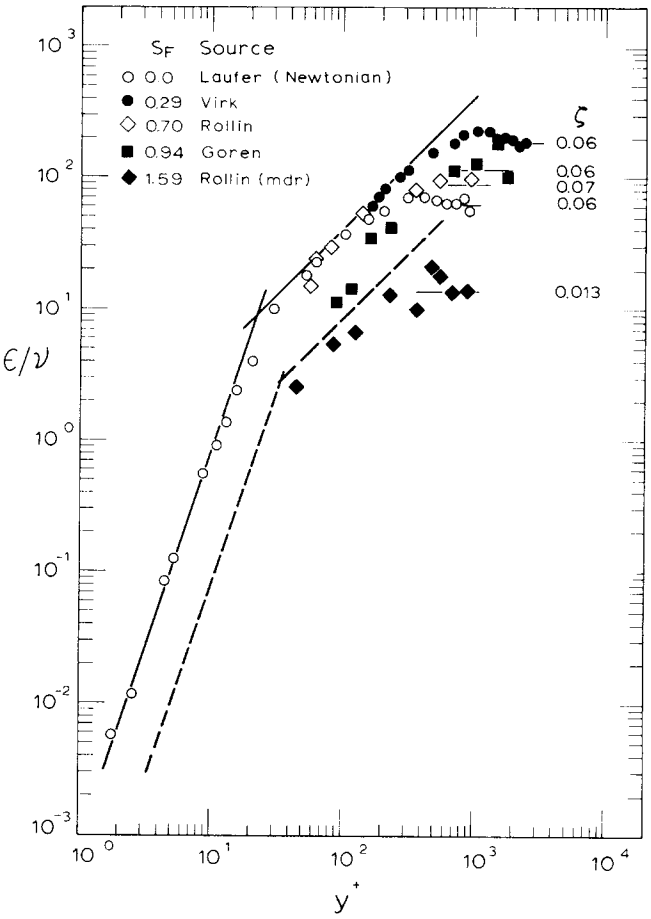

Fig. 17. Eddy viscosity profiles during drag reduction. The heavy solid and dashed lines respectively refer to Newtonian and maximum drag reduction (mdr) conditions.

2.5 Turbulence Structure Correlations

Table 6 summarizes turbulence structure measurements during drag reduction. The contents of columns 1 to 11 in Table 6 are identical with those of columns 1 to 11 in Table 5, described earlier. Where a square pipe or rectangular channel was used, $Ref^{1/2}$ is omitted and R^+, based on half-width, quoted. Columns 12 to 15 in Table 6 refer to turbulence quantities normalized by inner scales, u_T and ν, values of the former being quoted in column 16. Column 12 gives the center line mean square turbulent kinetic energy, column 13 the axial turbulent intensity gradient at the wall, column 14 the azimuthal streak spacing, and column 15 the mean time between turbulent bursts. For each source in Table 6, the first entry contains representative results obtained with (Newtonian) solvent alone which are required because the turbulence measurements are all subject to such large uncertainties that only comparisons between polymer solution and solvent results have significance. Turbulence structure results presented in Section 1.5 were all obtained by laser-Doppler anemometry, and in this section some further results obtained from a flow visualization study and by electrochemical techniques will be discussed. Hot-wire (film) anemometer derived data are omitted entirely because of the anomalous, and yet largely undefined, nature of crossflow heat transfer from small cylinders to polymer solutions (Smith et al., 1967; Friehe and Schwarz, 1969; James and Acosta, 1970).

The evidence summarized in Section 1.3.3 suggested that the elastic sublayer notion might well be applicable to the turbulence structure during drag reduction. If so, then turbulence quantities should be scaled by the usual parameters, that is, elastic sublayer thickness (or S^+) in the polymeric regime and X_m at maximum drag reduction.

The entries in Table 6 are all from the polymeric regime, so we seek relationships between turbulence quantities and S^+. Preliminary results of this quest are shown in Figure 18, a three-part plot of (a) maximum kinetic energy, (b) axial intensity gradient, and (c) azimuthal streak spacing versus S^+; in all three parts, the ordinates are doubly normalized, first by wall scales and second by the corresponding nondimensional solvent value.

In Figure 18a, maximum turbulent kinetic energies were obtained from measured maximum axial intensities using $q = (u'^2 + v'^2 + w'^2) \simeq u'^2$, the latter a good approximation in the region of maximum q^+ because the axial contribution is about 80% of the total. The two data points in Figure 18a lie on a straight line through (0, 1) and with slope 0.1:

$$(q_{\max,p}{}^+/q_{\max,n}{}^+) = 1 + 0.1\,S^+ \qquad (24)$$

If we assume a typical $q_{\max,n}{}^+ = 10$ (after Laufer, 1954), then (24) implies $(q_{\max,p}{}^+ - q_{\max,n}{}^+) \simeq S^+ = U_{\max,p}{}^+ - U_{\max,n}{}^+$, that is, during low drag reduction, the (nondimensional) maximum kinetic energy and mean velocity exceed their respective Newtonian values by roughly the same amounts. This is possibly a consequence of the closely analogous nature of the turbulent transport of kinetic energy and of momentum (Virk, 1975). In both cases, the transport is due to velocity correlations of the forms $\langle vq \rangle$ and $\langle vu \rangle$, respectively, and near the wall $\langle vq \rangle \simeq \langle vu^2 \rangle$ so that both depend on a similar sort of coupling between the radial and axial flow fields. Recalling Figure 12b, the latter coupling seems to be altered in the elastic sublayer region.

In Figure 18b, the axial intensity gradients at the wall were obtained either from measured axial intensity profiles

Table 6. Summary of Turbulence Structure Data During Drag Reduction

Entry	Source	Polymer	M $\times 10^{-6}$	c, wppm	Pipe I.D., mm	$Ref^{1/2}$	$f^{-1/2}$	S_F	S^+	R^+	$q_1{}^+$	α^+	Z^+	$\theta^+{}_{bb}$	u_T, m/s
1	Logan (1972)	none		0	12.7 sq.		11.8	0	0	815	3.6	0.18			0.128
2		PEO	5	50			15.6	0.4	6	536	3.6	0.17			0.093
3	Rudd (1969)	none		0	12.7 sq.		13.7	0	0	360		0.45			0.051
4		none		0			—	0	0	700	4.3	—			0.10
5		PAMH	3	100			29.5	1.0	20	600	3.6	0.45			0.10
6	Fortuna (1972)	none		0	25	2,140	12.9	0	0			0.34	100		0.057
7		PAMH	3	150		1,825	15.1	0.19	3.5			—	160		
8				150		1,725	16.0	0.27	4.9			0.30	—		
9				150		2,070	18.9	0.43	8.0			—	320		
10				150		2,450	23.6	0.79	14.7			0.25	500		
11	Donohue (1972)	none		0	40.4 ch.		17.9	0	0	165			100 ± 6	135 ± 40	0.0073
12		PEO	8	140			19.6	0.18	3.0	108			124	100 ± 10	0.0067
13				140			22.1	0.26	4.6	153			128	123	0.0095
14				140			22.5	0.29	5.1	149			174	83	0.0092
15				140			28.1	0.49	9.3	251			185	—	0.0156
16	Taylor (1974)	none		0	50.8	2,670	13.1	0	0		2.0				0.033
17		PEO	4	50		2,140	16.3	0.26	4.8		2.0				0.027

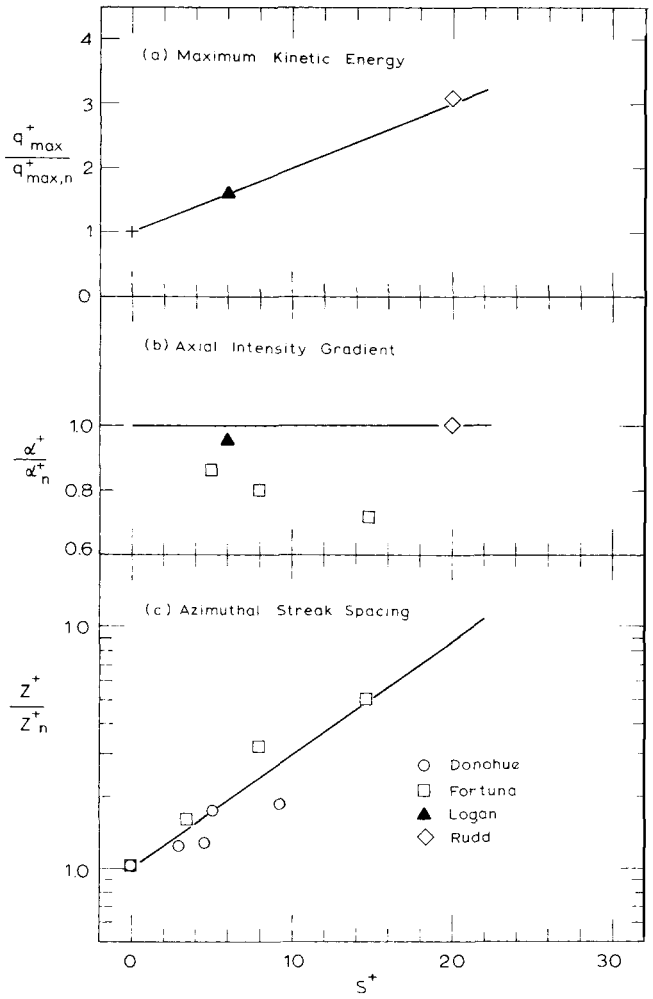

Fig. 18. The variation of some wall-turbulence quantities with drag reduction: (a) Maximum kinetic energy; (b) Axial turbulent intensity gradient at the wall; (c) Azimuthal streak spacing. See Table 6 for experimental details.

(Rudd, 1969; Logan, 1972), as shown in Figure 11a, or from electrochemical measurements (Fortuna and Hanratty, 1972). Plotted against S^+, these data are equivocal: the former measurements suggest $(\alpha_p{}^+/\alpha_n{}^+) = 1, 6 < S^+ < 20$, while the latter show $(\alpha_p{}^+/\alpha_n{}^+) = 0.8 \pm 0.1$, $5 < S^+ < 15$, but it is apparent that no profound changes in α^+ occur during low drag reduction. Therefore, we surmise that

$$(\alpha_p{}^+/\alpha_n{}^+) = 1 \qquad (25)$$

as indicated by the horizontal line in Figure 18b. Physically, α^+ is derived from the region of the viscous sublayer, $y^+ < 10$, a characteristic feature of which is an intermittent streaky structure (Kline et al., 1967). α^+ itself is directly the viscous sublayer turbulent intensity expressed as a fraction of mean velocity, $\text{Lim}_{y^+ \to 0} <uu>^{1/2}/U$ ($\simeq 0.3$); also, α^+ is related to the intermittency in the viscous sublayer through the streak velocity deficiency relative to the mean flow. The data embodied in (25) suggest then that some features of the Newtonian streaky structure persist unchanged at low drag reduction.

In Figure 18c, the azimuthal streak spacings shown were derived from analysis of electrochemical measurements (Fortuna and Hanratty, 1972; Eckelman, Fortuna, and Hanratty, 1972) and from flow visualization experiments (Donohue, Tiederman, and Reischman, 1972). There is a distinct tendency for Z^+ to increase with increasing S^+, with semilogarithmic slope $d\ln Z^+/dS^+ = 0.10 \pm 0.02$. The solid line in Figure 18c, from fitting the data, is

$$\ln(Z_p{}^+/Z_n{}^+) = 0.11\, S^+ \qquad (26)$$

Comparison of (26) with the elastic sublayer relation (13), $\ln(y_e{}^+/y_v{}^+) = 0.11\, S^+$, leads to the interesting conclusion that the azimuthal streak spacing increases roughly in proportion to elastic sublayer thickness, that is, the Newtonian aspect ratio of azimuthal to radial macroscales is preserved in the inner flow. It should be noted that the results of Figures 18b and 18c are not independent, but the measurements required to test their mutual consistency are unavailable.

Concerning the phenomenon of turbulent bursts, Donohue, Tiederman, and Reischman (1972) seemed unable to detect any significant differences between Newtonian flows and those with low drag reduction. Their results for the mean time between bursts, given in column 15 of Table 6, show $\theta_{bb,p}{}^+ = 100 \pm 30$ essentially indistinguishable from $\theta_{bb,n}{}^+ = 135 \pm 40$. It is not certain whether θ_{bb} is best normalized by inner (Kline et al., 1967) or outer (Rao, Narasimha, and Badri Narayanan, 1971) flow scales; use of the latter yields $(U_{av}\theta_{bb}/R)_p = 17 \pm 3$, again indistinguishable from $(U_{av}\theta_{bb}/R)_n = 16 \pm 8$.

2.6 Sources

We attempt to refer the reader to some of the original sources of the preceding developments.

In regard to gross flow, the works of Toms (1948) and Oldroyd (1948) are required reading; the former's data touch on all presently known gross flow features while the latter's connection of drag reduction with an effective slip (inferred, incidentally, from a P-K plot) anticipated experimental results by 17 years. Some of the earliest investigations of onset were by Elata and Tirosh (1965), Hershey and Zakin (1967), and Virk et al. (1966, 1967). The latter works pointed out the existence of an abrupt onset of drag reduction and identified $T_w{}^*$ and R_G as relevant flow and polymer parameters in an onset hypothesis based on length scales. Time-based onset hypotheses were first proposed by Hershey and Zakin (1967), Fabula, Lumley, and Taylor (1966), and Elata, Lehrer, and Kahanovitz (1966). In the polymeric regime, the P-K slope increment was identified as an important entity by Meyer (1966), his fluid property parameter α differing from our δ only by a numerical factor. The dependencies of δ upon polymeric parameters, as $c^{1/2}$ (Virk and Baher, 1970) and $N^{3/2}$ (Virk, 1971), were suggested by the present author. The maximum drag reduction asymptote, its universality, and Prandtl-Karman form were first pointed out by us (Virk et al., 1967, 1970) although the existence of a maximum possible drag reduction was independently noted by several investigators (Hoyt and Fabula, 1964; Castro and Squire, 1967; Giles, 1968). The reader should also be aware of some alternative gross flow correlation schemes, for example, those of Rodriguez, Zakin, and Patterson (1967), Whitsitt, Crawford, and Harrington (1968), Seyer and Metzner (1969), Astarita, Greco, and Nicodemo (1969).

Some of the earliest mean velocity profiles, exhibiting the effective slip, were reported by Ernst (1966), Elata, Lehrer, and Kahanovitz (1966), Goren and Norbury (1967), and Virk et al. (1967); the first profiles at maximum drag reduction were measured by Seyer and Metzner (1969) and by Rollin and Seyer (1972). Mean flow models evolved from the thickened laminar sublayer scheme (Meyer, 1966; Elata, Lehrer, and Kahanovitz, 1966), that is, two zones, a viscous sublayer and a Newtonian plug, with the latter moving upward to show an effective slip as the former thickened with increasing drag reduction. The model is appropriate at low drag reduction but erroneously

tends toward Poiseuille's law as drag reduction increases. Seyer and Metzner (1969) eliminated the latter error by forcing the viscous sublayer thickening to be asymptotic, with maximum allowed Newtonian plug effective slip of $S^+ \simeq 25$, but this then predicts a maximum drag reduction asymptote with Prandtl-Karman slope, 4.0 (and a parallel upshift of $(25/\sqrt{2})$ in $f^{-1/2}$ relative to (2)), whereas the experimentally observed asymptote (4) has a much different slope, 19.0. Finally, our three-zone elastic sublayer model (Virk, Mickley, and Smith, 1970; Virk, 1971) properly reproduces presently known gross flow and mean velocity profile features. Another three-zone mean flow model is due to Van Driest (1967, 1970); in this, the central zone mixing length constant is assumed to be a function of macromolecular parameters and therefore fails to yield the observed asymptotic behavior, which is independent of macromolecular parameters.

The turbulence structure measurements summarized in Table 6 are all among the first of their kind during drag reduction, namely axial intensity (Rudd, 1969), radial intensity and turbulent shear stress (Logan, 1972), azimuthal streak spacing (Fortuna and Hanratty, 1972) and times between bursts (Donohue, Tiederman, and Reischman, 1972).

3. MECHANISM

A mechanism for drag reduction must specify the basic polymer-turbulence interaction responsible for the phenomenon and detail how this interaction affects the energy balances in turbulent pipe flow to yield the observed reduction in specific energy requirement relative to the solvent alone. In this section, the attempt is first to outline a physical framework for discussion of the mechanism problem and to refer the reader to some of the approaches taken in the literature. Next, we try to synthesize a (fragmentary) picture of the polymer-turbulence interaction and of the energy balances by inference from experimental information. It should be noted at the outset that the mechanism of drag reduction is still rather obscure and our discussion involves speculation and is likely to contain some erroneous impressions.

3.1 Physical Framework

We try to outline some elements of a drag reduction mechanism. The region initially affected by the addition of macromolecules appears to be $y^+ \simeq 15$, and the characteristic features of the flow in this region involve turbulent bursts (Kline et al., 1967). To assess the interaction between a macromolecule and a burst, we seek a simple flow field to model the fluid particle deformation during a burst. The sequence of burst events is quite well known (Kline et al., 1967; Corino and Brodkey, 1969; Kim, Kline, and Reynolds, 1971; Nychas, Hershey, and Brodkey, 1973; Offen and Kline, 1974), but a clear kinematic signature relevant to drag reduction has yet to be identified. However, elongational flows seem to merit the most attention for two reasons: first, because dilute polymer solutions can exhibit striking anomalies at stagnation points (Smith et al., 1967), the approach to which involves this type of irrotational, straining motion, and second, because fluid particle elongations of significant magnitude are indeed apparent in the near-wall flow visualizations of Grass (1971) and of Kim, Kline, and Reynolds (1971). The next step is to describe dilute polymer solutions by an appropriate rheological equation of state, developments pertinent to drag reduction being considered in several recent works (Metzner and Metzner, 1970; Batchelor, 1971; Lodge and Wu, 1971; Bird, Warner, and Evans, 1971; Hinch and Leal, 1973; Oliver and Bragg, 1974; Hinch, 1974; Williams, 1975). Finally, the rheological equation is applied to a model of the wall turbulence, and the predicted changes, relative to Newtonian, are interpreted in terms of experimental drag reduction observations.

Of drag reduction models which have been proposed in the literature, Walsh (1967) gave substance to a long-standing, but vague, association of drag reduction with visco-elasticity (Metzner and Park, 1964; Wells, 1965; Gadd, 1966) by linking it to the turbulent transport of macromolecular strain energy. While the relevance of its transport remains unproven, the strain energy, resulting from macromolecular deformation, does seem implicated in drag reduction. Black (1968) provided the first clear connection between drag reduction and the bursting phenomenon in wall turbulence, assuming that the polymer molecules reduced the burst frequency. Experiments at low drag reduction do not appear to support Black's basic assumption, but his model nevertheless has many qualitatively correct features and, most notably, predicted an increase in $u_{max}'^+$ relative to Newtonian which anticipated experimental measurements. Landahl (1973) and Landahl and Bark (1974) have applied their two-scale model of a turbulent boundary layer to drag reduction. They consider the flow to consist of large- and small-scale fields, coupled through the turbulent bursting process, with bursts viewed as a kind of recurring instability. The elongation of added polymer molecules is postulated to stabilize the small-scale flow field, presumably because at very small scales, that is, high strain rates, macromolecular extension profoundly increases the (elongational) viscosity. Landahl's model incorporates an attractive rheological argument, but its detailed consequences, especially the implied burst stabilization, remain to be tested. Lumley (1969, 1973) has postulated a most comprehensive and physically plausible drag reduction mechanism in which macromolecular elongation initiates a sequence of changes in mean and turbulent flow structures, which are predicted in some detail and "suggest many investigations," the outcome of which is awaited. Hansen (1973), a noteworthy example of the continuum approach, has examined the behavior of a fluid with a simple rheological equation, Maxwell's model, in a transient laminar shear flow, which is relevant to wall turbulence, and obtained results which qualitatively agree with some gross flow drag reduction observations. Substantive mechanistic ideas are also contained in some of the following references: Gadd (1971), Boggs (1969), Peterlin (1970), Rudd (1971), and Gordon and Balakrishnan (1972).

3.2 Polymer-Turbulence Interaction

Oldroyd's (1948) suggestion that the polymer molecules most affected by the near-wall region is supported and clarified by many subsequent experiments. Wells and Spangler (1967) injected a polymer solution into a turbulent water flow at both the wall and the axis of a pipe; in the former case, the wall shear stress was reduced almost directly downstream of the injection point, whereas in the latter case the drag reduction was observed relatively much further downstream, presumably only after the macromolecules had diffused to the wall region. Mean velocity profiles, shown in Figure 9, indicate that, at low drag reduction, the region affected is closer to the wall than $y^+ \simeq 50$, whereas rough pipe experiments (McNally, 1968; Spangler, 1969; Virk, 1971) show that onset is unaffected by the presence (hydraulically smooth flow) or absence (fully rough flow) of a viscous sublayer, which suggests that the region of interest is further from the wall than $y^+ \simeq 5$; together, these implicate $5 < y^+ < 50$ as the region affected by the macromolecules. Turbulence measurements (Figure 11a) also suggest that the region affected is

roughly $10 < y^+ < 100$. From the foregoing, it is very likely that the polymer-turbulence interaction responsible for drag reduction commences in the buffer zone near the plane of peak turbulent energy production, $y^+ \simeq 15$.

Flow visualization studies (Kim, Kline, and Reynolds, 1971) indicate that turbulent energy production occurs mainly during relatively discrete bursts in which low speed streaks lift up from the viscous sublayer, exhibit an oscillatory growth of instability, and then break down via streamwise and transverse vortices, being ejected into the core during the latter processes. It is clearly of interest to compare macromolecular and burst scales. Bursts have two characteristic times, the mean time between bursts θ_{bb} which is the inverse of the average frequency of bursting, and the actual duration of a burst θ_b with $\theta_b < \theta_{bb}$. It is yet unclear whether burst times correlate with inner or outer flow scales. For turbulent boundary layers, the correlation of Rao et al. (1971) indicates $(\theta_{bb}U_e/\Delta_*) = 32 \pm 5$, independent of Reynolds number; in pipe flow, from $(U_{av}/U_1) \simeq 0.8$ and $(\Delta_*/R) \simeq 1/8$ (Schlichting, 1960), we should then expect $(\theta_{bb}U_{av}/R) = 3.2 \pm 0.5$. However, the available data (Corino and Brodkey, 1969; Donohue, Tiederman, and Reischman, 1972; Bremhorst and Walker, 1973) show $25 > (\theta_{bb}U_{av}/R > 3$ for $6 \times 10^3 < Re < 6 \times 10^4$ and, among much scatter, $(\theta_{bb}U_{av}/R) \propto Re^{-1}$. This suggests that inner scaling might be the more appropriate, and the same data yield $\theta_{bb}{}^+ = 180 \pm 100$ with no discernable trends versus Re. In regard to burst duration, which is the time more relevant to drag reduction, the spectral measurements of Bremhorst and Walker (1973) suggest $\omega_b{}^+ = 0.4 \pm 0.2$ $(\theta_b{}^+ = 2\pi/\omega_b{}^+)$. The macro molecular time scale can be estimated from the theory of Zimm (1956) which predicts a terminal relaxation time $\tau_m = 0.42\, M[\eta]\, \eta_s/\mathbf{NkT}$. As an example relevant to drag reduction, the experimental relaxation time measurements of Sakanishi (1968) on a PIB, $M \simeq 2 \times 10^6$, in benzene and in cyclohexane are in striking agreement with Zimm's theory. The empirical time onset constants of Table 3, Zimm's theory, and $\omega_b{}^+$ allow an estimate of the (universal) ratio of relaxation time to burst duration at onset:

$$(\omega_b\tau_t)^* = \omega_b{}^+\Omega_T(0.42 \times 6^{3/2}\Phi \times 10^{-27}/\mathbf{NkT}) \simeq 2 \tag{27}$$

(Incidentally, the dimensionless group on the left-hand side of (27) is sometimes called a Deborah number, a generic name for the ratio of characteristic fluid to flow times, or their reciprocal.) In regard to length scales, the viscous sublayer streaks which eventually burst have a width of $\Lambda_b{}^+ = 20 \pm 10$; this should be relevant at the start of the bursting process, but striking changes in length scale (Kim, Kline, and Reynolds, 1971) occur thereafter. From another angle, an axial kinetic energy spectrum at $y^+ = 13$ (Bremhorst and Walker, 1973) shows a maximum at $k^+ \simeq 0.02$, the reciprocal of which, that is, the energy-containing eddy wavelength, is about streak width. The same energy spectrum suggests a maximum for the dissipation function $k^2E(k)$ at $k^+ \simeq 0.2$ from which the smallest burst length scale can be taken as $\lambda_b{}^+ = 5$. We have then the (maximum) ratio of random-coiled macromolecule to burst length scales at onset:

$$(k_bR_G)^* = \Omega_L/\lambda_b{}^+ \simeq 0.002 \tag{28}$$

At the onset of drag reduction, (27) and (28) indicate that the strain rate during a turbulent burst is high enough to excite the macromolecule while the random-coiling macromolecule is small enough that over its domain the bursting flow field is essentially uniform. Among polymers used, $20 < (L_C/R_G) < 330$, at the upper end of which range the macromolecule contour length would be of the order of the burst microscale at the onset, although, we hastily add, there is no evidence whatever for the attainment of a fully-uncoiled state, experiments on macromolecular elongation yielding maximum principal axis extension ratios $\simeq 4$, two orders of magnitude lower than full extension (Cottrell, Merrill, and Smith, 1969; Smith, Merrill, and Banijamali, 1974).

The precise role of elongational flows, either during turbulent bursts or in deforming macromolecules, is yet unknown. Peterlin (1966) has shown theoretically that, at high strain rates, the increase in macromolecular principal extension ratio with strain rate is faster in elongational than in shear flows. This leads (Lumley, 1971, 1973; Landahl, 1973) to the theoretical possibility of enormous increases in elongational viscosity, but not in shear viscosity, for dilute polymer solutions in a flow field where the ratio of vorticity to strain rate is small. The main experimental basis for associating elongational flows with drag reduction resides in the anomalous behavior exhibited by stagnation flow devices in dilute polymer solutions as we now try to illustrate (Virk and Merrill, 1969). Consider the flow of a 100 wppm solution of a PEO, $M \simeq 5 \times 10^6$, in four cases: (i) past a Pitot tube of squared-off cylindrical tip, O.D. 0.51 mm, (ii) transverse to a cylindrical hot-film probe, O.D. 0.025 mm, (iii) inside a pipe of I.D. 32.1 mm, with turbulent flow, and (iv) inside a capillary tube of I.D. 0.24 mm, with laminar flow. In the first two cases, the onset of anomalous behavior, namely (i) decreased stagnation pressure and (ii) lower heat transfer coefficient, relative to Newtonian, occurred at a stagnation strain rate of order 10^3 s^{-1}. Approaching a stagnation point, the flow is irrotational and the rate-of-strain tensor has its principal axes of extension perpendicular to the stagnation streamline, the stagnation strain rate being of order (U_e/R) where U_e is the approach velocity and R the obstruction half-width, normal to the flow. In case (iii), the onset of turbulent drag reduction occurred at a wall shear rate of about 10^3 s^{-1}, but in case (iv), at wall shear rates up to 10^5 s^{-1}, no anomalous behavior was observed: in a developed laminar pipe flow, of course, there is vorticity, of the order of the strain rate. Comparison of cases (i) and (ii) with (iv) suggests the importance of elongational flows in causing anomalous behavior of dilute polymer solutions, and then the further comparison between (i) and (ii), and (iii) suggests that elongational flow may be relevant to drag reduction.

It seems possible that the elastic sublayer observed during drag reduction physically represents the region where macromolecular deformation alters the normal Newtonian energetic processes (Virk, 1971). Pursuing this premise, we devise a theoretical expression for turbulent strain energy and try to relate it to the experimental results. The strain energy per unit of a dilute polymer solution is the molecular concentration $(10^{-6}\ \mathbf{N}c/M)$ times the strain energy per molecule, the latter being (Treolar, 1958)

$$\mathbf{s}_{\mathrm{mol}} = (\mathbf{kT}/2)(-1 + L''^2/L^2) \tag{29}$$

Theories of macromolecular extension in laminar flows (Peterlin, 1963, 1966; Cerf, 1968) show that, at small extensions, in both shear and elongation,

$$(-1 + L''^2/L^2) = J\beta^2 \tag{30}$$

with β a nondimensional strain rate and J predicted to be about 10^{-1}. Experiments in a Couette flow (Cottrell, Merrill, and Smith, 1969) yield J about 10^{-3} to 10^{-2} while those in a Borda flow (Smith, Merrill, and Banijamali, 1974) show J may be about 10^{-1}. The disagreement between the theoretical and Couette flow results (and, presumably, also between the Couette and Borda flow

results) can be attributed (Cerf, 1968; Cottrell, Merrill, and Smith, 1969) to an internal viscosity, that is, to torsional energy barriers that hinder interconversions between conformational isomers, thus making the real polymer chain less than perfectly flexible. Taking J to be an empirical chain deformation factor, dependent on polymer skeletal structure, the mean strain energy in a one-dimensional flow is

$$S = JkT(Nc/M)(M[\eta]\,\eta_s/NkT)^2G^2 \qquad (31)$$

Now, the response of a macromolecule to an external stimulus requires the coordinated movement of various sets of its individual segments, termed *modes*, and in a turbulent flow the macromolecule will necessarily suffer stimulation by the entire spectrum of turbulence. Therefore, the turbulent strain energy s′ can be thought of as being distributed over all modes of the macromolecule at all wave numbers of the turbulent flow field. A typical spectral element of s′ will thus contain the strain energy associated with, say, the jth mode of the macromolecule at the kth wave number. The form on an s′ element is obtained by analogy with (31) in which the $(M[\eta]\,\eta_s/NkT)$ term has dimensions of time and can hence be replaced by an element τ_j, representing the contribution of the jth mode to the macromolecular relaxation time while G^2 is replaced by an element $k^2E(k)dk$ of the mean-square turbulent strain rate at wave number k. The local turbulent strain energy is, finally,

$$s' = [JkT(Nc/M)(M[\eta]\,\eta_s/NkT)^2]\left[\int_0^\infty \sum_{j=1}^{n} \mu_j(j,k)k^2E(k)dk\right] \qquad (32)$$

Of the two square brackets on the right-hand side of (32), the first, of dimensions [length]^2, consists entirely of molecular parameters associated with a given polymer solution, whereas the second, dimensions [time]$^{-2}$, involves only the excitation of an individual macromolecule by the turbulent flow field at the given radial location. This separation of variables is reminiscent of that employed in Equation (15b) of Section 2.1. If the turbulent strain energy is normalized by wall turbulence scales, $\Phi(Nb^2)^{3/2}$ substituted for the $M[\eta]$ product in (32), and the normalized excitation integral (at a characteristic radial location) called I^+, then

$$s'^+ = [(Nc/M)^{1/2}N^{3/2}(J/kT)^{1/2}b^3(\Phi/N)(u_T/\nu_s)]^2 I^+ \qquad (33)$$

Experimental results for the slope increment in the polymeric regime, (6) and (22) substituted into (15b), show that the observed effective slip is given by

$$S^+ = [(Nc/M)^{1/2}N^{3/2}(\kappa/1.626N^{1/2})]\ln(u_T/u_T^*) \qquad (34)$$

The experimental concentration and backbone chain link dependencies are *both* matched by assuming the effective slip related to the square root of turbulent strain energy:

$$S^+ \propto s'^{+1/2} \qquad (35)$$

Equation (35) is our tentative physical connection between the theoretically developed expressions for turbulent strain energy and the experimentally observed dependence of drag reduction on polymeric parameters. Notice that (33), (34), and (35) imply a further pair of relations:

$$\kappa \propto (J/kT)^{1/2}b^3 \qquad (36)$$

and

$$I^{+1/2} \propto (u_T^*/u_T)\ln(u_T/u_T^*) \qquad (37)$$

Relation (36) suggests that the drag reduction slope modulus κ is physically related to the polymer chain deformation factor J, the effect of which might be obtained by classification according to (κ/b^3). From the data in Tables 1 and 3, the carbon-carbon and cellulosic skeleton polymers respectively yield $(\kappa/b^3)_{c\text{-}c}/(\kappa/b^3)_{cell} \simeq 6$, which accords with the carbon-carbon chain being more flexible than the cellulosic chain, the respective chain conformation factors being 1.8 and 3.5. The excitation integral, the second bracket on the right-hand side of (32), is evidently the usual dissipation integral with all ordinates altered by a (dimensionless) summation that couples the macromolecule to the flow field; the major contributions to the integral should therefore arise from the dissipative wave numbers. For a Newtonian flow, the highest turbulent strain rates occur at $y^+ \simeq 15$, which is then likely to be the radial location of maximum s′ prior to onset. When the variation of I^+ with friction velocity, as in (37), is plotted over the usual experimental range of (u_T/u_T^*), the function on the right-hand side of (37) increases rapidly from 0 at $(u_T/u_T^*) = 1$ to 0.2 at $(u_T/u_T^*) \simeq 1.2$ and then stays essentially unchanged at 0.32 ± 0.05 for $1.5 < (u_T/u_T^*) < 8$, implying that the excitation integral switches from one value, characteristic of Newtonian flow, to another, that is characteristic of drag reduction, over a rather narrow range of friction velocity.

In summary, the polymer-turbulence interaction responsible for drag reduction seems to commence in the neighborhood of the plane of peak turbulence energy production, $y^+ \simeq 15$, suggesting an involvement of the macromolecule in the turbulent bursting process. Macromolecular extension appears implicated in the interaction from the approximate equalities of macromolecular relaxation time and turbulent burst duration at onset and from the correlation of the effective slip with macromolecular strain energy. Whether the act of macromolecular elongation interferes with the burst or whether it is the elongated macromolecules which do so is unclear; nor is it known which part of the burst cycle is most affected. Concerning these questions, imagine an additive-burst matrix, the rows being macromolecular states, namely, (1) random-coiled, (2) coiling-uncoiling, and (3) extended, while the columns are burst events, namely, (1) lift-up, (2) growth, and (3) breakdown. Experiments on drag reduction by extended polyelectrolyte molecules and fibers provide information on row (3) exclusively, and their comparison with drag reduction by random-coiling macromolecules might then suggest the elements of interest in rows (1) and (2). The gross flow behavior of random-coiling macromolecule solutions and of collapsed polyelectrolytes on the one hand does indeed seem to differ strikingly from that of fiber suspensions and of extended polyelectrolytes on the other (Virk, 1975). In the former case, called Type A, a family of polymer solutions yields polymeric regime segments fanning outwards from a common onset point on the Prandtl-Karman line with slopes increasing with increasing additive concentration and drag reduction increasing with increasing $Re_f^{1/2}$. In the latter case, called Type B, a family of solutions of extended polyelectrolytes, say, yields polymeric regime segments roughly parallel to, but displaced upwards from, the Prandtl-Karman line with drag reduction essentially independent of $Re_f^{1/2}$ but increasing with increasing additive concentration. Perhaps Type A drag reduction results from the elastic deformation of the additive, whereas Type B drag reduction is characteristic of rigid, already extended additives.

3.3 Energy Balances

We examine how the mean and turbulent energy balances in Newtonian turbulent flow, for example, Laufer

(1954), Hinze (1959), Monim and Yaglom (1971), are altered during drag reduction, all comparisons being made at constant R^+ with neglect of differences between the polymer solution and solvent constitutive equations.

The local mean energy balance (Cartesian coordinates) reads

$$\underset{\text{I}}{(1-\xi)(R/2\rho)\,|dP/dx|} \quad \underset{\text{II}}{(dU/dy) = \nu(dU/dy)^2} \quad \underset{\text{III}}{-\langle uv\rangle\,(dU/dy)} \tag{38}$$

The energy available from the pressure gradient (I) suffers direct viscous dissipation (II = Dv) and causes turbulent energy production (III = Pr). Profiles of Dv and Pr have been determined experimentally in Newtonian flow (Laufer, 1954); during drag reduction these can only be inferred from eddy viscosity profiles such as presented in Figure 17, using the relations $Dv^+ = (1-\xi)/(\epsilon/\nu + 1)^2$ and $Pr^+ = Dv^+\epsilon/\nu$. The estimated variation of Dv^+ and of Pr^+ versus y^+ is sketched in Figure 19, arithmetic coordinates, for both Newtonian and maximum drag reduction flows at $R^+ = 1000$. The plane of peak turbulent energy production, at which $\epsilon/\nu = 1$, shifts from $y_{max,n}{}^+ = 12$ to $y_{max,m}{}^+ \simeq 28$. Integration of (38), normalized over the pipe cross section yields the overall mean energy balance

$$\underset{\text{I}}{(2U_{av}{}^+/R^+)} = \underset{\text{II}}{\int_0^1 Dv^+\, d(1-\xi)^2} + \underset{\text{III}}{\int_0^1 Pr^+\, d(1-\xi)^2} \tag{39}$$

Evaluation of the right-hand side terms in (39) from Figure 19 gives the integral direct viscous dissipation (II = $\int Dv^+$) and turbulent energy production (III = $\int Pr^+$) as follows: $(\int Dv^+, \int Pr^+)_n = (0.019, 0.019)$ and $(\int Dv^+, \int Pr^+)_m = (0.047, 0.046)$. Thus, at constant R^+, the ratio of total turbulent energy production to total direct viscous dissipation at a pipe cross section during maximum drag reduction appears to be essentially the same as in Newtonian flow. Good Dv^+ and Pr^+ profiles cannot be synthesized in the case of low drag reduction, for lack of eddy viscosity data in the near-wall region, but it may be surmised that $y_{max,n}{}^+ < y_{max,p}{}^+ < y_{max,m}{}^+$, that is, the peak production plane moves progressively away from the wall as drag reduction increases, and since $(\int Pr^+/\int Dv^+)_m \simeq (\int Pr^+/\int Dv^+)_n$, we might expect $(\int Pr^+/\int Dv^+)_p \simeq (\int Pr^+/\int Dv^+)_n$ also.

The local turbulent energy balance reads

$$\underset{\text{I}}{\langle uv\rangle\,(dU/dy)} + \underset{\text{II}}{\nu\langle(\partial u_j/\partial x_i)(\partial u_j/\partial x_i)\rangle} + \underset{\text{III}}{\partial\langle vq^2/2\rangle/\partial y} + \underset{\text{IV}}{\partial\langle vp/\rho\rangle/\partial y} - \underset{\text{V}}{\nu\,\partial^2\langle q^2/2\rangle/\partial y^2} = 0 \tag{40}$$

The terms in (40) respectively represent turbulent energy production (I = $-Pr$), dissipation (II = Di, with Cartesian tensor summation of indices i and j implied), turbulent transport of kinetic energy (III) and of potential energy (IV) by the radial velocity, and the molecular transport of turbulent kinetic energy (V); and integration of (40) across the pipe cross scetion shows that total turbulent energy production must equal the total dissipation of turbulent energy. A simplified picture of the turbulent energy balance in Newtonian pipe flow, considering only terms I, II, and III of (43), is as follows. At all radial locations, turbulence production and dissipation are approximately equal; in the core, $\xi > \xi_c \simeq 0.1$, or outer

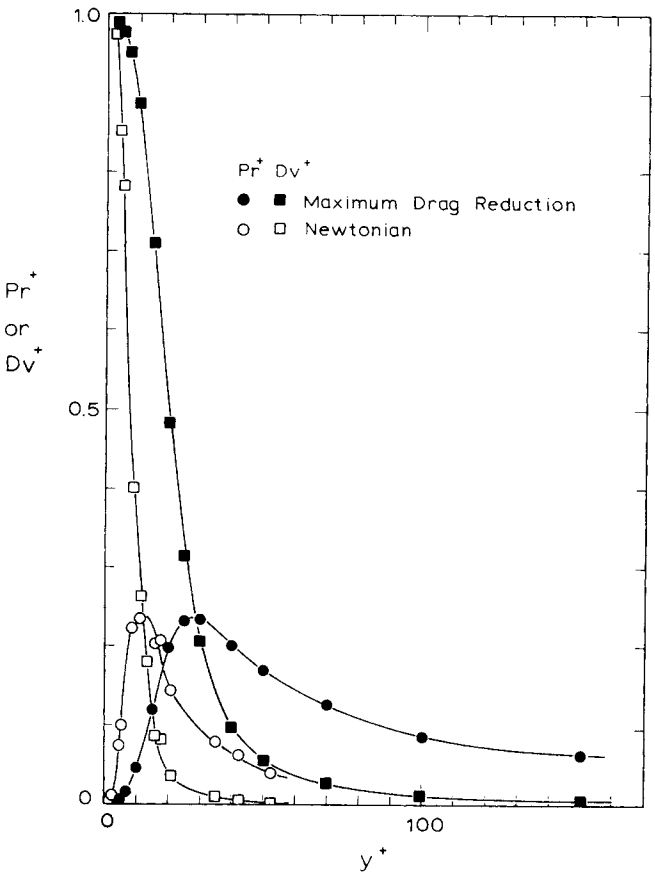

Fig. 19. Estimated direct viscous dissipation and turbulent energy production profiles in the wall region during Newtonian and maximum drag reduction flows at $R^+ = 1000$.

portion of the outer flow, $(Pr - Di) < 0$, the net energy shortfall being supplied by the diffusion of turbulent kinetic energy from the near-wall inner portion of the inner flow, $y^+ < y_i{}^+ \simeq 100$ where $(Pr - Di) > 0$. The region of inner-outer flow overlap, $y^+ > y_i{}^+$, $\xi < \xi_c$, has $(Pr - Di) \simeq 0$ and through this region there is an essentially constant flux $\simeq \rho u_T{}^3$ of kinetic energy in transit from $y^+ < y_i{}^+$ to $\xi > \xi_c$. The corresponding nondimensional turbulent kinetic energy profile is shown in Figure 20a which has an arithmetic ordinate q^+ and dual logarithmic abscissae $-y^+$ from the wall outward and ξ from the axis inward. The three zones are apparent:

1. The near-wall region, in which q^+ increases to a maximum:

$$q^+ \simeq (u'^+)^2 = (\alpha_n{}^+ y^+)^2; \quad 0 < y^+ < y_{max,n}{}^+ \tag{41}$$

2. The overlap region of nearly constant q^+:

$$q^+ \simeq q_{max,n}{}^+; \quad y^+ > y_{max,n}{}^+, \quad \xi < \xi_c \tag{42}$$

3. The core region, in which, strikingly, the energy excess essentially equals the velocity defect:

$$q^+ - q_n{}^+(1) = -(1/X_n)\ln\xi = U_n{}^+(1) - U^+; \quad \xi_c < \xi < 1.0 \tag{43}$$

Equations (41) to (43) are shown by solid lines in Figure 20a, providing an approximate description of the data. Turning to the polymer solutions, a partial kinetic energy profile can be synthesized from the data of Logan (1972) at low drag reduction. This is shown, along with corresponding results for solvent alone, in Figure 20b, which has the same abscissae as Figure 20a but an ordinate

$q_{uv}^+ = (u'^2 + v'^2)/u_T^2$ obtained from the intensity measurements shown in Figure 11. q_{uv}^+ should provide a good approximation to the actual q^+ in the region of the wall, up to q_{max}^+, where q is predominantly axial and should be about 2/3 of the actual q^+ in the core where the w'^2 component omitted makes a relatively constant contribution of 1/3 to q. In Figure 20b, the solid line on the left is $q_{uv}^+ \propto y^{+2}$ faired through the solvent data; it can be seen that $q_{max,p}^+$ for the polymer solution lies close to the extension of this line; also $q_{max,p}^+ - q_{max,n}^+ \simeq S^+$ as noted earlier. The solid line on the right is drawn with slope $-(2/3X_n)$ through $q_n^+(\xi = 1)$, and it can be seen that the polymer solution and solvent data straddle this line in the core $0.3 < \xi < 1$, establishing a Newtonian plug. In the region $y^+ > y_{max}^+$, $\xi < \xi_c$, the missing w' component and the relatively low R^+ hinder analysis, but the polymer solution q_{uv}^+ drops off more sharply than solvent reaching the latter level at $y^+ \simeq 100$, which marks the interface between the elastic sublayer and Newtonian plug regions. Now, if the core is essentially Newtonian during low drag reduction, then its energy requirement must also be. Hence, the usual Newtonian kinetic energy flux $\simeq \rho u_T^3$ must proceed from the region of production through the inner region to the inner edge of the core ξ_c. The observed increase in potential difference $q_{max,p}^+ - q_{\xi_c,p}^+ \simeq q_{max,p}^+ - q_{max,n}^+$ required to maintain the same flux must then reflect an increased resistance, or reduced turbulent diffusivity, of the intervening region, that is, the elastic sublayer. Since turbulent transport of kinetic energy occurs by a correlation term of form $\langle vq \rangle \simeq \langle vu^2 \rangle$, the coupling between v and u^2 must be reduced relative to Newtonian. Analogous arguments apply to turbulent momentum transport, which is possibly why $\Delta q_{max}^+ \simeq S^+$.

The interconversion of kinetic energy between axial and transverse components is also of interest. According to the usual interpretation (for example, by Hinze, 1959), all turbulent energy production feeds into the axial component, and then, if $u^2 > (v^2 + w^2)$, energy is transferred out of u^2, and into v^2 and w^2, by the pressure-velocity gradient correlation $\langle p(\partial u/\partial x) \rangle$, which thus tends to equalize all components, promoting isotropy. During drag reduction, the observation that $\alpha_p^+ \simeq \alpha_n^+$, (25), suggests that the energy production feeds into the axial component in the normal Newtonian fashion. However, the anisotropy, roughly measured by $u'^2 - (v'^2 + w'^2) \simeq u'^2$, markedly exceeds Newtonian in the wall region, which implies a greater resistance to the transfer of energy out of the axial and into the transverse components.

In summary, during low drag reduction, the outer flow structure and the viscous sublayer streaky structure are both Newtonian, as is the turbulent burst frequency, indicating that the overall cycle of events which sustain turbulent flow remains essentially Newtonian. In the near-wall region, the turbulent energy produced feeds normally into the axial component of the turbulent kinetic energy, but the macromolecules appear to hinder the transfer of energy between axial and transverse components and decrease the correlation between the axial and radial flow fields, thus reducing the turbulent diffusivity and retarding turbulent transport. To maintain the usual Newtonian energy flux from wall to core, despite the increased resistance of the intervening region, apparently forces the flow to increase the potential difference, that is, to increase $q_{max}^+ \simeq u_{max}'^{2+}$. The turbulent energy production, which feeds u^2, is a product of two terms of which $\langle uv \rangle / u_T^2$ is, if anything, lower than Newtonian while (dU^+/dy^+) is not much different from its maximum value of unity in the region of interest. Therefore, to achieve a higher u'^{2+} than Newtonian, the region of high velocity gradient must persist for a greater distance from the wall. This would appear to be the essential source of the effective slip associated with drag reduction.

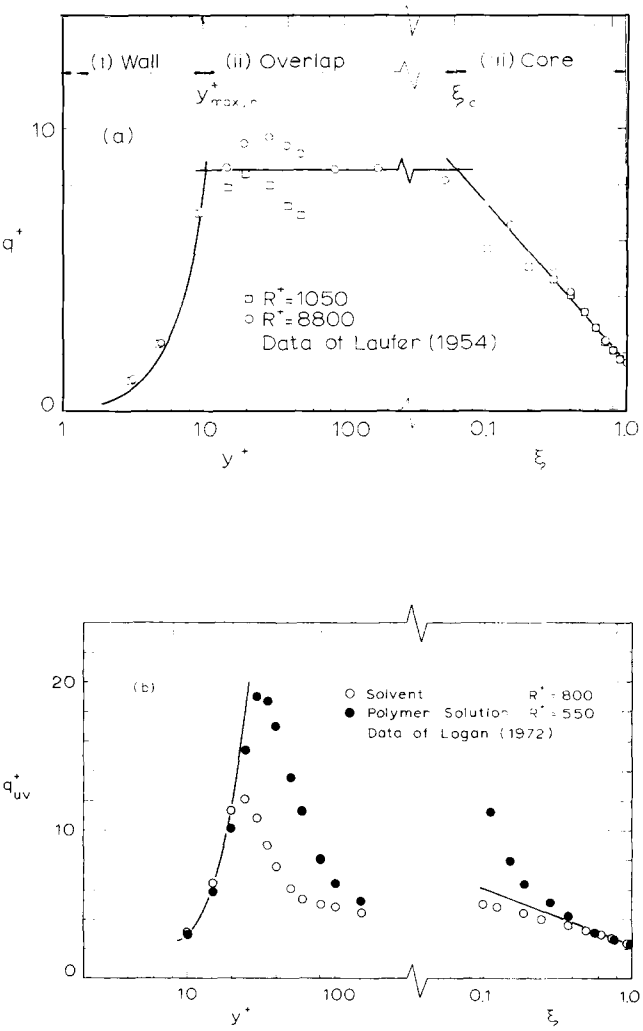

Fig. 20. Turbulent kinetic energy profiles: (a) Newtonian flow (after Laufer, 1954); (b) Low drag reduction (after Logan, 1972).

The preceding paragraph, and the last paragraph in Section 3.2, are the elements of our drag reduction mechanism.

4. SUMMARY

4.1 Experimental Evidence

1. Three major gross-flow features of drag reduction by dilute solutions of random-coiling macromolecules in turbulent pipe flows have been identified:

(1) The onset of drag reduction, rather abruptly, at a characteristic wall shear stress.
(2) A polymeric regime in which the observed friction factor relations depend upon polymeric parameters, namely, the polymer species-solvent pair, polymer molecular weight, and concentration.
(3) A maximum drag reduction asymptote which is insensitive to polymeric parameters, being universally,

$$f^{-1/2} = 19.0 \log_{10} Ref^{1/2} - 32.4 \qquad (4)$$

The drag reduction phenomenon appears bounded between the Prandtl-Karman law for Newtonian turbulent flow (2) and (4).

2. The friction factor relation exhibited by a given polymer solution in the polymeric regime can be experimentally

characterized by two parameters, namely, the onset wall shear stress T_w^* (or, equivalently, the onset wave number W^*) and the Prandtl-Karman slope increment δ:

$$f^{-1/2} = (4.0 + \delta) \log_{10} Ref^{1/2} - 0.4 - \delta \log_{10} \sqrt{2} dW^* \quad (3)$$

The onset wall shear stress is essentially independent of pipe diameter, polymer concentration, and solvent viscosity, and varies inversely as the two to three power of polymer radius of gyration. An approximate onset correlation is

$$T_w^* R_G^3 = \Omega_T \quad (5)$$

with Ω_T an onset constant, characteristic of a polymer species-solvent pair. The slope increment is essentially independent of pipe diameter, varies as the square root of polymer concentration and as the three-halves power of the number of chain links in the polymer backbone, and seems unaffected by decreases in polymer excluded volume. A slope increment correlation is

$$\delta = \kappa (c/M)^{1/2} N^{3/2} \quad (6)$$

with κ a slope modulus, characteristic of a polymer species-solvent pair. There are preliminary indications that both Ω_T and κ are influenced by the skeletal structure of the polymer species while being unaffected by the solvent strength.

3. Mean velocity profiles during drag reduction show two characteristic extremes: at low drag reduction the entire outer flow, $y^+ > 50$, say, is shifted upward from but parallel to the Newtonian law of the wall by an amount S^+, the effective slip, whereas at maximum drag reduction the ultimate velocity profile has a semilogarithmic form similar to the Newtonian wall law but with a mixing length constant $X_m = 0.085$, about a fifth of the Newtonian $X_n = 0.40$. The general mean velocity profile thus comprises three zones:

(1) The usual viscous sublayer

$$U^+ = y^+; \quad 0 \leq y^+ \leq y_v^+ \quad (7)$$

(2) An elastic sublayer, characteristic of drag reduction, in which the profile can be approximated by a segment of the ultimate profile sufficient to yield the effective slip

$$U^+ = 11.7 \ln y^+ - 17.0; \quad y_v^+ < y^+ < y_e^+ \quad (9)$$

(3) A Newtonian plug region, with Newtonian mixing length constant, in which the profile is parallel-shifted upward by S^+ relative to the Newtonian law of the wall

$$U^+ = 2.5 \ln y^+ + 5.5 + 9.2 \ln (y_e^+/y_v^+); \quad y_e^+ \leq y^+ \leq R^+ \quad (8) + (13)$$

The elastic sublayer segment (2) arises at the onset, prior to which the mean velocity profile consists only of segments (1) and (3) with $S^+ = 0$, that is, the Prandtl-Taylor approximation for Newtonian turbulent flow. In the polymeric regime, the elastic sublayer grows with increasing drag reduction, the profile showing all three segments, with zone (2) increasing at the expense of zone (3). At maximum drag reduction, the elastic sublayer extends to the pipe axis, the profile consisting only of segments (1) and (2).

4. Turbulence structure information, available only in the polymeric regime, also suggests the existence of three radial zones, analogous to (but not identical with) those observed in the mean velocity profiles:

(1) The viscous sublayer. In this region, the Newtonian streaky structure semes to remain at least partially intact during drag reduction, with the axial intensity gradient at the wall and the aspect ratio of transverse macroscales both essentially the same as Newtonian.

(2) The elastic sublayer. Here the turbulence structure during drag reduction is significantly different from Newtonian: relatively, the (nondimensional) axial intensity is higher while the radial intensity, turbulent shear stress, and u-v correlation coefficient are all lower. The maximum turbulent kinetic energy appears to exceed Newtonian by roughly the same amount S^+ that the maximum mean velocity exceeds Newtonian.

(3) The Newtonian plug. In this region, the turbulence structure during drag reduction appears to be the same as Newtonian based on measurements of axial and radial intensities.

4.2 Physical Interpretation

1. The polymer-turbulence interaction responsible for drag reduction appears to commence in the vicinity $y^+ \simeq 15$ of the plane of peak turbulent energy production, suggesting that the polymer molecules interfere with the turbulent bursting processes.

2. At the onset of drag reduction the duration of a turbulent burst is of order the terminal relaxation time of a macromolecule and after onset the extent of drag reduction correlates with the turbulent strain energy of the dilute polymer solution. These observations suggest that macromolecular extension is involved in the mechanism of drag reduction. At onset, the random-coiled radius of gyration of the macromolecule is about 10^{-3} times the smallest turbulent burst length scale.

3. The axial and radial turbulent flow fields are decoupled in the region of interaction, as witnessed by a striking reduction in the u-v correlation coefficient, relative to Newtonian. The polymer-induced flow field decoupling seems to retard about equally the radial transport of axial momentum and of turbulent kinetic energy. The observed drag reduction is possibly a consequence of the readjustments, notably an increase in maximum kinetic energy, that the inner flow makes to maintain the overall cross-sectional turbulent energy balance.

ACKNOWLEDGMENTS

The author is indebted to the Editor of this Journal for his assistance and encouragement in the preparation of this review. Professor K. A. Smith offered many helpful comments during discussions of the manuscript. Dr. F. R. Cottrell suggested the polymer sample heterogeneity index. H. Doris Fall and Margaret Quarrie were extremely helpful in typing the manuscript. Machine computations were performed at the IIT/Madras Computer Center.

NOTATION

a, K = Mark-Houwink parameters, Equation (17)
A, B = coefficients in Equation (10)
$\hat{A}, \hat{B}$ = coefficients in Equation (11)
b = effective bond length per backbone chain link
c = concentration of polymeric solute, in parts per million by weight (wppm)
C_{uv} = correlation coefficient $(<uv>/<u^2>^{1/2}<v^2>^{1/2})$
d = pipe inside diameter
$E(k)$ = turbulent kinetic energy density at k
f = Fanning's friction factor $(2T_w/\rho U_{av}^2)$
g = exponent in Relation (20)
G = strain (or shear) rate

H = heterogeneity index, defined by Equation (18)
I = excitation integral, in Equation (32)
J = chain deformation factor, defined by Equation (30)
$\mathbf{k}$ = Boltzmann's constant
k = wave number
L, L_C = macromolecule end-to-end distances, root mean square, contour
m_0 = molecular weight per backbone chain link
M, M_w, M_n = polymer molecular weights; unspecified (usually weight), weight, number, averages
$\mathbf{N}$ = Avogadro's number
N = number of backbone chain links in macromolecule (M/m_0)
p, P = pressures; fluctuating, mean
q = turbulent kinetic energy
Q = volumetric flow rate
R = pipe radius (half width for noncircular cross sections)
R_F = fractional drag reduction $[1 - (f/f_n)_{Re}]$
R_G = macromolecule root mean square radius of gyration, z-average
Re = Reynolds number (dU_{av}/ν)
Re' = generalized (power-law) Reynolds number
s_{mol} = strain energy of a macromolecule
s, S = strain energies of a polymer solution; fluctuating, mean
S^+ = effective slip $(U_{av,p}{}^+ - U_{av,n}{}^+)_{R^+}$, also see Equation (13)
S_F = fractional flow enhancement $[-1 + (f^{-1/2}/f_n{}^{-1/2})_{Ref^{1/2}}]$
$\mathbf{T}$ = temperature
T_w = wall shear stress
u, v, w = fluctuating velocity components in x, y, z directions
u_T = friction velocity $(T_w/\rho)^{1/2}$
U, U_{av}, U_x = mean velocities in x direction; local, bulk average, free stream
W^* = onset wave number ($u_T{}^*/\nu_s$)
x, y, z = Cartesian coordinates in axial, radial, azimuthal directions with origin at pipe wall
X = mixing length constant
y = distance from pipe wall
Z = azimuthal streak spacing

Greek Letters

α^+ = axial intensity gradient at wall, $\mathrm{Lim}_{y^+ \to 0}\ (du'^+/dy^+)$
α_η, α_R = Flory excluded volume (or 'expansion') factors, viscosity-, R_G-based
β = parameter of a polymer solution being strained ($\tau_0 G$)
γ, ζ = coefficients in Equations (23a) and (23c)
δ = slope increment, $(df^{-1/2}/d\log_{10}Ref^{1/2})_p - 4.0$
Δ_* = momentum thickness of a boundary layer
ϵ = eddy (shear) viscosity $<uv>/(dU/dy)$
η = viscosity
η_{rel} = viscosity (polymer solution) relative to solvent
$[\eta]$ = intrinsic viscosity
θ_{bb}, θ_b = mean time between bursts, burst duration
κ = slope modulus, Equations (6) and (22)
λ_b, Λ_b = burst dissipation wavelength, streak width at liftup
$\mu_j(j,k)$ = an eigenvalue summation for jth mode (of n total) at kth wave number, see Equation (32)
ν = kinematic viscosity
ξ = radius-normalized distance from wall (y/R)
Π = intrinsic slope increment, Equation (22)
ρ = density
σ = macromolecule chain conformation factor ($R_{G,o}/R_{G,of}$)
τ_0 = macromolecular (relaxation) time scale ($M[\eta]\,\eta_s/\mathbf{NkT}$)
τ_t, τ_j = Zimm theory relaxation times, terminal ($0.42\,\tau_0$), jth mode
ϕ = ratio of Reynolds to total shear stresses $<uv>/u_T{}^2(1-\xi)$
Φ = Flory's viscosity constant
ψ = polymer solution parameter, Equation (15b)
ω_b = $(2\pi/\theta_b)$
Ω_T, Ω_L = onset constants, time- and length-based, Equations (19), (5)

Subscripts

b = burst
c, e, i, v = regions of pipe cross section: inner edge of core, outer edge of elastic sublayer, outer edge of inner flow, outer edge of viscous sublayer
i, j = dummy indices
n, p, m = gross flow regimes: Newtonian, polymeric, maximum drag reduction
max = maximum, or at location of maximum
o, of = unperturbed (in theta solvent), unperturbed with free rotation about bonds
s = based on solvent viscosity and density
tr = at transition from laminar to turbulent flow
w = at wall, $\xi = 0$
1 = at axis, $\xi = 1$

Superscripts

* = at onset of drag reduction
$^+$ = normalized by inner scales, u_τ and ν
$'$ = root mean square turbulent quantity
$''$ = deformed macromolecule
0 = for monodisperse polymer

Other Symbols

$<>$ = time average
var = error variance
m = salt solution molality
ν = percent error operator, for example, $\epsilon(\delta) = 100[\mathrm{var}(\delta)]^{1/2}/\delta$

LITERATURE CITED

Arunachalam, V., R. W. Hummel, and J. W. Smith, "Flow Visualization Studies of a Turbulent Drag Reducing Solution," *Can. J. Chem. Eng.*, **50**, 337 (1972).

Astarita, G., G. Greco, and L. Nicodemo, "Phenomenological Interpretation and Correlation of Drag Reduction," *AIChE J.*, **15**, 564 (1969).

Bailey, F. E., and R. W. Callard, "Some Properties of Poly(Ethylene Oxide) in Aqueous Solution," *J. Appl. Polym. Sci.*, **1**, 56 (1959).

Batchelor, G. K., "The Stress Generated in a Non-Dilute Suspension of Elongated Particles by Pure Straining Motion," *J. Fluid Mech.*, **46**, 813 (1971).

Beech, D. R., and C. Booth, "Unperturbed Dimensions of Poly(Ethylene Oxide)," *J. Polym. Sci. Ser. A2*, **7**, 575 (1969).

Berman, N. S., and W. K. George, "Onset of Drag Reduction in Dilute Polymer Solutions," *Phys. Fluids*, **17**, 250 (1974).

Bilgen, E., "The Stability of Viscoelastic Flow Due to a Rotating Disk," *Chem. Eng. Progr. Symp. Ser. No. 111*, **67**, 74 (1971).

Bird, R. B., H. R. Warner, and D. C. Evans, "Kinetic Theory of Dumbbell Suspensions with Brownian Motion," *Fortschr. Hochpolym. Forsh*, **8**, 1 (1971).

Black, T. J., "Viscous Drag Reduction Examined in the Light of a New Model of Wall Turbulence," in *Viscous Drag Reduction*, pp. 383-407, C. S. Wells (Ed.), Plenum Press, New York (1969).

Boggs, F. W., "Relationship Between Flow Pattern, Constitutive Equation and Molecular Structure," *ibid.*, pp. 475-485.
Brandrup, T., and E. H. Immergut, *The Polymer Handbook*, Interscience, New York (1966).
Bremhorst, K., and T. B. Walker, "Spectral Measurements of Turbulent Momentum Transfer in Fully Developed Pipe Flow," *J. Fluid Mech.*, **61**, 173 (1973).
Brennen, C., and G. E. Gadd, "Aging and Degradation in Dilute Polymer Solutions," *Nature*, **215**, 1368 (1967).
Brown, W., "Hydroxyethycellulose—Macromolecular Properties in Solution," *Arkiv. Kemi.*, **18**, 227 (1961).
———., D. Henley, and J. Ohman, "Hydroxyethyl Cellulose in Dilute Solution," *Makromol. Chem.*, **64**, 49 (1963).
Castro, W. E., and W. Squire, "The Effect of Polymer Additives on Transition in Pipe Flow," *Appl. Sci. Res.*, **18**, 81 (1967).
Cerf, R., "Sur l Extension Des Macromolecules en Chaines par un Champ de Vitesses," *C. R. Acad. Sci. Paris Ser. C*, **267**, 1112 (1968).
Chung, J. S., and W. P. Graebel, "Laser Anemometer Measurements of Turbulence in Non-Newtonian Pipe Flows," *Phys. Fluids*, **15**, 546 (1972).
Chinai, S. N., J. D. Matlack, and A. L. Resnick, "Polymethyl Methacrylate Dilute Solution Properties by Viscosity and Light Scattering," *J. Polym. Sci.*, **17**, 391 (1955).
Clarke, W. B., "Polyelectrolytes in Solution—Their Conformation and Turbulent Flow Characteristics," Sc.D. thesis, Mass. Inst. Tech., Cambridge, Mass. (1970).
Corino, E. R., and R. S. Brodkey, "A Visual Investigation of the Wall Region in Turbulent Flow," *J. Fluid Mech.*, **37**, 1 (1969).
Cottrell, F. R., "The Conformation of Polyisobutylene in a Hydrodynamic Shear Field," Sc.D. thesis, Mass. Inst. Tech., Cambridge, Mass. (1968).
———., E. W. Merrill, and K. A. Smith, "Conformation of Polyisobutylene in Dilute Solution Subjected to a Hydrodynamic Shear Field," *J. Polym. Sci. Ser. A2*, **7**, 1415 (1969).
Deb, S. K., and S. N. Mukherjee, "Molecular Weight and Dimensions of Guar Gum from Light Scattering in Solution," *Indian J. Chem.*, **1**, 413 (1963).
Donohue, G. L., W. C. Tiederman, and M. M. Reischman, "Flow Visualization of the Near-Wall Region in a Drag-Reducing Channel Flow," *J. Fluid Mech.*, **56**, 559 (1972).
Eckelman, L. D., G. Fortuna, and T. J. Hanratty, "Drag Reduction and the Wavelength of Flow-Oriented Wall Eddies," *Nature*, **236**, 94 (1972).
Elata, C., and J. Tirosh, "Frictional Drag Reduction," *Israel J. Technol.*, **3**, 1 (1965).
Elata, C., J. Lehrer, and A. Kahanovitz, "Turbulent Shear Flow of Polymer Solutions," *ibid.*, **4**, 87 (1966).
Ernst, W. D., "Investigation of the Turbulent Shear Flow of Dilute Aqueous CMC Solutions," *AIChE J.*, **12**, 581 (1966).
Fabula, A. G., J. L. Lumley, and W. D. Taylor, "Some Interpretations of the Toms Effect," in *Mechanics of Continua*," pp. 100-120, S. Eskanazi (Ed.), Academic Press, New York (1966).
Flory, P. J., *Principles of Polymer Chemistry*, Cornell Univ. Press, Ithaca, New York (1953).
———., *Statistical Mechanics of Chain Molecules*, Wiley, New York (1969).
Fortuna, G., and T. J. Hanratty, "The Influence of Drag-Reducing Polymers on Turbulence in the Viscous Sublayer," *J. Fluid Mech.*, **53**, 575 (1972).
Friehe, C. A., and W. H. Schwarz, "The Use of Pitot-Static Tubes and Hot Film Anemometers in Dilute Polymer Solutions," in *Viscous Drag Reduction*, pp. 281-296, C. S. Wells (Ed.), Plenum Press, New York (1969).
Gadd, G. E., "Reduction of Turbulent Friction by Dissolved Additives," *Nature*, **212**, 874 (1966).
———., "Reduction of Turbulent Drag in Liquids," *Nature PS*, **230**, 29 (1971).
Giles, W. B., "Similarity Laws for Friction-Reduced Flow," *J. Hydronautics*, **2**, 34 (1968).
———., and W. T. Pettit, "Stability of Dilute Viscoelastic Flow," *Nature*, **216**, 470 (1967).
Gordon, R. J., and C. Balakrishnan, "Vortex Inhibitions: A New Viscoelastic Effect with Importance in Drag Reduction and Polymer Characterisation," *J. Appl. Polym. Sci.*, **16**, 1629 (1972).
Goren, Y., and J. F. Norbury, "Turbulent Flow of Dilute Aqueous Polymer Solutions," *ASME J. Basic Eng.*, **89**, 814 (1967).
Grass, A. J., "Structural Features of Turbulent Flow over Smooth and Rough Boundaries," *J. Fluid Mech.*, **50**, 233 (1971).
Hansen, R. J., "The Reduced Drag of Polymer Solutions in Turbulent and Transient Laminar Shear Flows," *ASME J. Fluids Eng.*, **1**, 23 (1973).
———., and R. C. Little, "Pipe Diameter, Molecular Weight, and Concentration Effects on the Onset of Drag Reduction," *AIChE Symposium Series No. 111*, **67**, 93 (1971).
Hershey, H. C., and J. L. Zakin, "A Molecular Approach to Predicting the Onset of Drag Reduction in the Turbulent Flow of Dilute Polymer Solutions," *Chem. Eng. Sci.*, **22**, 1847 (1967).
———., "Existence of Two Types of Drag Reduction in Pipe Flow of Dilute Polymer Solutions," *Ind. Eng. Chem. Fundamentals*, **6**, 381 (1967).
Hinch, E. J., "Models of Dilute Polymer Solutions for Strong Flows with Large Polymer Deformation," paper presented to C.N.R.S. Colloque Intern. Polymeres et Lubrification, Brest (1974).
———., and L. G. Leal, "Time-Dependent Shear Flows of a Suspension of Particles with Weak Brownian Rotations," *J. Fluid Mech.*, **57**, 753 (1973).
Hinze, J. O., *Turbulence*, McGraw-Hill, New York (1959).
Hoyt, J. W., "A Turbulent Flow Rheometer," in *Symposium on Rheology*, pp. 71-80, A. W. Marris and J. T. S. Wang (Eds.), ASME, New York (1965).
———., and A. G. Fabula, "The Effect of Additives on Fluid Friction," in *Proc. Fifth Symp. on Naval Hydrodynamics*, pp. 947-970, Bergen, Norway ONR-ACR 112 (1964).
Hoyt, J. W., "The Effect of Additives on Fluid Friction," *ASME J. Basic Eng.*, **94**, 258 (1972).
Huang, T. T., and N. Santelli, "Drag Reduction and Degradation of Dilute Polymer Solutions in Turbulent Pipe Flows," NSRDC Washington, D.C. Report No. 3677 (1971).
James, D. F., and A. J. Acosta, "The Laminar Flow of Dilute Polymer Solutions Around Circular Cylinders," *J. Fluid Mech.*, **42**, 269 (1970).
Kim, O. K., R. C. Little, and R. Y. Ting, "Polymer Structural Effects in Turbulent Drag Reduction," *Chem. Eng. Progr. Symp. Ser. No. 130*, **69**, 39 (1973).
Kim, H. T., S. J. Kline, and W. C. Reynolds, "The Production of Turbulence Near a Smooth Wall in a Turbulent Boundary Layer," *J. Fluid Mech.*, **50**, 133 (1971).
Klebanoff, P. S., "Characteristics of Turbulence in a Boundary Layer with Zero Pressure Gradient," NACA Report 1247 (1955).
Kline, S. J., W. C. Reynolds, F. A. Schraub, and P. W. Runstadler, "The Structure of Turbulent Boundary Layers," *J. Fluid Mech.*, **30**, 741 (1967).
Koleske, J. V., and S. F. Kurath, "Configuration and Hydrodynamic Properties of Fully Acetylated Guaran," *J. Polym. Sci. Ser. A2*, **2**, 4123 (1964).
Landahl, M. T., "Drag Reduction by Polymer Addition," in *Proc. 13th Intern. Congr. Theor. and Appl. Mechanics*, Moscow, pp. 177-199, E. Becker and G. K. Mikhailov (Eds.), Springer-Verlag, Berlin (1973).
———., and F. Bark, "Application of a Two-Scale Boundary Layer Turbulence Model to Drag Reduction," paper presented to C.N.R.S. Colloque Intern. Polymeres et Lubrification, Brest (1974).
Laufer, J., "The Structure of Turbulence in Fully Developed Pipe Flow," NACA Report No. 1174 (1954).
Lee, T. S., "Turbulent Flow of Dilute Polymer Solutions—Studies in Couette Flow," Sc.D. thesis, Mass. Inst. Tech., Cambridge, Mass. (1966).
Liaw, G. C., "Effect of Polymer Structure on Drag Reduction in Non-Polar Solvents," Ph.D. thesis, Univ. of Missouri, Rolla (1968).
———., J. L. Zakin, and G. K. Patterson, "The Effects of Molecular Characteristics of Polymers on Drag Reduction," *AIChE J.*, **17**, 391 (1971).

Little, R. C., "Drag Reduction by Dilute Polymer Solutions in Turbulent Flow," Naval Research Lab. Report No. 6542 (Clearinghouse AD 654160) (1967).
Lodge, A. S., and Y. Wu, "Constitutive Equations Derived from the Bead-Spring Model of Rouse and Zimm," *Rheol. Acta*, **10**, 539 (1971).
Logan, S. E., "Laser Velocimeter Measurement of Reynolds Stress and Turbulence in Dilute Polymer Solutions," *AIAA J.*, **10**, 962 (1972).
Lumley, J. L., "Drag Reduction by Additives" in *Ann. Reviews of Fluid Mechanics*, Vol. 1, W. R. Sears (Ed.), Annual Reviews Inc., Palo Alto, Calif. (1969).
———., "Drag Reduction in Turbulent Flow by Polymer Additives," *Macromol. Rev.*, **7**, 263 (1973).
———., "Applicability of the Oldroyd Constitutive Equation to Flow of Dilute Polymer Solutions," *Phys. Fluids*, **14**, 2282 (1971).
McIntyre, D., and F. Gornick, "Light Scattering from Dilute Polymer Solutions," Gordon and Breach, New York (1964).
McNally, W. A., "Heat and Momentum Transport in Dilute Polyethylene Oxide Solutions," Ph.D. thesis, Univ. of Rhode Island (1968).
Metzner, A. B., and M. G. Park, "Turbulent Flow Characteristics of Viscoelastic Fluids," *J. Fluid Mech.*, **20**, 291 (1964).
Metzner, A. B., and A. P. Metzner, "Stress Levels in Rapid Extensional Flows of Polymeric Fluids," *Rheol. Acta.*, **9**, 174 (1970).
Meyer, W. A., "A Correlation of the Frictional Characteristics for Turbulent Flow of Dilute Viscoelastic Non-Newtonian Fluids in Pipes," *AIChE J.*, **12**, 522 (1966).
Monim, A. S., and A. M. Yaglom, *Statistical Fluid Mechanics*, MIT Press, Cambridge, Mass. (1972).
Mysels, K. J., "Flow of Thickened Fluids," U.S. Patent 2,492,173, Dec. 27, 1949 (1949).
Nychas, S. G., H. C. Hershey, and R. S. Brodkey, "A Visual Study of Turbulent Shear Flow," *J. Fluid Mech.*, **61**, 513 (1973).
Offen, G. R., and S. J. Kline, "Combined Dye-Streak and Hydrogen-Bubble Visual Observations of a Turbulent Boundary Layer," *ibid.*, **62**, 223 (1974).
Ohara, M., "Triggered Laminar-to-Turbulent Transition in Pipe Flows of Dilute Polymer Solutions," S.M. thesis, Mass. Inst. Technol., Cambridge (1968).
Oldroyd, J. G., "A Suggested Method of Detecting Wall Effects in Turbulent Flow Through Pipes," in *Proc. First Intern. Congr. on Rheol.*, pp. 130-134, Vol. II, North Holland, Amsterdam (1948).
Oliver, D. R., and R. Bragg, "Development of the Triple-Jet System for Extensional Viscosity Measurement of Polymer Solutions," paper presented to CNRS Colloque Intern. Polymers et Lubrification, Brest (1974).
Paterson, R. W., and F. H. Abernathy, "Turbulent Flow Drag Reduction and Degradation with Dilute Polymer Solutions," *J. Fluid Mech.*, **43**, 689 (1970).
———., "Transition to Turbulence in Pipe Flow for Water and Dilute Solutions of Polyethylene Oxide," *ibid.*, **51**, 177 (1972).
Patterson, G. K., and G. L. Florez, "Velocity Profiles During Drag Reduction," in *Viscous Drag Reduction*, pp. 233-250, C. S. Well (Ed.), Plenum Press, New York (1969).
Patterson, G. K., J. L. Zakin, and J. M. Rodrigues, "Drag Reduction—Polymer Solutions, Soap Solutions and Solid Particle Suspensions in Pipe Flow," *Ind. Eng. Chem.*, **61**, 22 (1969).
Peterlin, A., "Mean Dimensions of Macromolecular Coil in Laminar Flow," *J. Chem. Phys.*, **39**, 224 (1963).
———., "Molecular Model of Drag Reduction by Polymer Solutes," *Nature*, **227**, 598 (1970).
———., "Hydrodynamics of Linear Macromolecules," *Pure Appl. Chem.*, **12**, 563 (1966).
Preston, J. L., "The Toms Phenomenon in a Rough Pipe," S.B. thesis, Mass. Inst. Tech., Cambridge (1968).
Pruitt, G. T., B. Rosen, and H. R. Crawford, "Effect of Polymer Coiling on Drag Reduction," Western Co., Dallas, Texas, Report No. DTMB-2 (1966).
Pruitt, G. T., N. F. Whitsitt, and H. R. Crawford, Western Co., Dallas, Texas, Report No. NAS 7-369 (1967).
Pyun, C. W., and M. Fixman, "Pertubation Theory of the Intrinsic Viscosity of Polymer Chains," *J. Chem. Phys.*, **44**, 2107 (1966).
Ram, A., E. Finkelstein, and C. Elata, "Reduction of Friction in Oil Pipelines by Polymer Additives," *Ind. Eng. Chem. Process Design Develop.*, **6**, 381 (1967).
Rao, K. N., R. Narasimha, and M. A. Badrinarayan, "Bursts in Turbulent Shear Flow," *J. Fluid Mech.*, **48**, 339 (1971).
Rodrigues, J. M., J. L. Zakin, and G. K. Patterson, "Correlation of Drag Reduction with Modified Deborah Number for Dilute Polymer Solutions," *Soc. Petrol. Eng. J.*, **7**, 325 (1967).
Rollin, A., and F. A. Seyer, "Velocity Measurements in Turbulent Flow of Viscoelastic Solutions," *Can. J. Chem. Eng.*, **50**, 714 (1972).
Rotta, J., "Experimenteller Beitrag zur Entstehung Turbulenter Stromung im Rohr," *Ing. Arch.*, **24**, 258 (1956).
Rudd, M. J., "Laser Dopplermeter and Polymer Drag Reduction," *Chem. Eng. Progr. Symp. Ser. No. 111*, **67**, 21 (1971).
———., "Measurements Made on a Drag Reducing Solution with a Laser Velocimeter," *Nature*, **224**, 587 (1969).
Sakanishi, A., "Dynamic Viscoelastic Properties of Dilute Polyisobutylene Solutions," *J. Chem. Phys.*, **48**, 3850 (1968).
Schlichting, H., *Boundary Layer Theory*, 4th Edit., McGraw-Hill, New York (1960).
Seyer, F. A., and A. B. Metzner, "Turbulence Phenomena in Drag Reducing Systems," *AIChE J.*, **15**, 426 (1969).
———., "Drag Reduction in Large Tubes," *Can. J. Chem. Eng.*, **47**, 525 (1969).
Shin, H., "Reduction of Drag in Turbulence by Dilute Polymer Solutions," Sc.D. thesis, Mass. Inst. Tech., Cambridge (1965).
Smith, K. A., E. W. Merrill, H. S. Mickley, and P. S. Virk, "Anomalous Pitot Tube and Hot Film Measurements in Dilute Polymer Solutions," *Chem. Eng. Sci.*, **22**, 619 (1967).
Smith, K. A., E. W. Merrill, and H. Banijamali, "Elongation of Drag-Reducing Macromolecules by a Pure Straining Motion," Paper presented to C.N.R.S. Colloque Intern. Polymeres et Lubrification, Brest (1974).
Spangler, J. G., "Studies of Viscous Drag Reduction with Polymers Including Turbulence Measurements and Roughness Effects" in *Viscous Drag Reduction*, pp. 131-155, C. S. Wells (Ed.), Plenum Press, New York (1969).
Sylvester, N. D., and S. M. Kumor, "Degradation of Dilute Polymer Solutions in Turbulent Tube Flow," *Chem. Eng. Progr. Symp. Ser. No. 130*, **69**, 69 (1973).
Tanford, C., *The Physical Chemistry of Macromolecules*, Wiley, New York (1961).
Taylor, A. R., and S. Middleman, "Turbulent Dispersion in Drag-Reducing Fluids," *AIChE J.*, **20**, 454 (1974).
Toms, B. A., "Some Observations on the Flow of Linear Polymer Solutions Through Straight Tubes at Large Reynolds Numbers" in *Proc. First Intern. Congr. on Rheology*, Vol. II, pp. 135-141, North Holland, Amsterdam (1948).
Treolar, L. R. G., *The Physics of Rubber Elasticity*, 2nd edit., Clarendon (1958).
Van Driest, E. R., "Turbulent Drag Reduction of Polymeric Solutions," *J. Hydronautics*, **4**, 120 (1970).
———., "The Damping of Turbulent Flow by Long-Chain Molecules," (Clearinghouse AD 660883) (1967).
Virk, P. S., "Drag Reduction in Rough Pipes," *J. Fluid Mech.*, **45**, 225 (1971).
———., "An Elastic Sublayer Model for Drag Reduction by Dilute Solutions of Linear Macromolecules," *ibid.*, 417.
———., "Drag Reduction by Collapsed and Extended Polyelectrolytes," *Nature*, **253**, 109 (1975).
———., "Turbulent Kinetic Energy Profile During Drag Reduction," *Phys. Fluids*, **18**, 419 (1975).
Virk, P. S., E. W. Merrill, H. S. Mickely, and K. A. Smith, "The Critical Wall Shear Stress for Reduction of Turbulent Drag in Pipe Flow" in *Mechanics of Continua*, pp. 37-52, S. Eskanazi (Ed.), Academic Press, New York (1966).
———., and E. L. Mollo-Christensen, "The Toms Phenomenon—Turbulent Pipe Flow of Dilute Polymer Solutions," *J. Fluid Mech.*, **30**, 305 (1967).
Virk, P. S., and E. W. Merrill, "The Onset of Dilute Polymer Solution Phenomena," in *Viscous Drag Reduction*, pp. 107-130, C. S. Wells (Ed.), Plenum Press, New York (1969).

Virk, P. S., H. S. Mickley, and K. A. Smith, "The Ultimate Asymptote and Mean Flow Structure in Toms Phenomenon," *ASME J. Appl. Mech.*, **37**, 488 (1970).
Virk, P. S., and H. Baher, "The Effect of Polymer Concentration on Drag Reduction," *Chem. Eng. Sci.*, **25**, 1183 (1970).
Virk, P. S., and T. Suraiya, "Mass Transfer at Maximum Drag Reduction," (submitted).
Walsh, M., "Theory of Drag Reduction in Dilute High Polymer Flows," *Intern. Shipbldg. Progr.*, **14**, 134 (1967).
Wang, C. B., "Correlation of the Friction Factor for Turbulent Pipe Flow of Dilute Polymer Solutions," *Ind. Eng. Chem.*, **11**, 546 (1972).
Wells, C. S., "Anomalous Flow of Non-Newtonian Fluids," *AIAA J.*, **3**, 1800 (1965).
———., and J. G. Spangler, "Injection of a Drag-Reducing Fluid into Turbulent Pipe Flow of a Newtonian Fluid," *Phys. Fluids*, **10**, 1890 (1967).
White, W. D., and D. M. McEligot, "Transition of Mixtures of Polymers in a Dilute Aqueous Solution," *ASME J. Basic Eng.*, **92**, 411 (1970).
Whitsitt, N. F., L. J. Harrington, and H. R. Crawford, "Effect of Wall Shear Stress on Drag Reduction of Viscoelastic Fluids," Western Co., Dallas, Texas, Report No. DTMB-3 (1968).
Williams, M. C., "Molecular Rheology of Polymer Solutions—Interpretation and Utility," *AIChE J.*, **21**, 1 (1975).
Yamakawa, H., *Modern Theory of Polymer Solutions*, Harper and Row, New York (1971).
Zimm, B. H., "Dynamics of Polymer Molecules in Dilute Solutions: Viscoelasticity, Flow Birefringence and Dielectric Loss," *J. Chem. Phys.*, **24**, 269 (1956).

THE AUTHOR

P. S. Virk's interest in drag reduction stems from an Sc.D. Thesis (1966) at Massachusetts Institute of Technology, supervised by Professors H. S. Mickley, E. W. Merrill, K. A. Smith, and E. L. Mollo-Christensen. He mildly enjoys teaching chemical engineering, at MIT (Assistant Professor 1966-71, Associate Professor 1971-72) and IIT/Madras (Professor 1972-present), and is currently at work on a course "Chemical Process Pathways" in hopes of introducing some mechanistic chemistry applications into the undergraduate curriculum. He is a consultant to Stone & Webster Engineering Corporation, Boston, in the areas of olefin plant technology and coal liquids processing.

Optimal Decomposition of Process Networks

PETER L. GENNA
and
R. L. MOTARD
Department of Chemical Engineering
University of Houston, Houston, Texas 77004

The tearing or decomposition of recycle process networks is extended to include the enumeration of alternate cut sets or tear stream sets. The optimality criterion is the response to convergence acceleration in the quasi-Newton sense and an algorithm is proposed to select the optimum cut set adaptively as the recycle computation proceeds.

SCOPE

The object of this study is to reduce the computer time required to complete the steady state mass and energy balance calculations in a chemical process with recycle. In the modular simulation approach, the process model in the computer consists of a set of subroutines (operation modules) whose function is to calculate the properties of the physical output streams given the properties of the physical input streams and design parameters appropriate to each module, for example, the temperature in an isothermal flash module. The process model is thus composed of a network of streams and operation modules quite analogous to the usual flow sheet representation of the plant.

Completing the steady state simulation is a matter of identifying the recycle streams in the model and finding the properties of these streams, that is, temperature, pressure, enthalpy, flow rate and composition, which lead to stationary computation loops as the information flows are traced around the plant in the direction of physical flows from one module to its neighbor. One simple procedure is to guess the recycle stream properties and then allow the computer to iterate around process loops until recycle stream properties converge. This direct substitution approach yields the slowest approach to steady state. Considerable improvement can be achieved if the successive

Correspondence concerning this paper should be addressed to R. L. Motard. P. L. Genna is with Brown & Root, Inc., Houston, Texas.